基于中子氢俘获方法的大亚湾实验 θ_{13} 新测量

（申请清华大学理学博士学位论文）

培养单位：工程物理系
学　　科：物理学
研 究 生：熙　盎
指导教师：陈少敏 教授

二〇一六年十二月

New measurement of θ_{13} via neutron capture on hydrogen at Daya Bay

Dissertation Submitted to
Tsinghua University
in partial fulfillment of the requirement
for the degree of
Doctor of Philosophy
in
Physics

by

Logan Michael Lebanowski

Dissertation Supervisor : Professor Shaomin Chen

December, 2016

关于学位论文使用授权的说明

本人完全了解清华大学有关保留、使用学位论文的规定，即：

清华大学拥有在著作权法规定范围内学位论文的使用权，其中包括：（1）已获学位的研究生必须按学校规定提交学位论文，学校可以采用影印、缩印或其他复制手段保存研究生上交的学位论文；（2）为教学和科研目的，学校可以将公开的学位论文作为资料在图书馆、资料室等场所供校内师生阅读，或在校园网上供校内师生浏览部分内容；（3）根据《中华人民共和国学位条例暂行实施办法》，向国家图书馆报送可以公开的学位论文。

本人保证遵守上述规定。

（保密的论文在解密后应遵守此规定）

作者签名：______________　　　　导师签名：______________

日　　期：______________　　　　日　　期：______________

摘　要

中微子是粒子物理标准模型中的基本粒子之一，也是宇宙中含量最为丰富的粒子之一。它们质量极其微小，不带电荷；且三种味道的中微子之间可相互转换，称为中微子振荡。振荡幅度由三个混合角 θ_{12}, θ_{23}, 和 θ_{13} 描述。精确测量混合角 θ_{13} 对中微子振荡理论的检验非常重要，同时也是加速器中微子实验研究轻子 *CP* 破坏的关键，而后者或能揭开宇宙正反物质不对称之谜题。

本论文论述在大亚湾反应堆中微子实验中一种新的对振荡幅度 $\sin^2 2\theta_{13}$ 的独立测量。大亚湾六个反应堆放出大量的反电子中微子（$\overline{\nu}_e$），每秒放出约 3×10^{21} 个。$\overline{\nu}_e$ 到达闪烁体探测器有可能与靶物质中的氢核发生反 β 衰变反应。此独立测量利用反 β 衰变的末态中子在氢上俘获的特征信号标记 $\overline{\nu}_e$ 事例。测量结果显示远点探测器的 $\overline{\nu}_e$ 事例数相较近点探测器缺失 5.0%，说明 $\overline{\nu}_e$ 发生振荡转换为其它味道的反中微子。由此测量开发的数据分析方法和建立的探测器模型也可用于未来基于中子在氢上俘获探测方法的中微子实验。进一步地，合并中子在氢上俘获和中子在钆上俘获的两种测量方法的结果，得到目前世界上最精确的 $\sin^2 2\theta_{13}$ 结果。本论文主要工作与成果为:

1. 从大亚湾实验 621 天的取数数据中识别和挑选了 780000 个中子在氢上俘获的 β 衰变事例作为候选 $\overline{\nu}_e$ 事例。分析和计算了各种本底，包括偶然符合本底、^{9}Li/^{8}He 引起的 β-n 本底，快中子本底等，并将它们从候选 $\overline{\nu}_e$ 事例中扣除，从而给出了远、近点探测器分别探测到的 $\overline{\nu}_e$ 事例。通过比较远、近点 $\overline{\nu}_e$ 事例数并与三代中微子振荡理论相比较，得到 $\sin^2 2\theta_{13} = 0.071 \pm 0.011$。
2. 系统研究了中子在氢上俘获和中子在钆上俘获的两种测量方法之间的关联，并发现最显著的关联来自慢信号的能量区间选择。考虑各种关联，将两种方法的结果合并起来，给出了目前世界上混合角 θ_{13} 的最精确测量结果: $\sin^2 2\theta_{13} = 0.082 \pm 0.004$。
3. 建立了一个通用的闪烁体探测器的能量响应模型。对不同类别的闪烁体探测器，此模型对它们的能量泄漏、能量非线性、非均匀性等性能，以及这些性能的系统误差和误差之间的关联等都提供了一种深刻理解的渠道。与探测器相关的误差是大亚湾实验的系统误差的最大来源，将此能量模型应用于大亚湾实验，成功减小了与探测器相关的误差。

关键词：中微子振荡，反贝塔衰变，液体闪烁体，中子氢俘获，大亚湾

Abstract

Neutrinos are fundamental constituents of the Standard Model of particle physics. They are some of the most abundant particles in the universe, are extremely light, have no electric charge, and their identities oscillate among three 'flavors'. The amplitudes of these oscillations are characterized with the three angles θ_{12}, θ_{23}, and θ_{13}. The accurate determination of θ_{13} is important for tests of oscillation theories, but is also key in searches at particle accelerators for leptonic *CP* violation, which may answer the basic question of why there is more matter than antimatter in the universe.

This thesis presents a new independent measurement of oscillation amplitude $\sin^2 2\theta_{13}$ at the Daya Bay Reactor Neutrino Experiment. Six nuclear reactors produced roughly 3×10^{21} electron antineutrinos ($\overline{\nu}_e$) every second. Eight 40-ton liquid scintillator detectors were used to identify $\overline{\nu}_e$ via inverse β-decays with the emitted neutron captured by hydrogen. A 5.0% deficit was observed in the number of $\overline{\nu}_e$ measured farther from the reactors relative to nearer the reactors, indicating the fraction of $\overline{\nu}_e$ that oscillated to a different flavor. The analytical techniques developed for this analysis may be useful to forthcoming neutrino experiments that will also use neutron captures on hydrogen. Furthermore, by combining with a measurement of $\sin^2 2\theta_{13}$ using neutron captures on gadolinium, the most accurate result is obtained. Achievements in this thesis include:

1. Using 621 days of data, 780000 hydrogen-neutron captures were selected as $\overline{\nu}_e$. Backgrounds were analyzed, including random coincidences, ^{9}Li/^{8}He β-n decays, and spallation neutrons, and subtracted from the number of $\overline{\nu}_e$ candidates. Comparing the resulting number of $\overline{\nu}_e$ in the near and far detectors within the three-neutrino-oscillation framework yielded $\sin^2 2\theta_{13} = 0.071 \pm 0.011$.
2. Correlations between the hydrogen- and gadolinium-capture measurements were studied, revealing that the most significant correlation is in the delayed event energy selection. A combination of the measurements produced the most precise result: $\sin^2 2\theta_{13} = 0.082 \pm 0.004$.
3. A generic energy response model of scintillation detectors was developed. It provides a thorough understanding of partial energy deposition, nonuniformity, nonlinearity, and their uncertainties and interrelations, for any scintillation-based detector. This understanding was applied to Daya Bay analyses and led to improved

detector-related systematic uncertainties, which comprise the largest component of systematic uncertainty.

Key words: neutrino oscillation; inverse beta-decay; scintillation detector; neutron hydrogen capture; Daya Bay

Contents

Chapter 1 Introduction

Precise measurements of neutrino oscillation are crucial to searches for CP-symmetry violation among neutrinos and for tests of neutrino oscillation theory. The latter is important for a general understanding of neutrinos, helping complete the picture of neutrinos in the Standard Model of particle physics. The former may explain, among other things, the basic question of why there is more matter than antimatter in the universe, a phenomenon not explained by the Standard Model. In particular, the precision of neutrino mixing angle θ_{13} is of key importance in constraining the leptonic CP phase δ_{CP}[1–4].

Before 2012, many experimental efforts had been made to determine θ_{13}[5–10]. In 2012, the first measurement of θ_{13} with a significance greater than five standard deviations was reported by the Daya Bay Reactor Neutrino Experiment[11]. Recent measurements of θ_{13} from both reactor and accelerator experiments[12–18] are consistent. In conjunction with accelerator experiments, these measurements have already led to constraints on δ_{CP}[1] (see Figure 1.1).

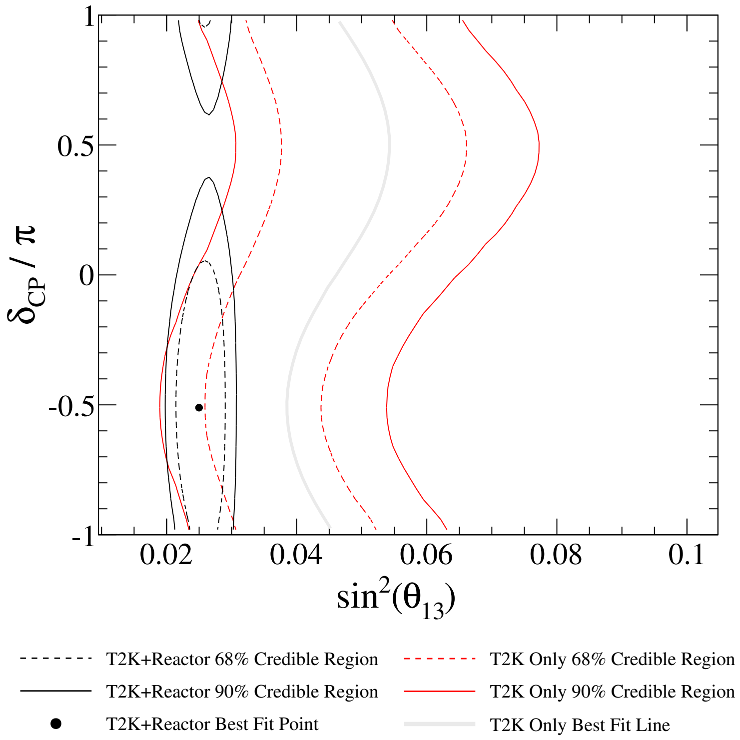

Figure 1.1 Constraints on δ_{CP} $vs.$ $\sin^2\theta_{13}$ from the T2K experiment alone (red and grey curves) and when combined with θ_{13} from reactor experiments (black). This figure is from Ref.[1].

The three reactor antineutrino experiments, Double Chooz[19], RENO[20], and Daya Bay[21], have provided the most precise measurements of θ_{13}. They used gadolinium-doped liquid scintillator to identify electron antineutrinos $\overline{\nu}_e$ through inverse β-decay (IBD) reactions ($\overline{\nu}_e + p \to n + e^+$) in which the neutron captured by gadolinium (nGd). A surrounding volume of undoped liquid scintillator improved the efficiency of detecting γ's that escaped from the doped volume, and has been used (in conjunction with the doped volume) by each of the three reactor experiments to independently measure $\sin^2 2\theta_{13}$ using IBD reactions in which the neutron captured by hydrogen (nH)[14,15,22,23]. The signature of nH IBDs has also been used by the KamLAND experiment to measure the disappearance of reactor $\overline{\nu}_e$[24] and the flux of geo-$\overline{\nu}_e$[25]. Borexino has used nH IBDs to detect geo-$\overline{\nu}_e$[26] and search for $\overline{\nu}_e$ correlated with gamma ray bursts[27]. And the Super-Kamiokande experiment has used nH IBDs to search for relic supernova $\overline{\nu}_e$[28]. Proposed and future projects, including LENA[29] and the medium-baseline reactor experiment JUNO[30], will also make use of nH IBDs. The techniques developed for this analysis at Daya Bay are described in this thesis and may be useful for these future experiments. In particular, a generic energy response model of scintillation detectors was developed and provided a foundation to understand the detector performance and its associated uncertainties. Compared with the previous analyses of nGd and nH IBDs from Daya Bay[12,15], the presented nH analysis also provides an improved understanding of backgrounds and a reduced uncertainty of the dominant neutron-capture energy selection efficiency. In addition, the statistically-independent nGd and nH measurements were found to be largely systematically independent, and their combination improves the overall uncertainty of $\sin^2 2\theta_{13}$ from Daya Bay.

This thesis is organized as follows. Chapter 2 gives a brief introduction to neutrinos and how they are produced and detected at Daya Bay. The Daya Bay experiment is described in Chapter 3. A general and thorough analysis of the detector response is presented in Chapter 4. Event selection is introduced in Chapter 5 and Chapters 6 and 7 describe the resulting backgrounds and selection efficiencies, and their uncertainties. The fit for $\sin^2 2\theta_{13}$ and the combination of the nGd- and nH-IBD measurements is presented in Chapter 8. A summary is given in Chapter 9.

Chapter 2 Neutrinos

This chapter begins with a brief and selective review of our history with neutrinos and our current understanding of them. The later sections of the chapter provide the basic knowledge needed to determine the mixing angle θ_{13} using $\overline{\nu}_e$ produced at nuclear reactors.

2.1 A Brief History

Neutrinos are some of the most abundant particles in the universe and are distinct among the known elementary particles. They are produced copiously by stars, supernovae, atmospheric cosmic rays, radioactive decays, and in the Big Bang. Man-made sources of neutrinos include particle accelerators and nuclear reactors. The interaction of neutrinos with matter is extremely weak, making neutrinos a unique tool in the study of, for example, supernova dynamics and the solar interior. They are also now being used to test geothermal models. In the Standard Model of particle physics, neutrinos are massless.

Around 1930, measurements of β-decay energy spectra (e.g., $^{210}\text{Bi} \rightarrow {}^{210}\text{Po} + \beta^- + \overline{\nu}_e$) revealed continuous spectra. With no knowledge of $\overline{\nu}_e$, the β-decay process was thought to be a two-body decay, which according to momentum and energy conservation, should result in a fixed energy for the β. In 1930, Wolfgang Pauli correctly proposed that there was an extremely light (perhaps massless), electrically neutral, spin-1/2 particle carrying away some of the energy[31].

A few years after Pauli's proposed solution, Enrico Fermi developed a β-decay theory that included the neutrino[32]. In this theory, the β-decay process is a point interaction, which is an accurate approximation only at low energies. This limitation was overcome with the electroweak theory developed by Sheldon Lee Glashow, Steven Weinberg, and Abdus Salam, in the 1960's. They predicted that weak interactions were mediated by three so-called intermediate vector bosons, the $W^{\pm}$ (80.4 GeV) and Z (91.2 GeV), all of which were discovered at CERN in 1983, January[33,34] and May[35,36], respectively.

At energies well below the masses of the vector bosons, the weak nuclear force is much weaker than the strong nuclear and electromagnetic forces, while gravity is by far the weakest. As leptons, neutrinos do not interact via the strong nuclear force. And given their lack of electric charge and tiny masses, they do not experience an electromagnetic force and experience a negligible gravitational force. As the only particles that interact almost purely through the weak nuclear force, neutrinos have a very small interaction cross section and are unique tools in the study of weak interactions. The former feature of neutrinos makes them a useful probe of physics in locations otherwise inaccessible, such as the solar or terrestrial interiors. Enticingly, weak interactions are the only one among the four known fundamental interactions, that have exhibited *CP* violation, which has not yet been confirmed or refuted for neutrinos.

The first neutrino was definitively observed by the Reines and Cowan team at Savannah River in 1956[37]. They used a 5000-L multi-layer scintillator detector to detect electron antineutrinos $\overline{\nu}_e$ from a nuclear reactor via the inverse β-decay reaction (see Section 2.4). We now know that neutrinos come in three “flavors”, partnered with the three charged leptons: electron, muon, and tau (e, μ, τ). The other two flavors of neutrinos were discovered at accelerators: the muon neutrino was discovered at Brookhaven National Laboratory in 1962[38] and the tau neutrino was discovered by the DONUT collaboration at Fermi National Laboratory in 2000[39]. Measurements on the Z boson resonance at e^+e^- colliders[40] and combined astrophysical data[41] both indicate that there are only three light Standard Model neutrinos.

As of 2016, the tiny masses of the neutrinos have not been measured. The best constraints are inferred from cosmological measurements. References[41] and[42] give upper limits for the sum of the three neutrino masses: 0.23 eV (95% C.L.) and 0.12 eV (95% C.L.), respectively. We also know from neutrino oscillation measurements (see Section 2.2), that one neutrino has a mass of at least about 0.05 eV. Thus, the scale of neutrino masses is about seven orders of magnitude smaller than the mass of the next lightest known particle, the electron (0.511 MeV). This large difference with the other elementary particles is currently unexplained by the Standard Model. To determine how neutrino masses fit into the Standard Model, precise knowledge of the masses may be necessary. Such knowledge would also enable valuable tests of cosmological and astrophysical theories.

Numerous neutrino experiments have detected neutrinos from the sun, the earth, the atmosphere, supernova 1987A, and from accelerators and reactors. It has been established with certainty that neutrinos have mass, from the first experiment to detect solar neutrinos in the 1960’s[43] to the definitive observations of neutrino oscillations by Super-Kamiokande (1998)[44] and the Sudbury Neutrino Observatory (beginning in

2001)[45]. Since these experiments, neutrino oscillations have also been measured at accelerators and reactors, which are now producing the most precise measurements, vindicating the three-neutrino-oscillation framework.

2.2 Neutrino Oscillation

Around the same time as the first detection of neutrinos, Bruno Pontecorvo suggested that neutrinos might transform[46]. A few years later, Ziro Maki, Masami Nakagawa, and Shoichi Sakata presented a quantum-mechanical model that included neutrino oscillation[47]. In the modern framework of three-neutrino oscillation, the oscillation arises due to distinct neutrino masses and is expressed with a unitary transformation between eigenstates of neutrino flavor $|\nu_\alpha\rangle$ ($\alpha = e, \mu, \tau$) and of neutrino mass $|\nu_i\rangle$ ($i = 1, 2, 3$):

$$|\nu_i\rangle = \sum_\alpha U_{\alpha i} \, |\nu_\alpha\rangle, \tag{2-1}$$

where $U_{\alpha i}$ is the Maki–Nakagawa–Sakata (MNS) matrix and is given by

$$\begin{aligned} U \equiv & \begin{bmatrix} U_{e1} & U_{e2} & U_{e3} \\ U_{\mu 1} & U_{\mu 2} & U_{\mu 3} \\ U_{\tau 1} & U_{\tau 2} & U_{\tau 3} \end{bmatrix} \\ = & \begin{bmatrix} c_{12}c_{13} & s_{12}c_{13} & s_{13}e^{-i\delta_{CP}} \\ -s_{12}c_{23} - c_{12}s_{23}s_{13}e^{i\delta_{CP}} & c_{12}c_{23} - s_{12}s_{23}s_{13}e^{i\delta_{CP}} & s_{23}c_{13} \\ s_{12}s_{23} - c_{12}c_{23}s_{13}e^{i\delta_{CP}} & -c_{12}s_{23} - s_{12}c_{23}s_{13}e^{i\delta_{CP}} & c_{23}c_{13} \end{bmatrix} \begin{bmatrix} e^{i\alpha_1/2} & 0 & 0 \\ 0 & e^{i\alpha_2/2} & 0 \\ 0 & 0 & 1 \end{bmatrix}, \end{aligned} \tag{2-2}$$

where $c_{ij} \equiv \cos\theta_{ij}$, $s_{ij} \equiv \sin\theta_{ij}$, and δ_{CP} is the *CP* phase. The phases α_1 and α_2 do not impact oscillation and are relevant only if neutrinos are Majorana particles, which is currently unknown.

The amplitudes of neutrino oscillations are characterized with the three mixing angles θ_{12}, θ_{23}, and θ_{13}, and the frequencies of neutrino oscillations are determined by the differences between neutrino masses; explicitly, Δm^2_{21}, Δm^2_{31}, and Δm^2_{32}, where $\Delta m^2_{ij} \equiv m^2_i - m^2_j$. The mass m_i of eigenstate $|\nu_i\rangle$ enters the expression via the time evolution of the state in Eq. (2-1): $|\nu_i(t)\rangle = e^{-iE_i t} \, |\nu_i(0)\rangle$.

In the case of using reactor antineutrinos to determine θ_{13}, we search for the disappearance of $\overline{\nu}_e$. The survival probability of electron (anti)neutrinos is obtained by squaring the amplitude of Eq. (2-1) with $\alpha = e$:

$$P_{ee} \equiv |\langle\nu_e(0)|\nu_e(t)\rangle|^2 = 1 - \cos^4\theta_{13}\sin^2 2\theta_{12}\sin^2\Delta_{21} - \sin^2 2\theta_{13}(\cos^2\theta_{12}\sin^2\Delta_{31} + \sin^2\theta_{12}\sin^2\Delta_{32})\,, \tag{2-3}$$

where $\Delta_{ij} \equiv 1.267\Delta m^2_{ij}L/E$, E [MeV] is the energy of the neutrino, L [m] is the distance traveled by the neutrino, and Δm^2_{ij} is in units of eV^2. As Eq. (2-3) is a survival probability ($\overline{\nu}_e \rightarrow \overline{\nu}_e$), there is no dependence on δ_{CP}. In the case of appearance probabilities, such as those relevant in accelerator experiments ($\nu_\mu \rightarrow \nu_e$ and $\overline{\nu}_\mu \rightarrow \overline{\nu}_e$), δ_{CP} is present in addition to θ_{13}; thus, knowledge of θ_{13} from reactor experiments is important in the study of δ_{CP}.

Currently, Δm^2_{21} is known to better than 3% due to the Kamioka Liquid Scintillator Antineutrino Detector (KamLAND), a reactor antineutrino experiment in Japan with an average flux-weighted baseline of about 180 km. The value of θ_{12} is known to about 2-3% dominantly due to the solar neutrino measurements of the SNO experiment (Canada). The magnitude of θ_{23} is known to about 6% due to muon neutrino beam experiments NOνA (U.S.A.), T2K (Japan), and MINOS (U.S.A.), and atmospheric muon neutrino disappearance measurements of IceCube (South Pole) [θ_{23} does not appear in Eq. (2-3)]. The magnitude of Δm^2_{32} is known to about 2% due to measurements at Daya Bay, T2K, MINOS, and NOνA. The precision of θ_{13} is 2% and due to Daya Bay. The third mass-squared difference, Δm^2_{31}, is derivable from Δm^2_{32} and Δm^2_{21}.

In this analysis, values for all parameters (except θ_{13}) were taken from Ref.[48]; specifically, $\sin^2 2\theta_{12} = 0.846 \pm 0.021$, $\Delta m^2_{21} = (7.53 \pm 0.18)\times10^{-5}$ eV^2, and $\Delta m^2_{32} = (2.44 \pm 0.06)\times10^{-3}$ eV^2 (for the normal mass hierarchy) [$\Delta m^2_{32} = (2.52 \pm 0.07)\times10^{-3}$ eV^2 (for the inverted mass hierarchy)]. Based on these values, the $\overline{\nu}_e$ survival probability of Eq. (2-3) is shown as a function of L/E in Fig. 2.1.

The mere 3% difference between Δm^2_{32} and Δm^2_{31} allows the latter term of Eq. (2-3) to be expressed with the effective mass-squared difference $|\Delta m^2_{ee}|$, which has been directly measured at Daya Bay[49]:

$$\sin^2\Delta_{ee} \approx \cos^2\theta_{12}\sin^2\Delta_{31} + \sin^2\theta_{12}\sin^2\Delta_{32}. \tag{2-4}$$

This numerical approximation is sufficiently precise for the range of L/E at Daya Bay, and expresses the measurement independently of the choice of neutrino-mass hierarchy.

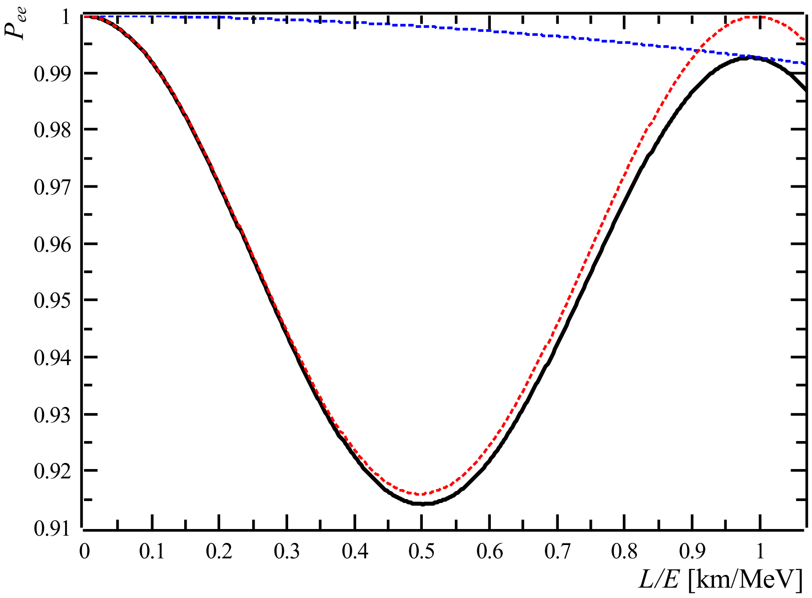

Figure 2.1 Probability of an initial electron (anti)neutrino of energy E to be an electron (anti)neutrino after traveling a distance L, assuming the normal neutrino-mass hierarchy ($\Delta m^2_{32} > 0$) (black curve). The red (blue) curve corresponds to only the Δ_{ee} (Δ_{21}) term. The upper limit of L/E in the figure corresponds to Daya Bay's longest reactor-to-detector baseline divided by the IBD energy threshold. See the text for more information.

Considering the average baseline of the farthest detectors and the average antineutrino energy of 4.3 MeV, $L/E \approx 380$ m/MeV for Daya Bay. This leads to the following approximate expression for Eq. (2-3):

$$P_{ee} \approx 1 - 0.0011 \cos^4 \theta_{13} - 0.86 \sin^2 2\theta_{13}. \tag{2-5}$$

Knowing $\theta_{13} \approx 8°$, we find that the first term in Eq. (2-5) is $O(1\%)$ of the second term and, therefore, the oscillation observed at Daya Bay has little impact from Δm^2_{21} or θ_{12}. This is illustrated with the red and blue curves in Fig. 2.1. Consistently, the uncertainties associated with the input oscillation parameters were found to have negligible impact on the fit of $\sin^2 2\theta_{13}$ and its uncertainty.

2.3 Reactor Antineutrino Flux

Commercial nuclear reactors isotropically emit approximately 2×10^{20} $\overline{\nu}_e$ per second per GW of thermal power. These $\overline{\nu}_e$ are produced in the β-decays of neutron-rich daughters from four primary fissile isotopes: ^{238}U, ^{235}U, ^{241}Pu, and ^{239}Pu. In this analysis, the rate of emission of reactor antineutrinos was calculated as

$$\frac{d^2N(E,t)}{dE\,dt} = \frac{W_{\mathrm{th}}(t)}{\sum_i f_i(t)e_i} \sum_i f_i(t)S_i(E)c_i^{\mathrm{ne}}(E,t) + S_{\mathrm{snf}}(E,t), \tag{2-6}$$

where the sum is over the four primary fissile isotopes. The nuclear power plant supplied the thermal power of the reactor $W_{\mathrm{th}}(t)$ and the fraction of fissions due to the ith isotope $f_i(t)$. The average thermal energies released per fission e_i (about 200 MeV) were taken from Ref.[50], and the antineutrino yields per fission $S_i(E)$ of ^{238}U, and of ^{235}U, ^{239}Pu, and ^{241}Pu, were from Ref.[51] and Ref.[52], respectively. About six $\overline{\nu}_e$ are produced per fission. The spectral models $S_i(E)$ are known to be imperfect[53], but the level of the spectral deficiencies (several %) introduce negligible consequences in a far-near relative analysis of measured antineutrino rates. The subdominant correction of the energy spectrum due to nonequilibrium effects of long-lived fission fragments $c_i^{\mathrm{ne}}(E,t)$ followed Ref.[51]. Also subdominant, contributions from removed spent nuclear fuel $S_{\mathrm{snf}}(E,t)$ were estimated following Refs.[54,55]. The combination of the uncertainties of these components yields a 0.9% reactor-uncorrelated uncertainty of the predicted IBD rate originating from a single reactor[53]. Reactor-correlated uncertainties play a negligible role in a far-near relative analysis. More information is given in Refs.[56,57].

Each of the time-dependent quantities was estimated daily, then weighted by the fractional data acquisition time of each day for each experimental hall, and finally summed for each week for use in the analysis. The accumulated predicted spectra $dN_r(E)/dE$ are shown in Fig. 2.2 and provided in Appendix B.1. The average fission fractions during this period were ^{235}U : ^{239}Pu : ^{238}U : ^{241}Pu = 0.561 : 0.307 : 0.076 : 0.056.

2.4 Inverse β-decay

Inverse β-decay (IBD) reactions are defined by the interaction of an $\overline{\nu}_e$ with a proton, and the production of a neutron and a positron: $\overline{\nu}_e + p \to n + e^+$. In the case of an isolated proton (hydrogen atom) at rest, the initial and final energies of the IBD reaction are expressed as

$$E_{\overline{\nu}_e} = E_{e^+} + E_n + E_{\mathrm{threshold}}, \tag{2-7}$$

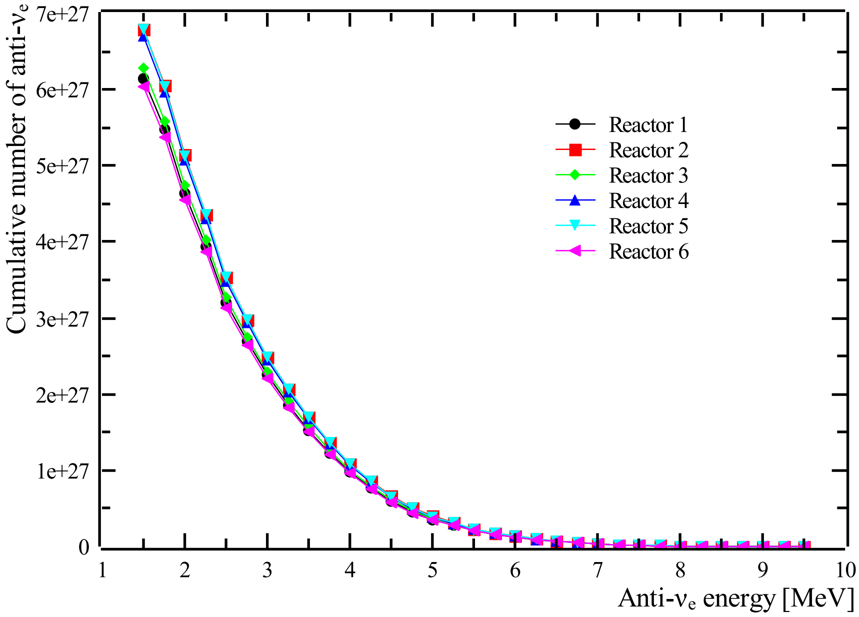

Figure 2.2 Predicted number of $\overline{\nu}_e$ per 0.25 MeV produced by each of the six reactors at Daya Bay integrated over the data acquisition periods of experimental hall 1 (EH1) (2011/12/24-2013/11/27). Applicable to both ADs in EH1.

where the last term is the IBD energy threshold:

$$E_{\text{threshold}} = \frac{(m_n + m_e)^2 - m_p^2}{2m_p} = 1.806\ \text{MeV}, \tag{2-8}$$

where m_n, m_p, and m_e are the masses of the neutron, proton, and electron. Besides hydrogen, the only other atom present in the scintillator in significant quantity is carbon. Since $E_{\text{threshold}} = 14$ MeV for carbon, only IBDs with hydrogen are relevant for reactor neutrinos.

The IBD cross section σ_{IBD} used to predict the energy spectra of detected antineutrinos was evaluated according to Ref.[58], to first order in $1/M$, where M is the nucleon mass. The cross section to zeroth order in $1/M$ is[58]

$$\sigma_{\text{IBD}}^{(0)} = \frac{2\pi^2}{f^R \tau_n m_e^5} E_{e^+}^{(0)} p_{e^+}^{(0)}, \tag{2-9}$$

where f^R is the phase space factor (1.7), τ_n is the neutron lifetime (880 s), and $E_{e^+}^{(0)}$ and $p_{e^+}^{(0)}$ are the zeroth order positron energy and momentum. Updated values were applied for the neutron lifetime, and less significantly, the phase space factor, both taken from Ref.[48]. The relatively small magnitude of the cross section is apparent after substituting all values:

$$\sigma_{\mathrm{IBD}}^{(0)} \approx 0.09 \frac{E_{e^+}^{(0)} p_{e^+}^{(0)}}{\mathrm{MeV}^2} \times 10^{-42} \mathrm{cm}^2. \tag{2-10}$$

Given that cross sections in nuclear and particle physics are typically at the level of a barn (10^{-24} cm^2), neutrino interactions are extremely weak. The cross section for elastic scattering with electrons ($\overline{\nu}_e + e^- \rightarrow \overline{\nu}_e + e^-$) is a few orders of magnitude smaller than that for IBDs. This and the single resulting event of the scattered electron make this channel less straightforward for counting $\overline{\nu}_e$ at nuclear reactors.

After the $\overline{\nu}_e$ spectra $dN_r(E)/dE$ of Fig. 2.2 are multiplied with the IBD cross section, the resulting IBD-$\overline{\nu}_e$'s have an average energy between 4.2 and 4.3 MeV. These spectra are shown in Fig. 2.3 without considering any oscillation between $\overline{\nu}_e$ production and detection. The small values of the ordinate result in a countable number of $\overline{\nu}_e$ when using a target with a sufficient number of protons. This value is $O(10^{30})$ for the Daya Bay detectors.

Based on the spectra of Fig. 2.3, the positron is found to carry away 99.4% of the kinetic energy of the final state on average. The average kinetic energy of the neutron is 0.016 MeV (see Fig. 2.4). Neutrons are emitted forwardly while the positrons are emitted

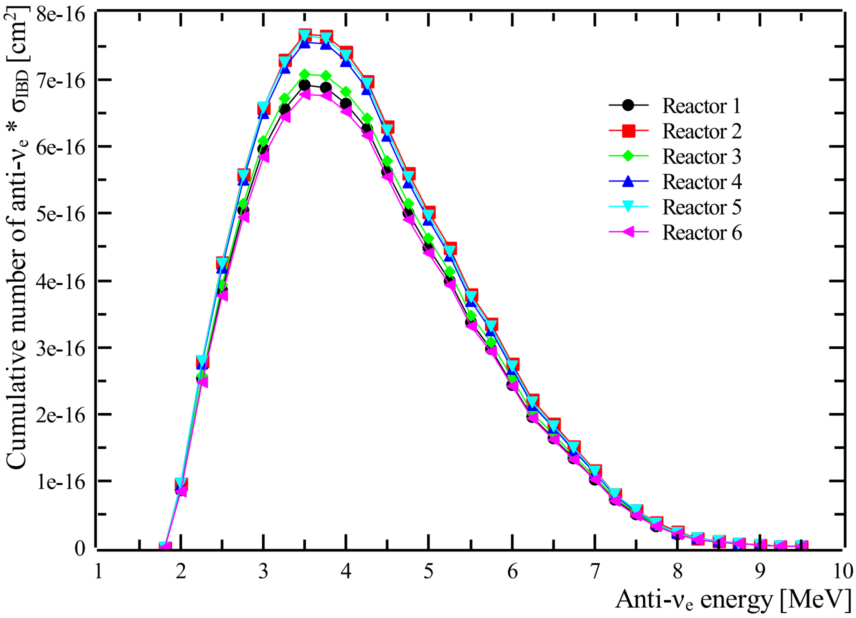

Figure 2.3 Predicted number of $\overline{\nu}_e$ per 0.25 MeV produced by each of the six reactors at Daya Bay integrated over the data acquisition periods of experimental hall 1 (EH1) and multiplied by the inverse-β decay cross section.

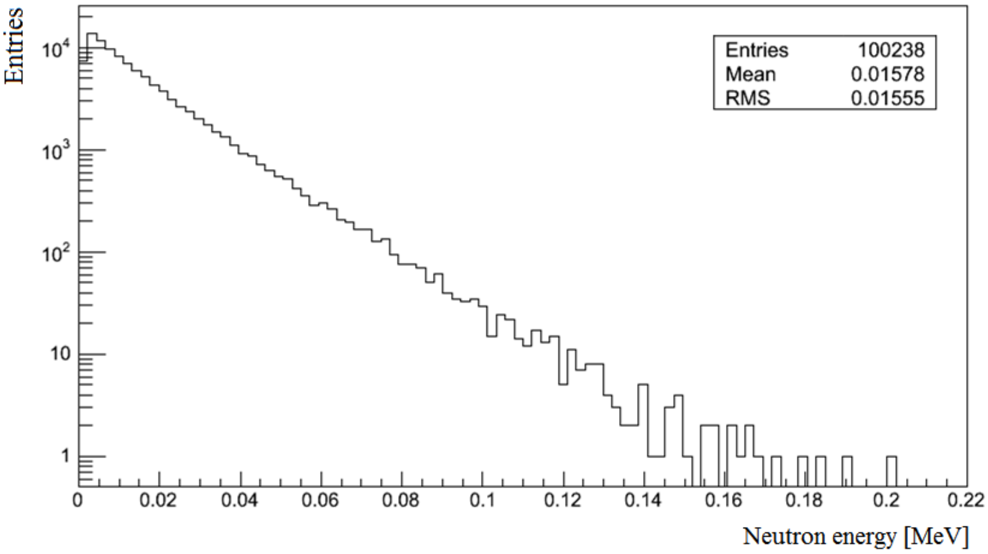

Figure 2.4 Distribution of initial kinetic energy of neutrons originating from inverse beta decays with reactor neutrinos (Monte Carlo calculation).

nearly isotropically.

Considering the annihilation of the produced e^+ with an e^- in the detector, which adds 2×0.511 MeV, the energy of the incident $\overline{\nu}_e$ is simply related to the total energy of the prompt event E_{prompt} (see Section 3.1):

$$E_{\overline{\nu}_e} \approx E_{\text{prompt}} + 0.784\ \text{MeV}. \tag{2-11}$$

Chapter 3 The Daya Bay Reactor Neutrino Experiment

Located in Guangdong province, China, the Daya Bay Reactor Neutrino Experiment is an international venture involving institutions in China, the U.S.A., Russia, the Czech Republic, and Chile. The experiment was designed to determine neutrino mixing angle θ_{13} with a sensitivity better than 0.01 in $\sin^2 2\theta_{13}$ (90% confidence level) by comparing measured rates and energy spectra of reactor antineutrinos at different baselines[21]. The Daya Bay nuclear power station consists of three pairs of nuclear reactors with each reactor nominally producing 2.9 GW of thermal power and therefore, a total of about 3.5×10^{21} electron antineutrinos $\overline{\nu}_e$ per second, making the station one of the most prolific sources of $\overline{\nu}_e$ in the world. Two *near* experimental halls (EH1 and EH2) are located roughly 360-470 m from their nearest reactor, and one *far* experimental hall (EH3) is 1.5-1.9 km from all six reactors. The halls were constructed within adjacent mountains to be shielded from cosmogenic muons. The layout is shown in Fig. 3.1. The near (far) experimental halls contain two (four) identically-designed antineutrino detectors (ADs) submerged in

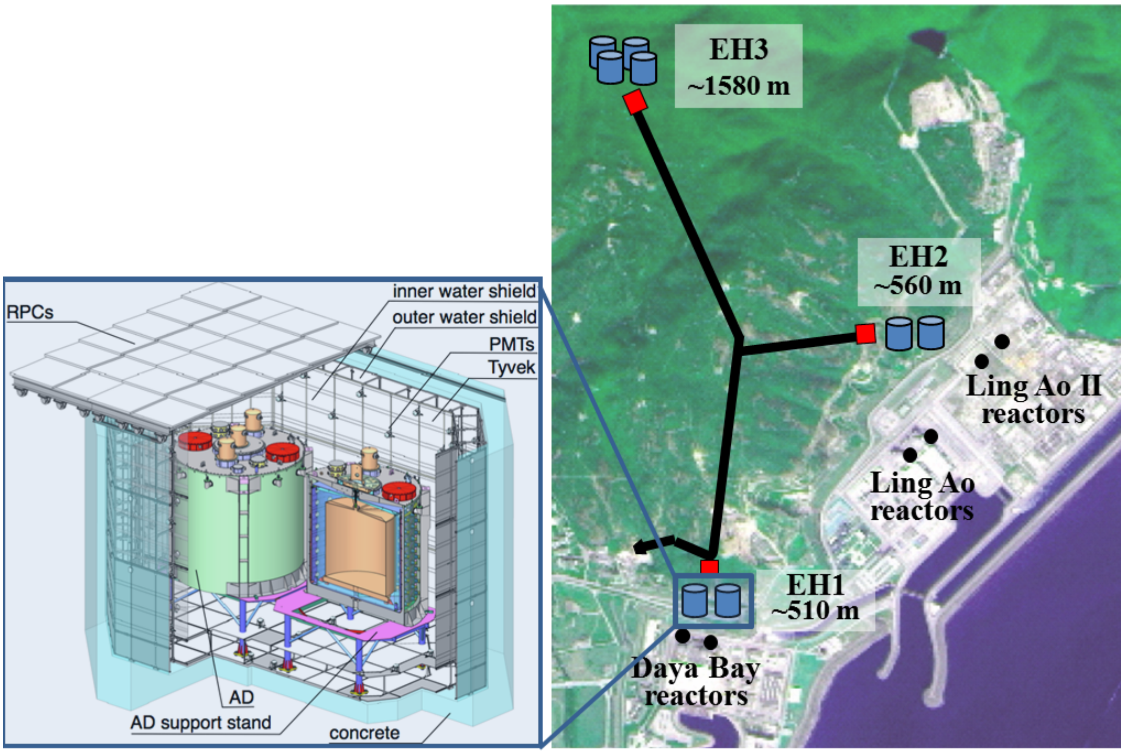

Figure 3.1 Layout of the Daya Bay experiment.

a two-zone water Cherenkov detector as illustrated in Fig. 3.1. Figure 3.2 shows EH3 on 2012/8/29, when the water was being refilled after installation of the eighth and final AD. Additional details about the detector hardware that are not described in this chapter may be found in Ref.[59].

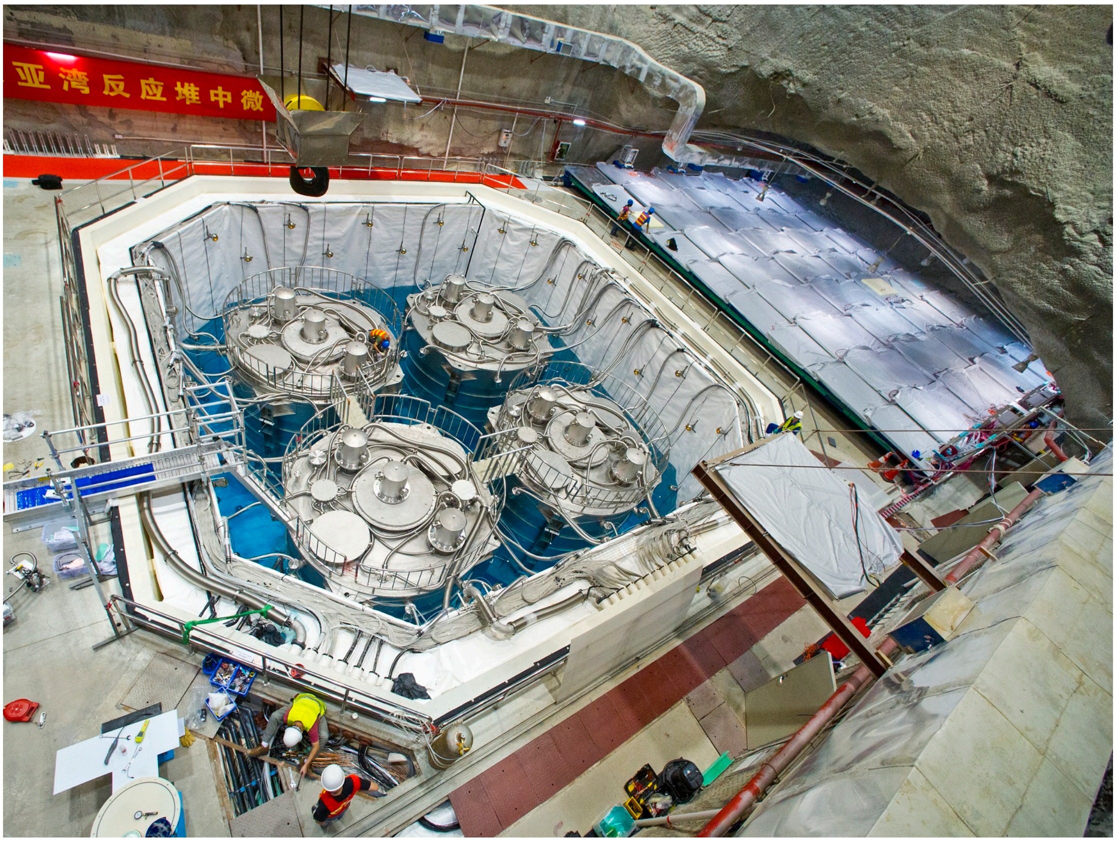

Figure 3.2 Photograph of experimental hall 3 on 2012/8/29. Photo courtesy of Lawrence Berkeley National Laboratory (© 2010 The Regents of the University of California, through the Lawrence Berkeley National Laboratory).

By comparing the number of observed IBDs (see Section 2.4) between the near (EH1 and EH2) and far (EH3) ADs, the amplitude of the neutrino oscillation probability $\sin^2 2\theta_{13}$ [see Eq. (2-5)] is determined. Additionally, comparing the shapes of the spectra between the near and far ADs, the frequency of the oscillation probability Δm^2_{ee} [see Eq. (2-4)] is determined and the precision on the amplitude is improved. Given that the comparison is between eight identically-designed ADs, generally, only detector-uncorrelated (and reactor-uncorrelated) uncertainties contribute to the uncertainties of the measured parameters.

The number of IBDs expected in an AD was calculated as the product of

- the number of IBDs per target proton Φ

- the efficiency-weighted number of target protons N_ε:

$$\overline{N}_{\text{IBD}} = \Phi N_\varepsilon. \tag{3-1}$$

The latter is discussed in Chapter 7. The expected number of IBDs per target proton for the dth AD was defined as

$$\Phi_d \equiv \sum_{r=1}^{6} \frac{1}{4\pi L_{dr}^2} \iint_{\{t_d\}} \sigma_{\text{IBD}}(E)\; P_{ee}\left(\tfrac{L_{dr}}{E}\right) \frac{d^2N_r(E,t)}{dEdt} dEdt, \tag{3-2}$$

where L_{dr} is the baseline from the rth reactor core to the dth AD, $\sigma_{\text{IBD}}(E)$ is the IBD reaction cross section of an $\overline{\nu}_e$ with energy E (see Section 2.4), $P_{ee}(L_{dr}/E)$ is the $\overline{\nu}_e$ survival probability (see Section 2.2), and $d^2N_r(E,t)/dEdt$ is the number of $\overline{\nu}_e$ emitted from the rth reactor at time t with energy E (see Section 2.3), which is integrated over the periods of data acquisition for the dth AD $\{t_d\}$.

The baselines L_{dr} were measured with negligible uncertainty[59] and are listed in Table 3.1.

Table 3.1 Baselines between the center of the dth AD and the center of each reactor core.

Detector	L_{d1} [m]	L_{d2} [m]	L_{d3} [m]	L_{d4} [m]	L_{d5} [m]	L_{d6} [m]
EH1-AD1	362.380	371.763	903.466	817.158	1353.618	1265.315
EH1-AD2	357.940	368.414	903.347	816.896	1354.229	1265.886
EH2-AD1	1332.479	1358.148	467.574	489.577	557.579	499.207
EH2-AD2	1337.429	1362.876	472.971	495.346	558.707	501.071
EH3-AD1	1919.632	1894.338	1533.180	1533.628	1551.384	1524.940
EH3-AD2	1917.519	1891.977	1534.919	1535.032	1554.767	1528.046
EH3-AD3	1925.255	1899.861	1538.930	1539.468	1556.344	1530.079
EH3-AD4	1923.149	1897.507	1540.667	1540.872	1559.721	1533.179

3.1 Antineutrino Detection

At Daya Bay, antineutrinos were detected via IBD reactions ($\overline{\nu}_e + p \rightarrow n + e^+$) in which the positron carried away 99.4% of the kinetic energy of the final state on average. Thus, the measured energy associated with the positron was readily related to the energy

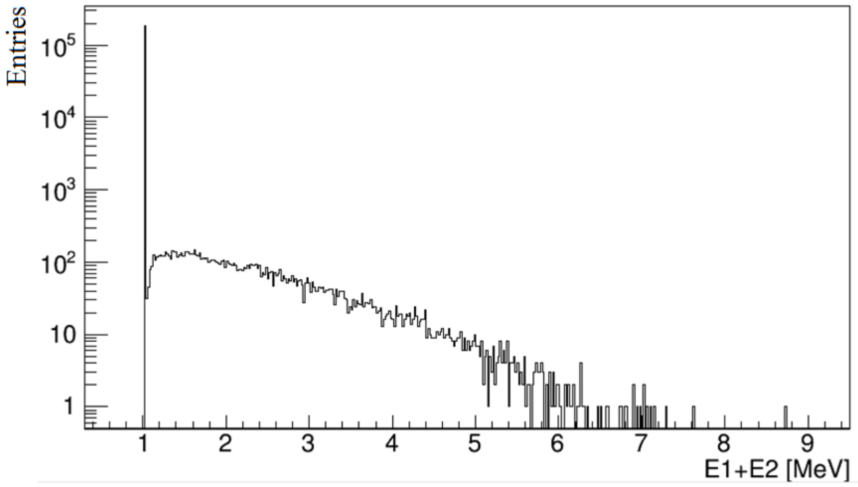

Figure 3.3 Sum of the energies of the two γ's from an IBD positron at Daya Bay (with no detector effects). Values above 1.02 MeV occur because of positron annihilation in flight.

of the incident $\overline{\nu}_e$ (see Sec 2.4). The positron deposited its energy within $O(1)$ ns and then annihilated with an electron, usually producing two back-to-back 0.511-MeV γ's. Several percent of the positrons annihilated in flight and produced two γ's whose energies summed to more than 2×0.511 MeV. The energy spectrum of the two annihilation γ's is shown in Fig. 3.3.

In the scintillator (see Section 3.2.2), the neutron thermalized and was captured primarily by Gd or H, releasing an approximately 8-MeV γ-cascade or a single 2.22-MeV γ, respectively. The reconstructed capture energy spectrum of IBD neutrons produced in the full volume of an AD is shown in Fig. 3.4 (simulation) where the fractions of captures by other nuclei are seen to be small. The broad nGd peak is due to the two isotopes of Gd that have very large capture cross sections for thermal neutrons: ^{157}Gd with a cross section of more than 250000 barns and ^{155}Gd with more than 60000 barns. The corresponding cross section of hydrogen is about 0.3 barns; thus, only a small amount of Gd is needed to shorten the neutron capture time in the scintillator. Upon de-excitation, the two Gd isotopes release a γ-cascade of total energy 7.94 and 8.54 MeV, respectively. With natural abundances of 15.7% and 14.8%, their relative capture probabilities are approximately 82% and 18%, respectively.

The time from the production of the neutron to its capture was typically tens to hundreds of microseconds. The temporal coincidence of the prompt positron event and delayed neutron-capture event allows clear distinction of $\overline{\nu}_e$ from single-event backgrounds.

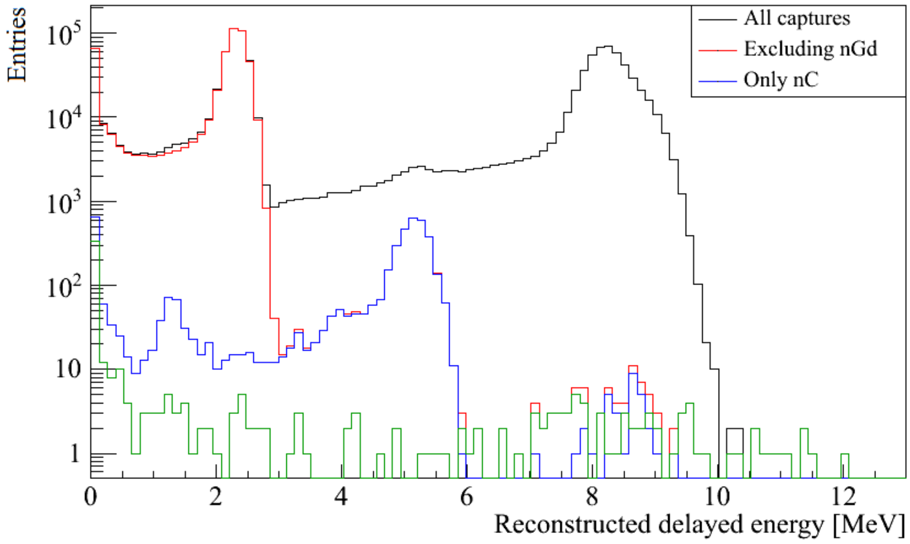

Figure 3.4 Reconstructed capture energy spectrum of IBD neutrons produced in the full AD volume and captured by various nuclei (simulation). The green line is the spectrum from neutron captures on all nuclei other than H, Gd, and C. The low-energy and coincidence-time criteria of the nGd analysis are applied.

3.2 Antineutrino Detectors

The eight identically-designed ADs consist of three nested, coaxial cylindrical vessels: an inner and outer acrylic vessel (IAV and OAV)[60] and an outermost stainless steel vessel (SSV), as shown in Fig. 3.5. The z axis is defined by the central axis of the cylinders and the r coordinate is measured radially from the central axis. The IAV is about 3 m in both diameter and height, and contains 20 tons of gadolinium-doped (0.1% by mass) liquid scintillator (GdLS)[61]. The surrounding OAV is about 4 m in both diameter and hight, and contains 22 tons of undoped liquid scintillator (LS) to improve the efficiency of detecting γ's that escape from the GdLS. The surrounding SSV is about 5 m in both diameter and height, and contains 36 tons of mineral oil (MO) to shield the scintillator against radiation from the PMTs and the SSV.

Each AD utilizes 192 20-cm PMTs arranged in 24 columns and 8 rings at a fixed radius ($r \approx 2.19$ m) within the MO. As can be seen in Fig. 3.5, a radial shield is flush with the widest diameter of the PMT glass, at $r \approx 2.26$ m. This shield is a matte-black acrylic with a reflectivity between 4% and 5% in the wavelength range of interest. The low reflectivity minimizes the complexity of event reconstructions. Reflectors with about 97% specular reflectivity were placed above and below the OAV to improve light collection.

Three automated calibration units (ACUs) were installed atop each AD and house LEDs and various radioactive sources for calibrating the energy scale and the position

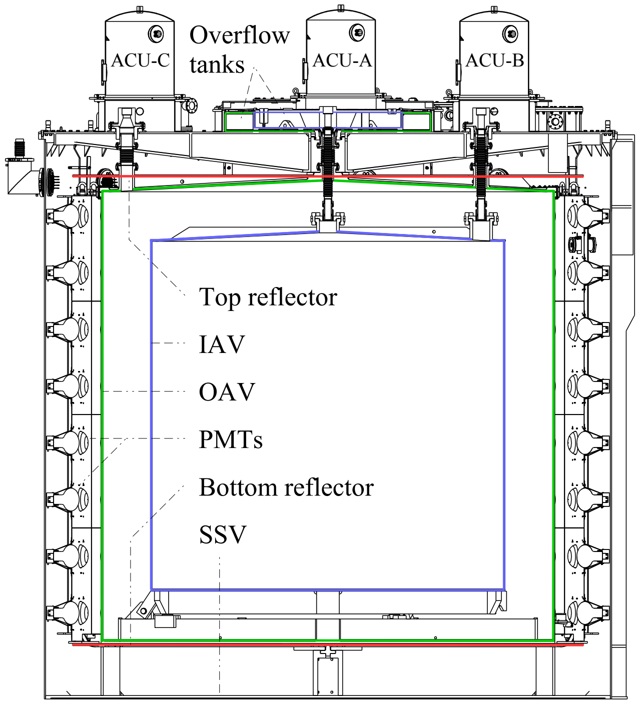

Figure 3.5 Schematic of an antineutrino detector. See text for definitions.

reconstruction of events[62]. The ACUs deploy sources vertically at three radial positions: ACU-A at $r = 0$, ACU-B near the inner wall of the IAV ($r = 1.35$ m), and ACU-C near the inner wall of the OAV ($r = 1.77$ m).

3.2.1 Acrylic Vessels

The acrylic volumes are in direct contact with the scintillator. Within these volumes, particles do not produce scintillation light, but instead produce a relatively small amount of light due to Cherenkov radiation. The impact of this localized reduction in light yield on both the rate and energy spectrum of detected $\overline{\nu}_e$, was estimated with simulation. A difference between the rates and energy spectra of the far and near ADs could arise from a difference in the densities and thicknesses of their IAVs. The density of the acrylic was measured to be 1.19 ± 0.01 g/cm^3[60], a 0.8% uncertainty which was propagated through the simulation to give a conservative 0.1% variation in the number of events above 1.25 MeV and 4% below. The average thicknesses for the far and near ADs are about 10.84 mm and 10.65 mm, respectively, a 1.8% difference that was also considered in the simulation. The thicknesses of the OAVs are irrelevant since they are surrounded by MO, which has a similar light yield as acrylic. Instead, the inner radius of the OAV could impact the peak-to-tail ratio of an energy spectrum, where the tail is due to energy deposition outside scintillator. Generally, if the OAV radius is larger, the peak-to-tail ratio will be larger, and vice versa. The inner radii of the OAVs of EH1-AD1 and EH1-AD2 averaged from 20 measurements at five heights across four azimuthal quadrants, are 3969.1 mm and 3965.3 mm, respectively. The standard deviation of the measurements at each height ranged from 1 mm to 8 mm, which is up to a 0.2% variation in radius, or a 0.4% change in volume. This variation was considered in evaluating the uncertainty of the delayed-event-energy criteria efficiency in Section 7.4. The refractive index of the acrylic is 1.50 with very little dependence on wavelength[60].

3.2.2 Organic Liquid Scintillator

Daya Bay scintillator[61] (undoped) is composed (by mass) of

- base LAB (99.6%), which scintillates and transfers energy to a primary fluor.
- primary fluor PPO (0.3%), which isotropically emits longer wavelength ultraviolet fluorescent light.
- wavelength shifter bis-MSB (0.0015%), which absorbs light and isotropically re-emits in the longer-wavelength visible spectrum to be detected at the PMTs.

The base LAB (linear alkyl benzene) consists of a linear alkyl chain of 10 to 13 carbon atoms and a benzene ring. Incident particles ionize and excite primarily LAB, which transfers energy to PPO (2,5-diphenyloxazole) via non-radiative mechanisms[63,64]. LAB radiates with a mean time of 49 ns while PPO, 1.5 ns[64]; thus, energy is transferred to PPO non-radiatively at the ns-scale. It should be noted that there are both fast and slow fluorescence time scales for most scintillators. These two scales are associated with singlet and triplet state excitations, respectively, and are often different by one or two orders of magnitude. “bis-MSB” stands for p-bis-(o-methylstyryl)-benzene. Finally, roughly 10000 photons are produced per MeV of energy deposited by β’s or γ’s.

The Gd-doped LS is identical to the undoped LS except for the presence of 0.1% (by mass) Gd. Specifically, 3,5,5-trimethylhexanoic acid (TMHA) was the ligand for the Gd[61]. Since the compound was present in small amount, the impact to the performance of the scintillator is also small. The measured densities were about 0.859 and 0.860 g/cm^3 for the LS and GdLS, respectively (that for the MO was about 0.851 g/cm^3). Early measurements of refractive indexes gave about 1.50 and 1.49 (1.47). Measurements of attenuation length at wavelengths of 420, 430, 440, and 470 nm resulted in rough values from 7 to 25 m, and suggested that the GdLS may have an attenuation length that is

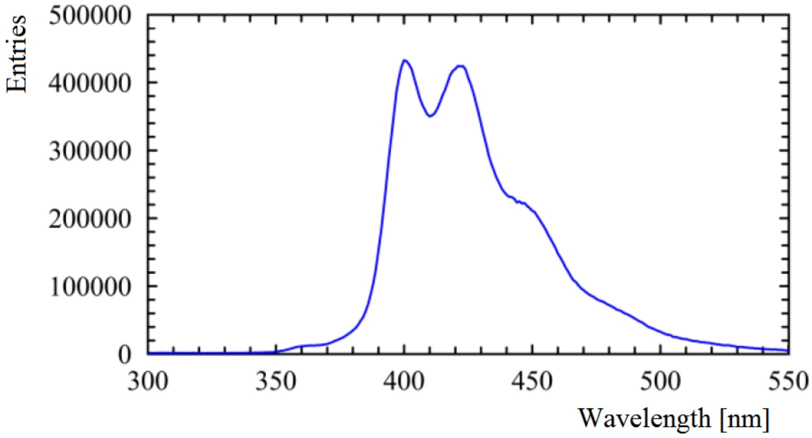

Figure 3.6 Measured emission spectrum of GdLS when excited at 260 nm.

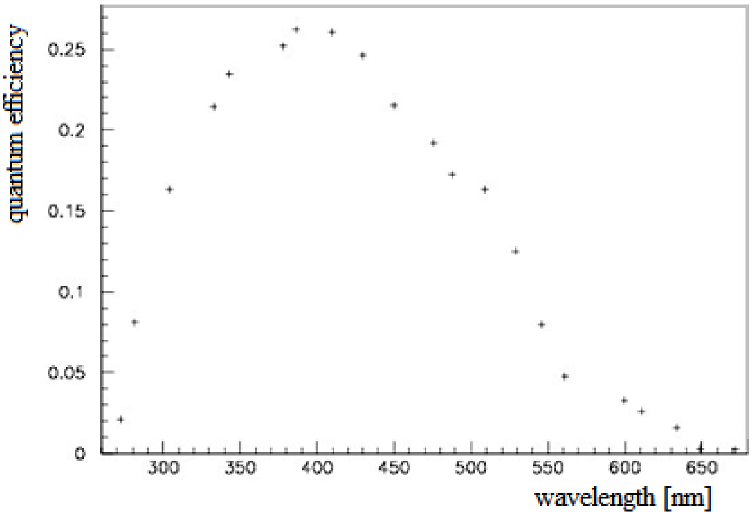

Figure 3.7 Measured quantum efficiency of a single PMT *vs.* wavelength.

roughly 10% shorter than that of the LS. Figure 3.6 shows the emission spectrum of GdLS measured with fluorescence spectrometry[61].

3.2.3 Photomultiplier Tubes

The 192 20-cm PMTs that populate each AD are Hamamatsu R5912[65]. The PMTs are operated at a gain of 10^7 with a typical voltage of +1400 to +1500 V. Based on measurements of all the PMTs before installation, the average rise time was 3.7 ± 0.5 ns and the average quantum efficiency was (22.0 ± 2.0)%. Figure 3.7 shows the quantum efficiency of a single PMT *vs.* wavelength. The efficiency spectrum overlaps with the emission spectrum of the scintillator shown in Fig. 3.6. The PMTs typically saturated above about 2000 photoelectrons (p.e.) and had a linear response up to several hundred photoelectrons. PMT signal overshoot, which is a positive tail of the primary negative

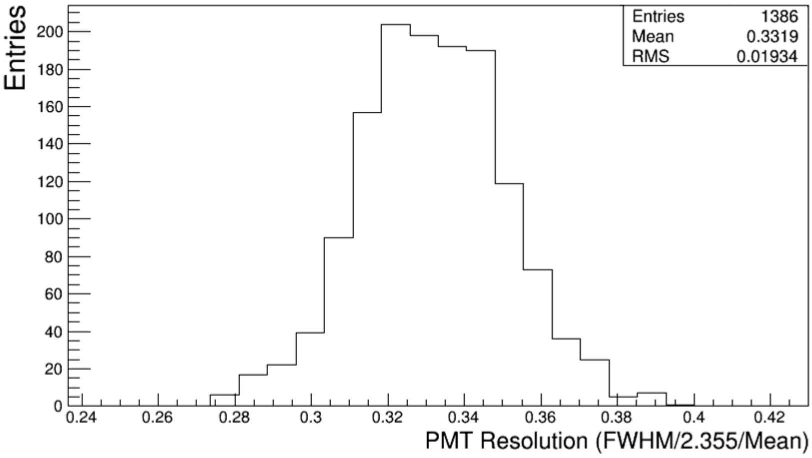

Figure 3.8 Measurements of R5912 s.p.e. resolution before installation at Daya Bay.

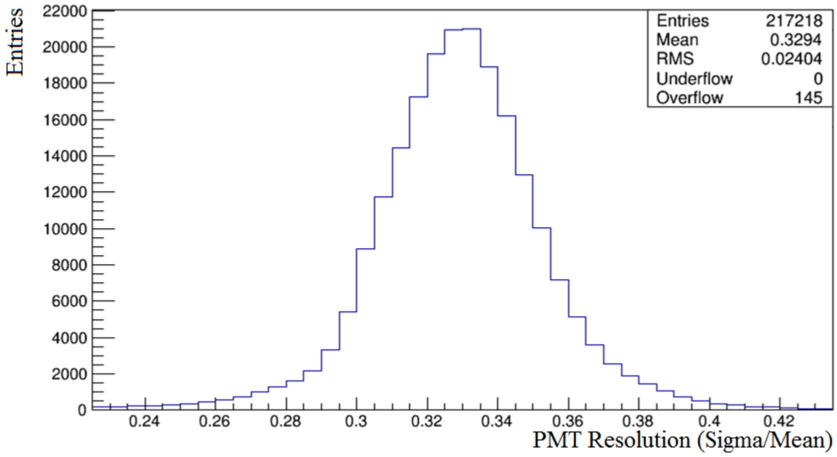

Figure 3.9 *In-situ* measurements of R5912 s.p.e. (plus electronics) resolution at Daya Bay from 2011/08 to 2014/07.

pulse, resulted from a capacitive coupling of the signal from the anode to the ground. The overshoot spanned approximately 0.51 μs and had a charge that was nearly equal in magnitude to the charge of the primary pulse. The single photoelectron (s.p.e) resolution was 33% as measured both before installation and during operation, the latter via the PMT channel calibration mentioned in Section 4.1. The two resolution distributions are shown in Figs. 3.8 and 3.9. In the ADs, the PMTs had an average dark rate of about 5.5 kHz.

3.2.4 EH3-AD1 Leak

When data-recording was paused to install the final two ADs around the end of July, 2012, a leak occurred between the LS and MO volumes of EH3-AD1. The levels of LS and GdLS in the overflow tanks[66] (see Fig. 3.5) of EH3-AD1 slowly decreased while the level of MO slowly increased, suggesting that the LS was leaking into the MO region. This hypothesis is supported by measurements with the MO clarity system[59], which showed substantial decreases in the transmission of shorter-wavelength light through the MO and an increase of MO light yield over time, consistent with a gradual adding of scintillator into the MO. The hypothesis was further supported by the observation of an increased (decreased) rate of higher-energy (lower-energy) muons reconstructed in the MO volume. After about two years, these observed trends stabilized with an estimated total leakage of about 20 kg. This loss of mass lowered the height of the LS and GdLS levels in the overflow tanks and did not directly impact the number of target protons in the LS and GdLS volumes.

No impact on the detector response in the LS volume is expected due to the direction of the leak; however, in the MO volume, there is potential for an increase in trigger rate. Given a 20-kg leakage into the 36-ton volume, and roughly estimating the light yield of the LS to be two orders of magnitude greater than that of the MO (using simulation), one may naively estimate an average increase of the light yield in the MO volume of $O(1\%)$. In simulation, this increase in light yield was modeled as an increase in reconstructed energy scale, and was applied to prompt and delayed events of IBDs generated in the MO, resulting in a $O(0.001)\%$ increase of the nH-IBD selection efficiency (and about five times smaller for the nGd-IBD efficiency). Indeed, the leak has had no observable impact in the nH-IBD analysis and in comparisons of various quantities before and after the start of the leak. These quantities include various event rates, neutron-capture energy peak and resolution, and IBD prompt and delayed event-position distributions. Given the stabilization of the leak, no impact is expected in the future.

3.3 Cosmogenic Muon Detectors

The three experimental halls are located hundreds of meters below the surfaces of the mountains adjacent to the Daya Bay nuclear power plant. More precisely EH1, EH2, and EH3, are located 93, 100, and 324 m directly below the surfaces, corresponding to about 250, 265, and 860 m of water. From simulation[67] and surveys of the mountain profiles, the average muon energy in each hall is about 57, 58, and 137 GeV, respectively.

Detecting cosmogenic muons allows an estimation of muon-induced backgrounds; particularly, ^{9}Li/^{8}He decay products and spallation neutrons. The water Cherenkov cosmogenic muon detector[67] of each hall consists of inner and outer zones, which together provide each AD with $>$ 2.5 m of shielding against ambient radiation and spallation products of nearby cosmogenic muons. These *inner* and *outer* water shields (IWS and OWS) are independent muon detectors with 160 (121) and 224 (167) 20-cm PMTs, respectively, in the far (near) hall(s). An array of resistive plate chambers above the water shields provides additional muon detection capability, however these arrays are not used in this analysis.

3.4 Readout Electronics

The same readout electronics (RE) are used for both the ADs and the water shields. These RE are housed, along with local trigger boards, in a single VME crate for a given detector (AD, IWS, or OWS). The RE measure the charges of PMT pulses in units of analog-to-digital converter (ADC) channels and record the times associated with an ADC threshold crossing (≈0.25 p.e.) in units of time-to-digital converter channels (TDCs). It is shown that the performance of the RE contributes negligibly to the energy resolution and nonlinear response of the detectors. However, the interplay between the time distribution of photons and the charge integration time produces a nonlinear charge estimate.

Two ADC ranges are used in the RE to provide higher resolution (a shorter range) at lower charge, and lower resolution (a longer range) at higher charge. These two ranges are illustrated in Fig. 3.10, where DAC refers to digital-to-analog converter, which are discussed in what follows. The low-charge ("fine") range measures channel charges up to about 200 p.e. for a PMT gain of 10^7 (about 1 MeV). Practically, all channels give readouts in the fine range for IBDs. Thus, calibration of the high-charge ("coarse") range primarily serves to calibrate higher energy events, such as muon events, and will not be discussed

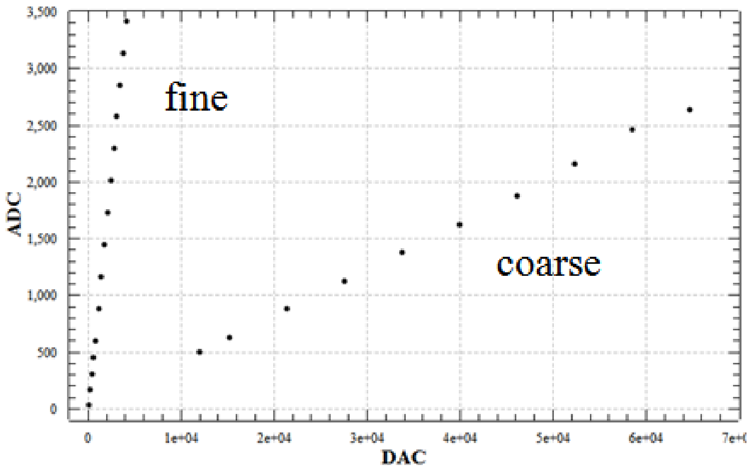

Figure 3.10 ADC *vs*. DAC measured for both fine and coarse ranges of a single RE channel.

further. The conversion from ADC channel to p.e. for the fine range was obtained through PMT ⊕ RE gain calibration as described in Section 4.1.

PMT signals are processed by the RE as follows. A signal first enters a high-speed amplifier and is then split into two parallel RC feedback op-amps. The two signals are then shaped by CR-(RC)^4 shaping circuits with distinct gains. Finally, the shaped signals enter their respective fine and coarse range ADCs. This scheme is shown in Fig. 3.11. Pulses enter each channel through the high-speed amplifier, which increases the gain of pulses by a factor of about 44. The aim of the RC feedback op-amps is to produce output pulses whose amplitudes are proportional to the charges of the input pulses. Therefore, the charge of an input pulse can be determined by simply measuring the peak of the output pulse. The op-amp is an ADI AD8066 with a differential gain error of 0.02%. The values of R_f and C_f are 2 kΩ and 10 pF, and 20 kΩ and 120 pF, for the fine and coarse ranges, respectively. These values give RC times of 20 ns and 2.4 μs. The typical rise time of a PMT signal is about 4 ns. To accurately measure waveform peaks, the CR-(RC)^4 shaping circuits broaden pulses by an order of magnitude: the peak time is approximately 4 × 25 ns = 100 ns. The circuits have a linear response and improve the signal-to-noise ratio. The shaped analog outputs are digitized by 12-bit/40-MSPS ADI AD9222-40 ADCs for

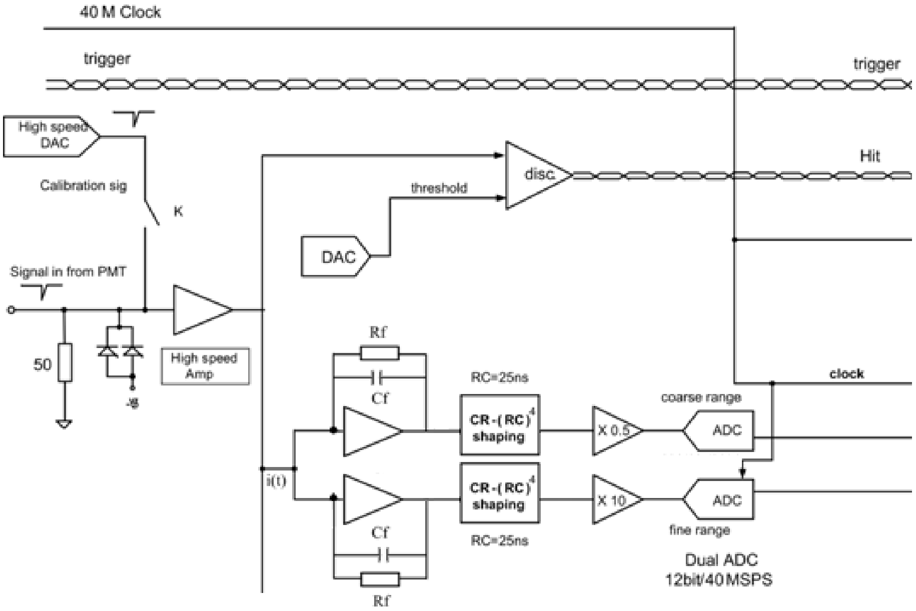

Figure 3.11 Simplified diagram of an RE channel (cropped) showing the initial circuitry of charge measurement.

both the fine and coarse ranges. From its datasheet, the largest typical Effective Number Of Bits (ENOB) is 11.38 [the ENOB is based on the signal-to-noise and distortion ratio (SINAD)]. Thus, the best expected accuracy of the ADC is $1/2^{11.38} \approx 0.038\%$, which corresponds to approximately 1.5 ADC channels, or 0.08 p.e., for the fine range and 1.6 p.e. for the coarse range. Typical values of differential and integral nonlinearities (DNL and INL) of the AD9222 are reported to be ±0.25 LSB and ±0.4 LSB, respectively. [DNL is the largest deviation from 1 LSB (Least Significant Bit = $1/2^{12} \approx 0.024\%$) between two analog voltages that correspond to two adjacent digital values.][INL is the largest deviation between the output and a linear fit across the full range.]

The ultimate resolution and non-linearity of charge measurements from the RE are comprised of the responses of all the aforementioned RE components. Without considering readout schemes, the largest contribution to nonlinearity is expected to come from the digitization of the pulse by the ADCs. However, the RE channels are generally linear within their charge resolution. The charge resolution is limited by the ADC chip at low charge (see below 500 ADC channels in Fig. 3.15). A contribution is also expected from the peak-finding process.

In principle, the RC feedback op-amp allows one to determine the charge of a signal by simply determining the peak of the output. The 40-MHz sampling frequency of the output from the CR-$(RC)^4$ pulse shaping circuits, which have 25-ns time constants, provides a determination of the peak with a downward bias between 0.0% and about 3.5%. Though a relative bias caused by differences in pulse shape should be reduced by the op-amp, the bias of the peak-finding process to underestimate charge is always present. However, the average bias is irrelevant due to channel calibration (see Section 4.1). Figure 3.12 shows a typical ADC distribution for a single input DAC value. The asymmetry toward lower values is of the expected magnitude and therefore attributed to the asymmetrical bias of the peak finding algorithm.

The linearity and resolution of the RE were measured and monitored using onboard DAC pulse generators. Pulse generator data are taken by shifters before each Physics run, about four times per week for all RE boards in all experimental halls, taking less than one minute per EH. The DAC pulses are square-shaped and 50 ns wide, generated at 1 kHz by a high-speed DAC (16-bit/400-MSPS ADI AD9726), and sent to a slow amplifier (op-amp) which outputs a signal of about 100-ns width that is then processed in the same ways as PMT signals. The DAC value represents the height of the input pulse and is scanned with

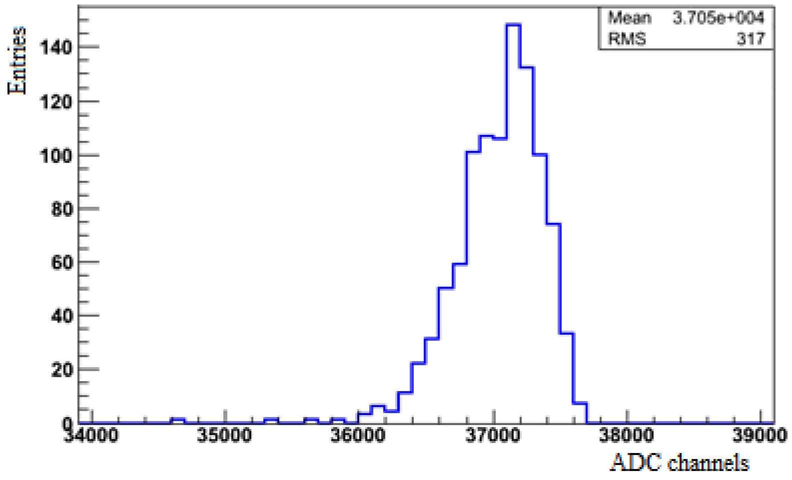

Figure 3.12 Distribution of ADC values from an identical input into a single RE channel.

each value repeated 1000 times.

- Fine range DAC values: [140, 310, 480, 650, 820, 1155, 1490, 1825, 2160, 2495, 2830, 3165, 3500, 3835, 4170, 4505]
- Coarse range DAC values: [12000, 15200, 21400, 27600, 33800, 40000, 46200, 52400, 58600, 64800]

With these data, the electronics gain (ADC/DAC) and linearity are determined. The average of the 1000 ADC values at DAC step i is denoted as μ_i. A line was fit to the μ_i ($a + b\mathrm{DAC}_i$) of each channel and no significant deviations from the lines were found.

The resolution of each RE channel was determined as the average of the standard deviation σ_i divided by the mean μ_i over each DAC step i:

$$\text{resolution} = \frac{1}{n}\sum_i^n \frac{\sigma_i}{\mu_i}. \tag{3-3}$$

The average resolution of all channels was (1.64 ± 0.17)%. The distribution of resolution for all channels in EH1-AD1 is shown in Fig. 3.13. The ADC resolution of the RE channels is generally stable to ±5% over time.

Here, differential nonlinearity (DNL) is defined as the deviation of residuals about the fit points:

$$\mathrm{DNL} = \sqrt{\frac{1}{n-2}\sum_i^n \left(\frac{\mu_i - (a + b\mathrm{DAC}_i)}{\mu_i}\right)^2}, \tag{3-4}$$

where $n = 16$ (10) for the fine (coarse) range. The average DNL of all channels was (0.215

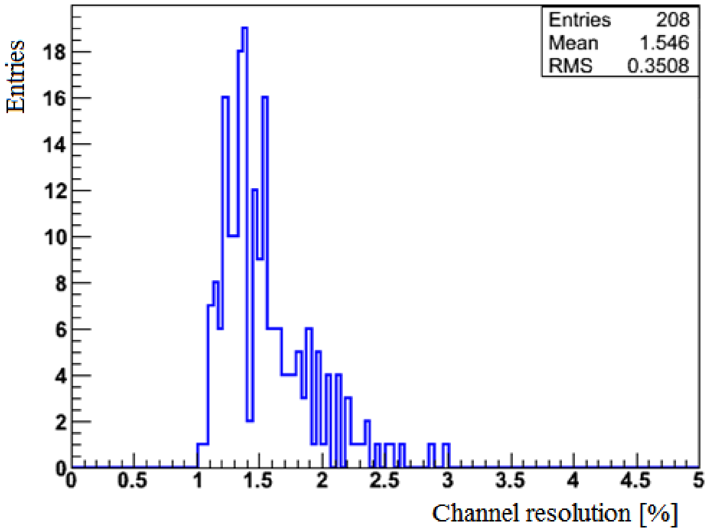

Figure 3.13 Distribution of RE channel charge resolution for all channels in EH1-AD1.

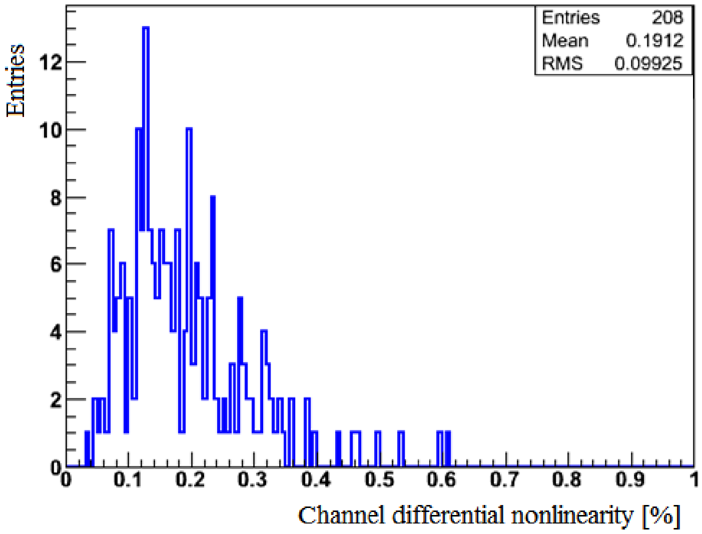

Figure 3.14 Distribution of RE channel differential nonlinearity for all channels in EH1-AD1.

± 0.090)%. The distribution of DNL for all channels in EH1-AD1 is shown in Fig. 3.14.

The total charge uncertainty of an RE channel is estimated as the quadratic sum of the above two measurements, which is predominantly due to the resolution. To properly propagate this charge uncertainty into energy uncertainty, the charge resolution (see Fig. 3.15) should be weighted with the charge spectrum of the event of interest; e.g., IBD prompt events.

Here, a highly conservative estimate of energy uncertainty is made. The observed energy of an event (E_{obs}) is proportional to the sum of all charges (Q_{tot}) in the event:

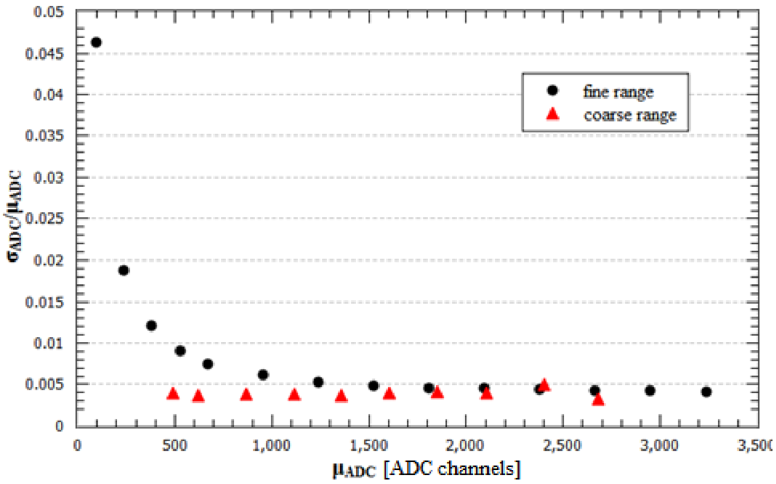

Figure 3.15 Relative charge resolution *vs*. charge for the fine and coarse ranges in a single RE channel.

$E_{\text{obs}} = cQ_{\text{tot}}$, where $Q_{\text{tot}} = \sum_i^N Q_i$ and N is the number of channels in the event. After error propagation and simplification through the assumptions of

- equal relative charge uncertainty on all channels and
- equal charge on all channels,

we obtain

$$\frac{\sigma_E}{E} = \frac{\sigma_Q}{Q}\frac{1}{\sqrt{N}}. \tag{3-5}$$

Very conservative values are $\frac{\sigma_Q}{Q} = 20\%$ and $N = 45$, which gives $\frac{\sigma_E}{E} = 3.0\%$. Using these numbers and an exponential decay fit of the fine range charge uncertainty in Fig. 3.15, a rough comparison with the expressions for energy resolution given in Section 4.4.3 is made. Adding the square of the maximum fractional uncertainty (which occurs around 1.5 MeV) with the square of the energy resolution, the new resolution is only about 3% (relative) greater. Thus, the RE charge resolution has very little impact on the energy resolution.

It was observed that the gain of the RE fine range is anticorrelated with the temperature of the RE. An excellent opportunity to observe this relationship occurred in the Spring of 2012 when the air conditioner in the electronics room of EH1 was replaced. After the replacement, the electronics room was 3 to 4°C cooler, as seen in Fig. 3.16, which shows the temperature of the VME crate *vs*. time from 2011/12/24 to 2012/07/28. Figure 3.17 shows the average fine range gain of EH1-AD1 and EH1-AD2 over the same time period. There is a clear jump in the gain corresponding to the drop in temperature. The anticorrelation between RE fine gain and RE (the VME crates') temperature is expressed as ΔGain/ΔT ≈ -0.2%/°C. The average gains of all eight ADs generally varied within 0.5% over time. The gains of individual channels varied within 0.5% to 1.5% over time. The temporal variation and temperature dependence of the RE is calibrated out for the fine ADC range as described in Section 4.1.

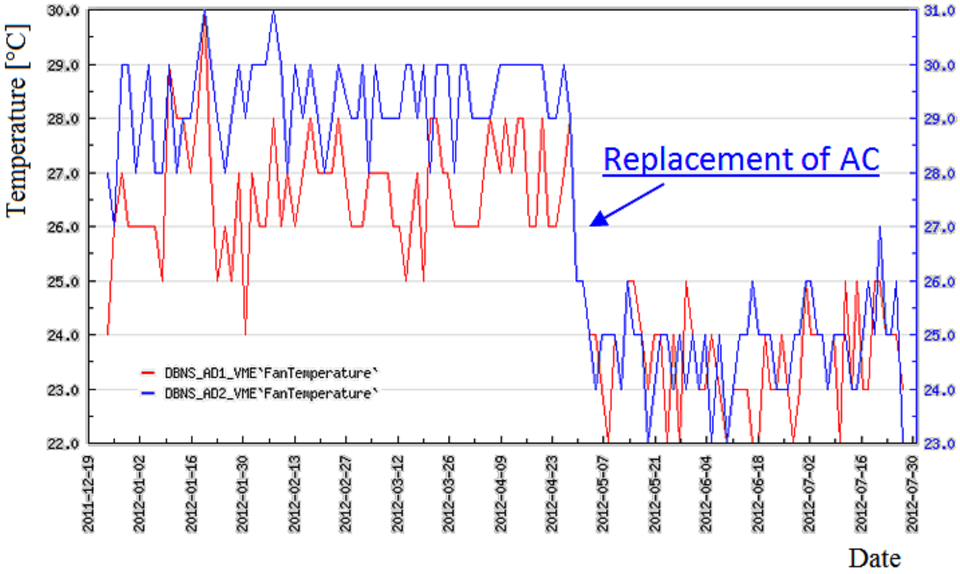

Figure 3.16 Temperature reported by the VME crates that house the readout electronics of EH1-AD1 (red) and EH1-AD2 (blue) from 2011/12/24 to 2012/07/28.

Though the RE themselves are linear in response, a nonlinear charge estimate can result from the distribution of the time at which secondary photons arrive at the PMTs. The slow fluorescence time scale of the scintillator can produce photons after 100 ns resulting in partial or complete exclusion from the charge integration of the RE. In addition, secondary photons that arrive relatively soon after the initial photon(s) will bias the integrated charge due to the overshoot of the initial PMT signal. The nonlinear behavior of a single channel was extracted from simulation and is shown in Fig. 3.18. Above one p.e., the curve is well modeled by an exponential decay. Another, simpler function was also fit for use in Section 4.4.3.

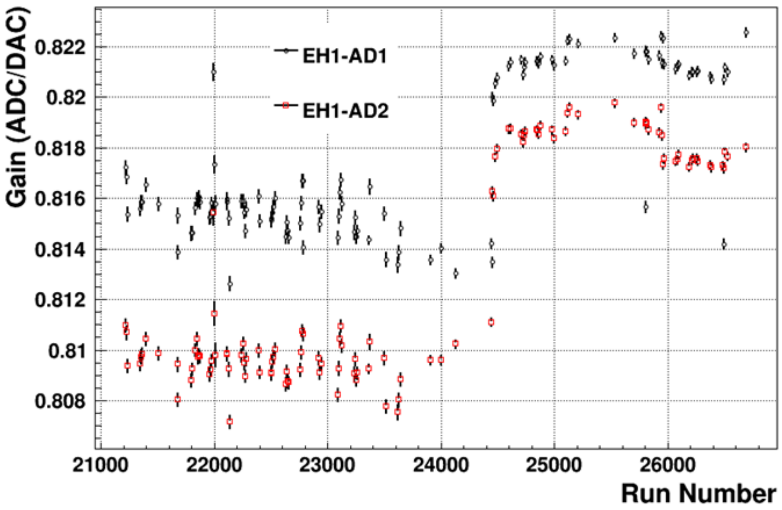

Figure 3.17 Average fine range gain of the EH1-AD1 (black) and EH1-AD2 (red) readout electronics from 2011/12/24 to 2012/07/28.

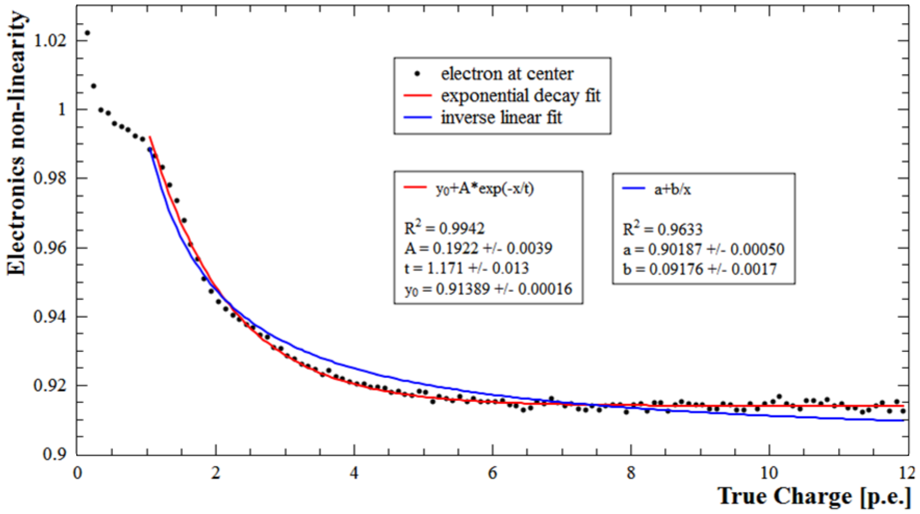

Figure 3.18 Readout electronics single-channel nonlinearity from simulation.

3.5 Readout Trigger

For ADs, output from the RE were recorded when either the number of PMTs with a pulse above the approximate 0.25-photoelectron channel threshold (N_{PMT}) was greater than or equal to 45 or the sum of all PMT pulses (Q_{sum}) was greater than or equal to approximately 65 photoelectrons. These trigger thresholds corresponded to approximately 0.4 MeV, accepting 100% of IBD positrons with more than 0.7 MeV deposited energy in scintillator[68].

For the IWS (OWS) at the near halls, output from the RE were recorded when either

$N_{\mathrm{PMT}} \geq 6$ (7) or $Q_{\mathrm{sum}} \geq 1.8$ (2.0) photoelectrons. These values were 6 (8) and 2.4 (2.9) photoelectrons at the far hall.

The trigger conditions were tested by the local trigger boards [69] during each cycle of an 80-MHz clock. If satisfied, the following 1 μs of data from all channels were recorded. The preceding 200 ns of data were also recorded, and used to estimate the baseline of each readout electronics channel, which was also recorded. The preceding data were also used to calibrate the gain of the PMT channels.

All physical interactions that led to a single trigger in a detector are designated as an “event”. For discussion purposes, the time of a trigger defines the time of the event.

3.6 Data Acquisition

The data acquisition (DAQ) system accepts data from the RE and trigger electronics and records them to disk. The design of the DAQ system is described in Ref. [70].

3.7 Data Sample

The data sample used in this analysis was acquired from December 24, 2011 to July 28, 2012, using six ADs (two ADs in EH1, one in EH2, and three in EH3), and, after installing the final two ADs in EH2 and EH3, from October 19, 2012 to November 27, 2013. Thus, the data sample spans 621 days: 217 days with 6 ADs and 404 days with all 8 ADs. Excluding the pause for AD installation, data acquisition was continuous with less than 3% of the time lost to occasional maintenance of the local facilities, primarily a nearby power station. Not counting weekly calibrations, special calibrations, and problematic data, the total time of data acquisition T_{DAQ} for each AD is listed in Tables 5.2 and 5.3. With the selection criteria described in Chapter 5, the nH and nGd analyses observed about 780000 and 1240000 IBDs, respectively.

Chapter 4 Characterizing the Antineutrino Detector

This chapter presents an analysis of the antineutrino detector (AD) response to deposited energies of reactor-$\overline{\nu}_e$ magnitude [O(MeV)]. Sections 4.1 and 4.2 describe how the energy scale and nonuniformity of an AD were measured. Section 4.3 describes how the position of an event was reconstructed. The subsequent majority of the chapter is devoted to the description of a generic energy response model of scintillation detectors that can be used in other experiments, and its application to Daya Bay ADs (Section 4.4). A thorough understanding of energy resolution is achieved through analytical derivations, and is applied to Daya Bay ADs (Section 4.4.3).

4.1 Energy Scale Calibration

The energy scale was calibrated in two steps. One step determined the gain [ADC channel/photoelectron] of each PMT channel. The other step determined an “inverted” gain [MeV/photoelectron] of the scintillator. Finally, these gains were combined so that the data recorded in units of ADC channels were calibrated to a known value of MeV, E_0.

PMT channels were calibrated *in-situ* by fitting the single photoelectron peak in the PMT dark noise spectrum. The peak was fit with the convolution of Poisson and Gaussian distributions[59]. An independent method of gain calibration used low-intensity LED pulses and validated the *in-situ* method.

The inverse gain of the scintillator of each AD was calibrated *in-situ* with muon-induced spallation neutrons that captured on Gd throughout the GdLS volume. The two isotopes, ^{157}Gd and ^{155}Gd, release γ-cascades of 7.94 and 8.54 MeV, respectively, and were fit with two Crystal Ball functions[71] to extract the central energy values as described in Ref.[68]. An independent method used weekly deployments of the ^{60}Co γ source of ACU A at the center of each AD, and validated the *in-situ* method.

Occasionally, PMT channels were excluded from analysis due to failed high voltage channels and less significantly, due to high noise and bad gain. Given the small number of channels excluded at any single moment (typically one or none per AD), the energy scale calibration was made to include this impact to sufficient accuracy with a simple scaling of 1/192 per excluded PMT per AD.

The AD-uncorrelated uncertainty of the energy scale in the GdLS volume was estimated to be 0.2% using a number of different reference energies in all eight ADs[12]. The corresponding uncertainty in the full GdLS plus LS volume was estimated to be 0.5% using nH-IBD γ's and ^{212}Bi α's in all eight ADs.

4.2 Energy Reconstruction

As illustrated in Section 4.4.2.3, the energy scale of an AD increased by 10-15% from the center of the detector to the radial edge of the LS, and changed by 2-6% between the top and the bottom of the OAV, depending on the radial position. Corrections of energy scale as a function of position were applied to each AD using two-dimensional maps (z $vs.$ r) derived from spallation neutron-captures on Gd. These maps were extrapolated into the LS volume using spallation neutron-captures on H throughout the GdLS and LS volumes.

After correcting for nonuniformity, the energy is referred to as the "reconstructed" energy E_{rec}. It is this energy to which IBD selection criteria are applied. Energy nonlinearity calibrations were applied to the prediction and are described in Section 4.4.1 and the end of Section 3.4. Looking at nH γ's, the standard deviation of E_{rec} across an AD was observed to be about 0.6% (0.8%) for near-hall (far-hall) ADs. The larger variations for the far-hall ADs are statistical; i.e., due to the fewer number of spallation neutrons in the far hall. Though the model described in Section 4.4.2 achieved similar performance (1.0% standard deviation using only the $n = 1$ map [see Fig. 4.8]), it had not been adopted at the time of this study.

4.3 Position Reconstruction

Estimating the position of an event is necessary for correcting the spatially-nonuniform response of a detector. At Daya Bay, a single position was reconstructed for each event in an AD, where an "event" is defined at the end of Section 3.5. The method applied in this analysis used charge-pattern templates derived from a Monte Carlo simulation of positrons[68]. From the simulation, the charge-pattern, or average distribution of charge from the 192 PMT channels, was determined for each of 9600 voxels within the scintillating volumes, corresponding to 20, 20, and 24 divisions in r^2, z, and ϕ (where azimuthal symmetry was assumed to decrease statistical uncertainty). For each voxel, a χ^2 was calculated with the expected (from the templates) and observed charges from each PMT channel. The voxel with the smallest χ^2 was interpolated with its

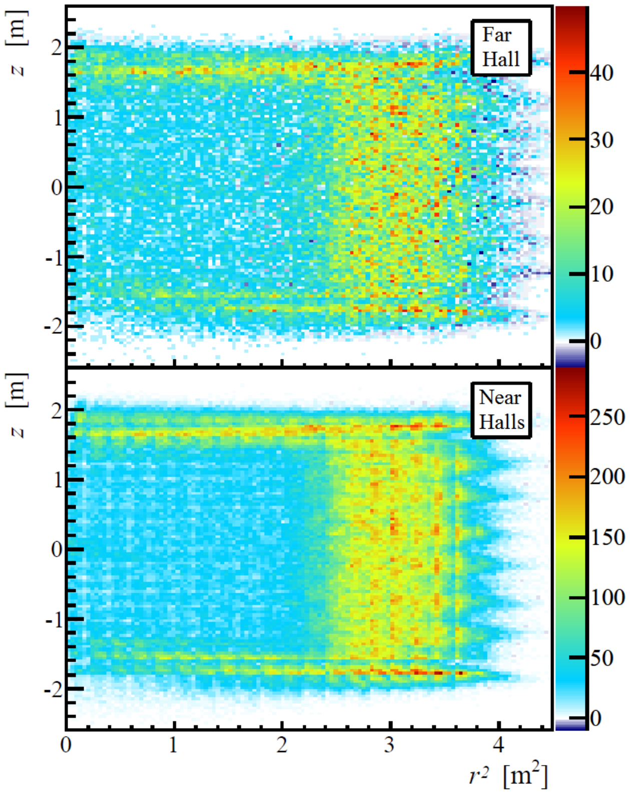

Figure 4.1 The reconstructed positions of all nH-IBD prompt events after subtracting the total accidental background sample for the far (top) and near halls (bottom). The sparser distribution of events at the bottoms of the ADs is due to the presence of the acrylic supports below the GdLS volume.

nearest-neighbor voxels to obtain the reconstructed position. The reconstructed positions of all (621-days) nH-IBD candidate prompt events (see Chapter 5) are shown in Fig. 4.1, where a residual voxel grid is visible.

The resolution of the position reconstruction is determined by several factors, including the number of photons produced by the incident particle, the location of the particle, and the mean free path of the particle. Using simulation, the position resolution for a 2.2-MeV γ was estimated as the deviation of its reconstructed position about its center of energy-deposition. This deviation was about 12 cm in the r-ϕ plane and 13 cm in the z direction, in the LS volume. Given that the mean free path of a 2.2-MeV γ through LS is about 24 cm, it can be deduced that the average distance of the γ's energy-deposition positions from its center of energy-deposition is smaller than (roughly half of) the estimated resolution. Thus, the mean free path would contribute roughly one fifth of the resolution estimated for 2.2-MeV γ's. The impact of the number of photons is apparent through an approximate $1/\sqrt{E}$ dependence of the resolution, which was observed with simulation. From data, the resolution of the position reconstruction improved by about 40% from the center of a detector to the edge of the scintillating volume, and varied within a few percent vertically. This improvement is expected to be associated with the increase in detected photons with increase in radial position. An analogous improvement is observed for energy resolution (see Section 4.4.3). Using the ^{60}Co γ source in ACU C (near the OAV), the bias of the position reconstruction was estimated to be about four times less than the resolution, near the edge of the scintillating volume.

4.4 Detector Energy Response

This section describes the energy response of Daya Bay ADs in the context of a generic model of scintillation detectors. The model requires a sufficiently accurate description of detector geometry and reduces the energy response to a few parameters that can be simultaneously fit with data.

An expression for the observed energy E_{obs} explicitly depends on the initial and final energies of an incident particle in the scintillating volume (E_{init} and E_{fin}), and the position about which the particle deposits energy ($\mathbf{x}$):

$$E_{\text{obs}}(\mathbf{x}, E_{\text{init}}, E_{\text{fin}}) = E_0 \sum_{i=1}^{\text{channels}} RE\left(O_i(\mathbf{x}, Y(E_{\text{init}}, E_{\text{fin}}))\right), \tag{4-1}$$

where the functions Y, O, and RE represent the photon yield, optical response, and single-channel response of the readout electronics, respectively. E_0 is a calibration constant that converts the readout (e.g., in units of ADC channels) to units of energy at a particular set of input parameters E_{init}, E_{fin}, and $\mathbf{x}$, as discussed in Section 4.1. The response of Daya Bay's RE is discussed in Section 3.4. All of the other components are discussed here.

It is highly desirable to modify Eq. (4-1) such that it is not a sum over three nested functions but rather a product of three functions. This can be achieved with two approximations: treating Cherenkov photons with the same wavelength-dependence of transmission as scintillation photons and ignoring any position dependence of the RE response. From these approximations, the model is simplified to

$$E_{\text{obs}} = E_0\, RE(\text{p.e.})\, C(\mathbf{x})\, T_s(\mathbf{x})\, [Y_s + f\, Y_C](E_{\text{init}}, E_{\text{fin}}), \tag{4-2}$$

where Y is expressed with two components Y_s and Y_C (scintillation and Cherenkov photon yields), the optical response function O has been separated into two basic components C and T (photocoverage and phototransmission), and $RE(\text{p.e.})$ is the full-detector electronics response as a function of total incident charge.

Based on studies with simulation, the necessary approximations introduce negligible uncertainties to the current Daya Bay analyses. The approximations have partially disentangled nonlinearity (Y and RE) and nonuniformity (O), however the output of one component still depends on the input of another. For example, when applying the model to data (E_{obs}), the RE response should be corrected first, then optical nonuniformity, and finally, scintillator photon yield. At Daya Bay, first correcting the energy for nonuniformity introduces an error generally well below 1%; however, in cases of low energy and large radius, the effect becomes more significant. For example, for a 1.5-MeV β^- just outside the IAV ($r \approx 1.6$ m) at $z = 0$, reversing the order of the RE and O functions would introduce an approximately 0.66% difference in reconstructed energy E_{rec}. For reference, the uncertainties of energy scale for the GdLS volume and the full GdLS plus LS volume are 0.2% and 0.5%, respectively (see Section 4.1).

4.4.1 Photon Yield

The production of photons in an organic scintillator is often quantified with Birks' law[72], which is an empirical formula for the photon yield per distance traveled by the incident particle:

$$\frac{dY_s}{dx} = \frac{Y_{s,0}}{E_0} \frac{\frac{dE}{dx}}{1 + k_B \frac{dE}{dx}}, \tag{4-3}$$

where k_B is the Birks' constant of the scintillator and dE/dx is the energy loss (which depends on E) of the incident particle. For Daya Bay's scintillator, k_B is $O(0.1)$ mm/MeV.

In addition to scintillation, charged particles generate Cherenkov radiation above a well-defined energy threshold: $E = mc^2/\sqrt{1 - n^{-2}}$, where n is the refractive index of the scintillator (for electrons at Daya Bay, this corresponds to about 0.17 MeV). The photon yield per distance traveled per unit wavelength λ is[48]

$$\frac{d^2Y_C}{dxd\lambda} = \frac{2\pi\alpha z^2}{\lambda^2}\left(1 - \frac{1}{\beta^2 n^2(\lambda)}\right), \tag{4-4}$$

where α is the fine structure constant, z is the particle charge in units of electron charge, and β is the speed of the particle relative to the speed of light in vacuum.

The photons produced by these two modes of radiation have different wavelength (λ) distributions and thus, will attenuate (both scatter and absorb) differently through the scintillator. As a result, they may also have a different acceptance by the PMTs (see Fig. 3.7). The relative photon yield of Cherenkov to scintillation is denoted as $f(\lambda)$. As mentioned, one of the approximations necessary to disentangle the nonuniformity and the nonlinearity is that scintillation and Cherenkov photons have the same wavelength dependence. Thus, the fraction f is an average over the emission and transmission spectra of the scintillator, and the acceptance spectrum of the PMT photocathodes, for the two types of photons. For the Daya Bay ADs, f is found to be $O(1\%)$ by fitting to data. Such a small value introduces negligible uncertainty from the approximation. The resulting expression of the total photon yield is

$$Y = Y_s + fY_C. \tag{4-5}$$

Since experiments generally express measurements in units of energy and do not directly count photons, Y is expressed relatively by a numerator and denominator both in units of energy. With the detector calibrated at a particular energy, events that deposit a known amount of energy (different from the energy of calibration E_0) will have an apparent energy that is different from the known true energy. A curve of apparent energy E_{app} divided by true energy E_{true} as a function of true energy ($E_{\text{app}}/E_{\text{true}}\ vs.\ E_{\text{true}}$) provides a unitless expression of the photon yield Y that is analogous to $Y(E_{\text{true}})/Y_0\ vs.\ E_{\text{true}}$, where Y_0 is the photon yield at E_0.

The photon yield function $Y(E_{\text{init}}, E_{\text{fin}})$ explicitly contains both initial and final energies to account for cases where a particle may not begin or end its energy deposition in the scintillator, which is common at the boundaries of the scintillator volumes. It is assumed that the curve of $E_{\text{app}}/E_{\text{true}}\ vs.\ E_{\text{true}}$ is determined with $E_{\text{init}} = E_{\text{true}}$ and $E_{\text{fin}} = 0$, for example, by studying interactions at the center of the detector. This curve was produced at Daya Bay using numerous γ reference energies as shown in Fig. 4.2 (simulation was used to relate γ energy to the β model). To account for the case when $E_{\text{fin}} > 0$, the following treatment can be applied to the curve. As both Y_s and Y_C are determined by integrals over the particle's energy [see Eqs. (4-3) and (4-4)], the dependence of Y on the

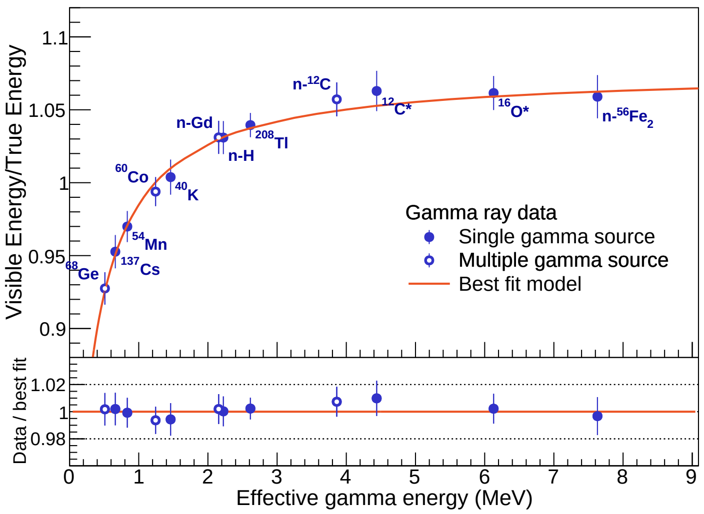

Figure 4.2 Ratio of apparent energy to true energy for both deployed and naturally-occurring γ-ray sources relative to the model of nonlinear scintillation and Cherenkov light. For sources that consist of multiple γ's, their mean energy is used. The best fit for the model is shown as a red line. The estimated nonlinearity contributed by the electronics has been removed from both the data and the model fit.[73]

initial and final energies is expressed as

$$E_{\mathrm{app}} = \frac{E_{\mathrm{true}}}{Y_0}\int_{E_{\mathrm{fin}}}^{E_{\mathrm{init}}}\frac{dY}{dE}dE = \frac{E_{\mathrm{true}}}{Y_0}\left(\int_0^{E_{\mathrm{init}}}\frac{dY}{dE}dE - \int_0^{E_{\mathrm{fin}}}\frac{dY}{dE}dE\right). \qquad (4\text{-}6)$$

Thus, the curve of $E_{\mathrm{app}}/E_{\mathrm{true}}$ $vs.$ E_{true} (or Y/Y_0 $vs.$ E_{true}) determined with $E_{\mathrm{fin}} = 0$ can be utilized twice to account for cases where $E_{\mathrm{fin}} > 0$.

The impact of this consideration to the nGd-IBD analysis is illustrated in Fig. 4.3, which shows the relative difference between simulated, reconstructed nGd-IBD prompt energy spectra with and without the treatment in Eq. (4-6). The only significant difference is at and below 1 MeV, which is due to the two 0.5-MeV annihilation γ's, which are more likely to exit the scintillator than the positron. This difference was found to be negligible when fitting for $\sin^2 2\theta_{13}$ and Δm^2_{ee}, which is also demonstrated by method E in Ref.[73]. The same illustration is shown for the nH-IBD analysis in Fig. 4.4, where the impact is significant across the entire spectrum due to the closer proximity of events to the outer scintillator boundary. Due to the small amount of doping of the GdLS, the GdLS and LS are assumed to have the same nonlinear photon yield within uncertainty.

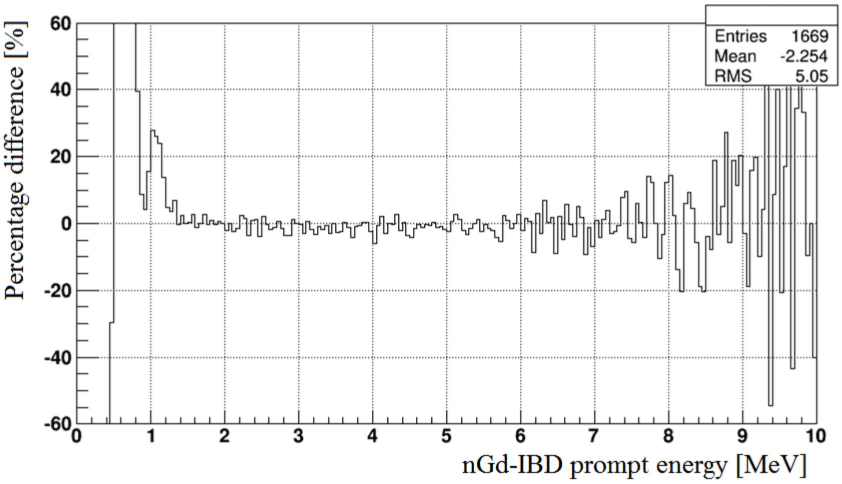

Figure 4.3 Percentage difference between simulated, reconstructed *n*Gd-IBD prompt energy spectra with and without considering the nonzero energy deposited outside the scintillators.

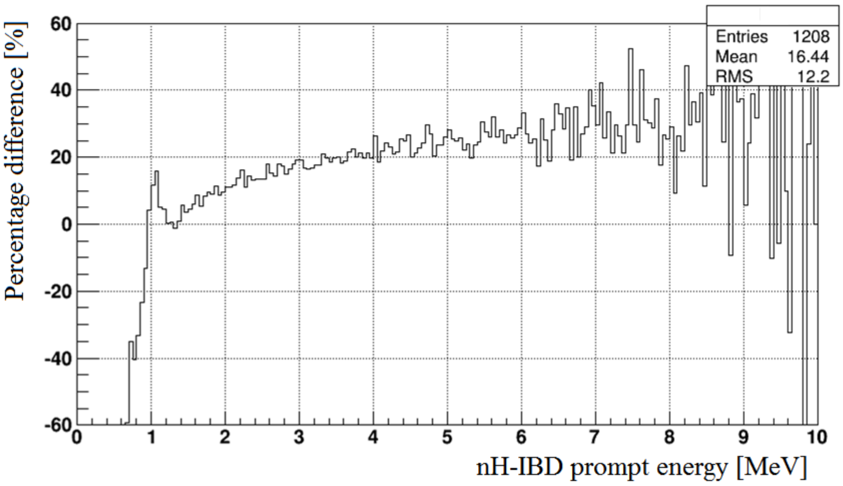

Figure 4.4 Percentage difference between simulated, reconstructed *n*H-IBD prompt energy spectra with and without considering the nonzero energy deposited outside the scintillators.

4.4.2 Optical Response

The optical response $O_i(\mathbf{x})$ is the probability that the photons propagate through the scintillator, and make contact with, and generate a signal in, PMT i. This probability is separated into two major components: phototransmission T (which is governed by an effective attenuation length) and photocoverage C (which is primarily geometric).

4.4.2.1 Phototransmission

The fraction of light that can reach a PMT is determined by the properties of the liquids and the distance to the PMTs. The probability that a photon of wavelength λ will travel a distance l through a medium of attenuation length $L(\lambda)$ follows Beer's law: $T(\lambda, l)$ = $\exp[-l/L(\lambda)]$. Now, Beer's law is applied to isotropically emitted photons, mimicking scintillation. The fraction of the N emitted photons that is transmitted from production vertex $\mathbf{x}$ to a surface that includes the sensitive surfaces of the PMTs is

$$T(\mathbf{x}) = \frac{1}{N}\sum_{i=1}^{N} \exp\left(\frac{-l_i(\mathbf{x})}{L}\right), \tag{4-7}$$

where L is an effective attenuation length (averaged over the emission spectrum of the scintillator and acceptance spectrum of the PMT photocathodes) and $l_i(\mathbf{x})$ is the distance traveled by the randomly-oriented photon i from production vertex $\mathbf{x}$ to a continuous surface that contains the PMT photocathode surfaces. The attenuation length L is separated from the photon distances $l_i(\mathbf{x})$ by expanding each exponential and grouping terms of the same order:

$$T(\mathbf{x}) = 1 + \sum_{n=1}^{\infty}\left(\frac{-1}{L}\right)^n m_n(\mathbf{x}), \qquad m_n(\mathbf{x}) = \frac{1}{N}\frac{1}{n!}\sum_{i=1}^{N}[l_i(\mathbf{x})]^n\,. \tag{4-8}$$

The sum $m(\mathbf{x})$ is determined at various positions $\mathbf{x}$ throughout the detector, and is therefore, a map. These maps can be determined with simulation as outlined in the next section. The number of moment maps $m_n(\mathbf{x})$ needed in the calculation of $T(\mathbf{x})$ is determined primarily by the size of the detector: if $l_i \ll L$ for nearly all i at all $\mathbf{x}$, then the first moment map ($n = 1$) is sufficient. In this case, the expression for T greatly simplifies:

$$T(\mathbf{x}) \approx 1 - \frac{1}{L}\frac{1}{N}\sum_{i=1}^{N} l_i(\mathbf{x}) \approx \exp\left(\frac{-\frac{1}{N}\sum_{i=1}^{N} l_i(\mathbf{x})}{L}\right), \tag{4-9}$$

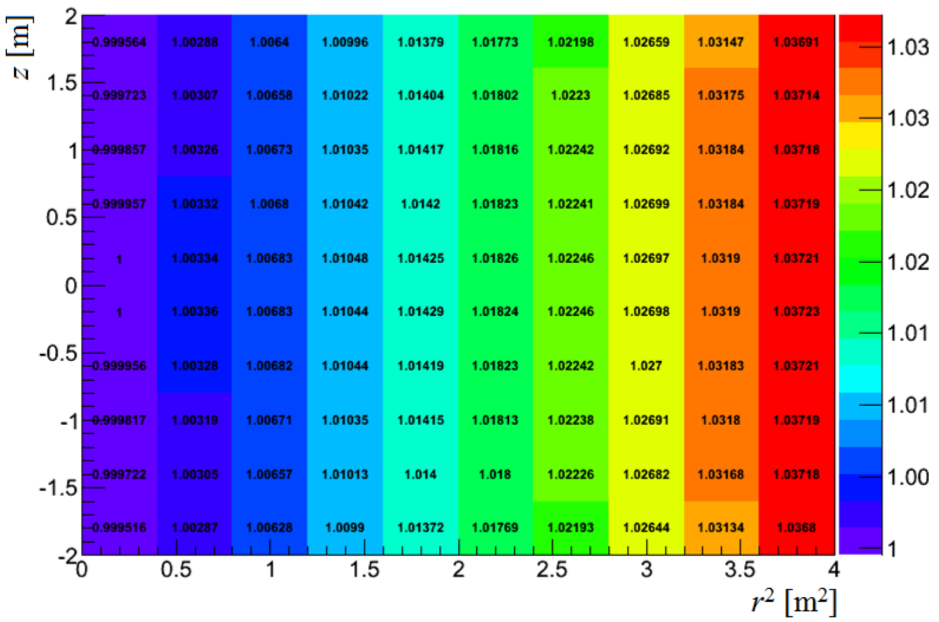

Figure 4.5 Phototransmission map fitted to nH γ's from all ADs using only the first ($n = 1$) moment map. This map is normalized to the value of the center cells ($z = 0$, $r = 0$). The color of a cell represents the fraction of light produced that can reach a PMT if an event occurs in that cell.

where the numerator of the exponent is simply the average distance $< l_i >$ traveled by the N photons. Approximating the attenuation length of Daya Bay LS as 12 m and with a mean photon distance of a little more than 2 m, $< l_i > /L \approx 0.2$. However, for events farthest from the center of a Daya Bay AD, l_i can be several meters; therefore, including a higher-order map would be appropriate. The fitted transmission map using only the n = 1 moment map is shown in Fig. 4.5. The effective attenuation length L was found to be consistent with 12 m.

In addition, detectors with more than one volume of scintillator, like the Daya Bay ADs, may use a transmission map that contains a distinct attenuation length for each volume. Following the same derivation, the transmission map of two distinct scintillators is expressed as

$$\begin{gathered} T(\mathbf{x}) = 1 + \sum_{n=1}^{\infty}\left[\left(\frac{-1}{L_1}\right)^n m_{1,n}(\mathbf{x}) + \left(\frac{-1}{L_2}\right)^n m_{2,n}(\mathbf{x})\right] + \sum_{a,b}^{\infty}\left(\frac{-1}{L_1}\right)^a \left(\frac{-1}{L_2}\right)^b m_{ab}(\mathbf{x}), \\ m_{j,n}(\mathbf{x}) = \frac{1}{N}\frac{1}{n!}\sum_{i=1}^{N}\left[l_{j,i}(\mathbf{x})\right]^n, \qquad m_{ab}(\mathbf{x}) = \frac{1}{N}\frac{1}{a!}\frac{1}{b!}\sum_{i=1}^{N}\left[l_{1,i}(\mathbf{x})\right]^a\left[l_{2,i}(\mathbf{x})\right]^b, \end{gathered} \tag{4-10}$$

where $a \geq b \geq 1$ and $l_{j,i}$ is the total distance of the ith path through the jth medium such that $l_{1,i} + l_{2,i} = l_i$. The nth-order transmission map consists of $m_{1,n}$, $m_{2,n}$, and all m_{ab} for which $a + b = n$ (note that there are no m_{ab} for $n = 1$). For this fit, it may be appropriate to apply two distinct light yields, or energy scales, for the two distinct volumes.

Equation (4-10) may also be used to fit two distinct attenuation length components of a single scintillator; namely, the scattering and absorption lengths. An independent value could be fit for each component by setting $l_{1,i} = l_{2,i} = l_i$. Though two values may be obtained, it would not be clear which effective length component a value corresponded to.

The basic method presented in this section also allows the fit of L to data $vs.$ time, naturally accounting for changes in scintillator properties $vs.$ time.

4.4.2.2 Photocoverage

The total number of photons that hit a PMT is determined almost entirely by geometry; i.e., the total sensitive area of PMTs visible to the photons. It depends on the sizes and shapes of the detector and PMTs, and on the reflectivity of the detector components. Further, the efficiency of the PMTs may exhibit dependencies on the incident angle of the photons relative to the PMT photocathode, on the interaction position of the photons on the photocathode, and on the orientation of the PMTs relative to the local magnetic field. Depending on the level of detail of the simulation, a generated photocoverage map can include all of these effects. A pseudocode example of how to generate a photocoverage map using a simulation of a detector is given below. In the example, photons are used as geometric ray tracers.

1. Generate particles uniformly in the detector.
2. Loop over all photons the particles produce.
3. For each photon, loop over its vertexes, saving the position of its initial vertex.
4. If the physical process of a vertex is related to scattering *in the scintillator*, then skip the photon because it might have changed direction.
5. If the photon vertex interacted with or passed through a PMT photocathode, then count it as a ‘PMT’ photon.
6. If the photon reached the user-defined continuous surface that contains the PMT photocathode surfaces (as used for the phototransmission map), then count it as a ‘CAN’ photon (this includes PMT photons).
7. The photo-coverage map will be PMT/CAN as a function of position. (all other photons are discarded.)

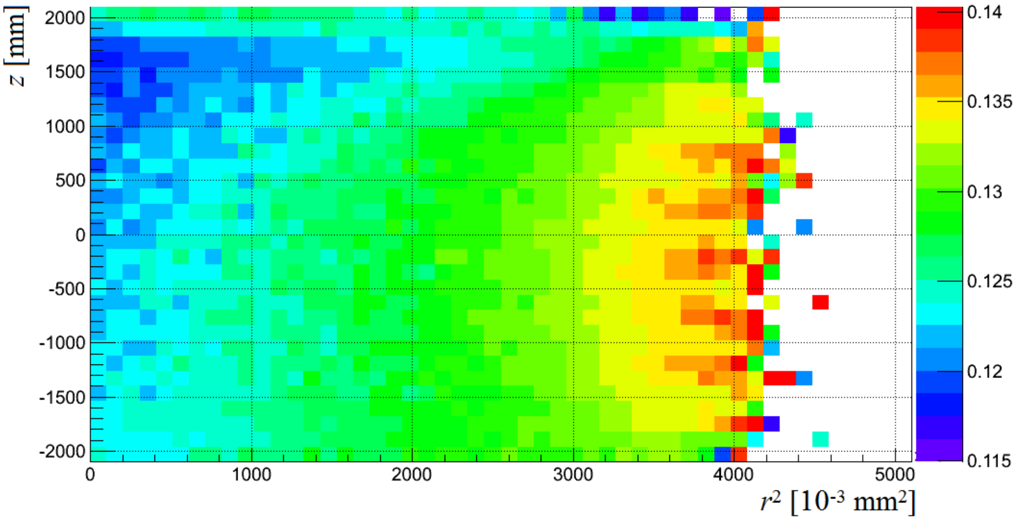

Figure 4.6   Photocoverage map of an AD generated with simulation requiring only the geometry of the detector. The color of a cell represents the fraction of light that will hit a PMT for an event in that cell.

The photocoverage map generated from the Daya Bay simulation is shown in Fig. 4.6.

4.4.2.3   Performance

The nonuniformity of nH-IBD γ's from all the ADs is shown in Fig. 4.7. The apparent pattern is very similar to the photocoverage map obtained in Section 4.4.2.2. This is expected as the spread of values across the photocoverage map is an order of magnitude

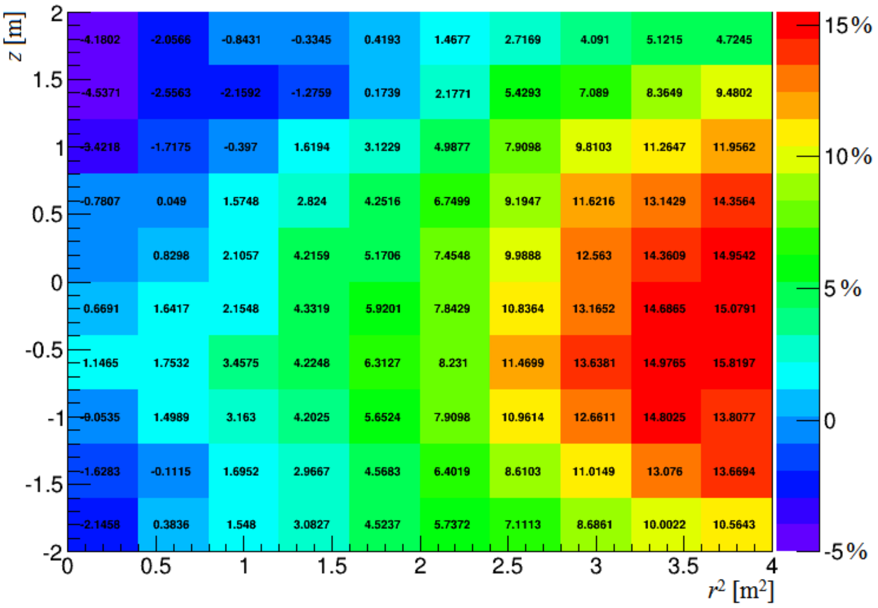

Figure 4.7   Spatial distribution of observed energy of nH-IBD γ's in all ADs. The values of the cells are relative to the center cell ($z = 0$, $r = 0$).

greater than that of the phototransmission map. After applying the photocoverage and phototransmission maps to Fig. 4.7, the reconstructed energy varies across the detector at the level of 1%, as shown in Fig. 4.8.

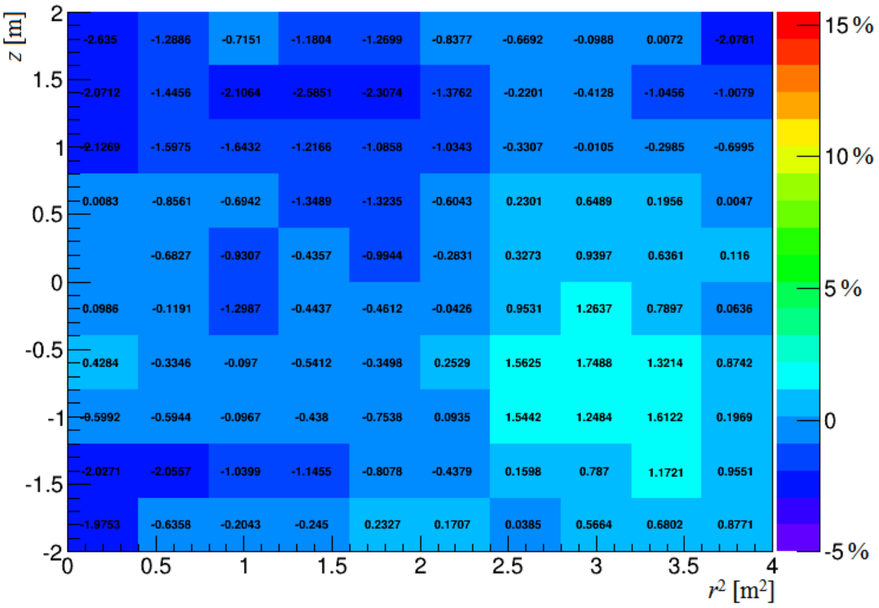

Figure 4.8 Spatial distribution of reconstructed energy of nH-IBD γ's in all ADs. The reconstruction utilized the photocoverage and fitted ($n = 1$) phototransmission maps. The values of the cells are relative to the center cell ($z = 0$, $r = 0$).

4.4.3 Energy Resolution

The energy resolution σ_E of a detector is a universal parameter that influences how precisely energy E can be measured. Furthermore, the nonuniformity of σ_E across a detector can be greater than that of E and therefore, important to characterizing the energy response of a detector. This section presents an analytical formulation of energy resolution that explains the factors that contribute to a detector's resolution.

As described in previous sections, the energy observed in a detector, E_{obs}, is generally obtained by summing the ‘charge’on each channel i and multiplying it by the calibrated values of each channel to a single p.e. (c_i [ADC/p.e.]), and the calibrated value of all channels N to a source of known energy (A [MeV/ADC]):

$$E_{\text{obs}} = A \sum_{i=1}^{N} c_i (s_i + n_i), \tag{4-11}$$

where each channel receives some amount of ‘charge’associated with the event, which is composed of the signal s [p.e.] and noise n [p.e.]. Equation 4-11 receives input expressed in units of p.e. because it is at this stage where the statistics are determined; i.e., where the signal is composed of the fewest number of units.

Applying error propagation to Eq. (4-11) and assigning Poisson errors for s and n, we obtain

$$\sigma_E^2 = \frac{\sigma_A^2}{A^2}E^2 + A^2\left[\sum_{i=1}^{N}\left(\frac{\sigma_{c_i}^2}{c_i^2}c_i^2(s_i+n_i)^2 + c_i^2(s_i+n_i)\right)\right]. \tag{4-12}$$

To obtain a tractable form we impose that all channels have the same σ_c, c, s, and n:

$$\frac{\sigma_E^2}{E^2} = \left(\frac{\sigma_A^2}{A^2} + \frac{1}{N}\frac{\sigma_c^2}{c^2}\right) + \frac{E_0}{E}. \tag{4-13}$$

The constant terms are the uncertainty in energy scale A and the channel resolution, and the statistical term contains the nominal energy of calibration $E_0 \equiv Ac\cdot$ 1 p.e. [MeV]. The assumptions of uniform values minimize the sum in Eq. (4-12), providing minimal estimates of the latter two of the three terms.

The previous derivation does not include the charge dependence of channel resolution. This is modeled as a Poisson error of the number of p.e. incident on the first PMT dynode:

$$\frac{\sigma_{c_i^2}}{c_i^2} = \frac{1}{s_i+n_i}\left(\frac{\sigma_{c_i}^2}{c_i^2}\right)_{\text{spe}}. \tag{4-14}$$

Substitution of this into Eq. (4-12) and imposing that all channels have the same resolution σ_c and calibration constant c, yields

$$\frac{\sigma_E^2}{E^2} = \frac{\sigma_A^2}{A^2} + \left[1 + \left(\frac{\sigma_c^2}{c^2}\right)_{\text{spe}}\right]\frac{E_0}{E}. \tag{4-15}$$

Now, the only constant term is the uncertainty in energy scale A, and the statistical term includes the s.p.e. channel resolution. Again, the assumptions of uniform values minimize the sum in Eq. (4-12), providing a minimal estimate of the statistical term.

From Eq. (4-15), a $1/E^2$ noise term can be revealed by factoring the statistical term:

$$\frac{\sigma_E^2}{E^2} = \frac{\sigma_A^2}{A^2} + \left[1 + \left(\frac{\sigma_c^2}{c^2}\right)_{\text{spe}}\right]\left(\frac{E_0}{E}\frac{1}{1+\frac{n}{s}} + \frac{E_0E_n}{E^2}\right), \tag{4-16}$$

where $E_n \approx AcNn$ [MeV]. This factoring has a negligible impact on the $1/E$ term since $1/(1{+}n/s)$ is roughly 0.998 for Daya Bay. The coefficient of the $1/E^2$ term is calculated by estimating n to be the product of a 300-ns charge selection window and a 5.5-kHz average PMT dark rate, yielding $(0.36\%)^2$. This value is negligible relative to that obtained from other considerations introduced below. Furthermore, considering the degenerate nature of its derivation, a $1/E^2$ noise term may be safely neglected.

The previous derivation [Eq. (4-15)] assumes no electronics nonlinearity. For Daya Bay, single-channel non-linearity can be roughly modeled as $1 + a/(s_i + n_i)$ with $a = 0.1$ (see Fig. 3.18). This alters Eq. (4-11):

$$E_{\text{obs}} = A \sum_{i=1}^{N} c_i(s_i + n_i)(1 + a_i/(s_i + n_i)). \tag{4-17}$$

Performing error propagation with the same assumptions as for Eq. (4-15) plus identical non-linearity among channels, yields

$$\frac{\sigma_E^2}{E^2} = \frac{\sigma_A^2}{A^2} + \left[1 + \left(1 + \frac{a}{s+n}\right)\left(\frac{\sigma_c^2}{c^2}\right)_{\text{spe}}\right]\frac{E_0}{E}. \tag{4-18}$$

As might be expected, non-linearity does not manifest directly in the statistical term; rather, it couples with the channel resolution. Finally, we approximate $s + n \approx E/NAc$ using the first-order expression of Eq. (4-11), yielding

$$\frac{\sigma_E^2}{E^2} = \frac{\sigma_A^2}{A^2} + \left[1 + \left(\frac{\sigma_c^2}{c^2}\right)_{\text{spe}}\right]\frac{E_0}{E} + aN\left(\frac{\sigma_c^2}{c^2}\right)_{\text{spe}}\frac{E_0^2}{E^2}. \tag{4-19}$$

Values of these parameters are given below.

The energy scale A depends on the position of calibration and so, the resolution curve should be determined at the same position. In addition, particles deposit energy over some distance. So, with a non-uniform detector response, there is a natural smearing of the energy scale and resolution, especially for γ's. This effect was estimated with a map of detector non-uniformity (Fig. 4.7) and the mean free path of γ's as a function of energy[74]: at the center of a Daya Bay AD, nH γ's acquire an approximate 0.5% smearing due to their 24-cm mean free path.

The effect of nonuniformity ⊕ mean free path was numerically added to Eq. (4-19) to obtain the final resolution curves shown in Fig. 4.9. Because of this effect, resolution

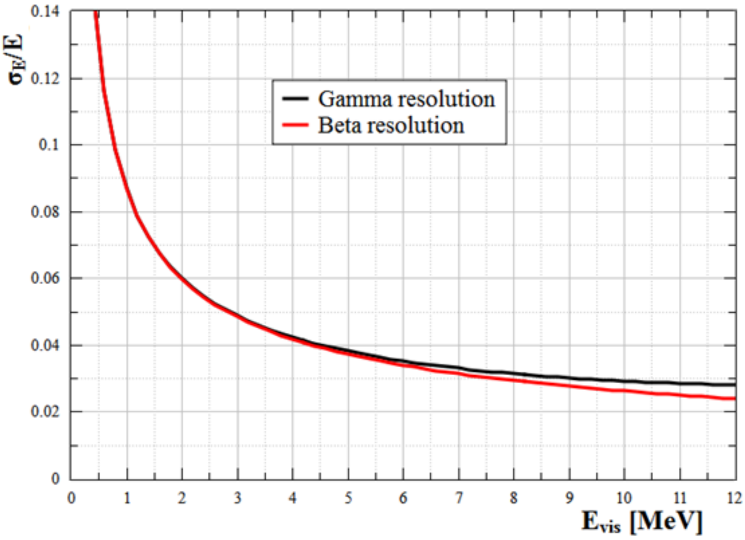

Figure 4.9 Energy resolution *vs*. observed energy calculated with Eq. (4-19). A numerical correction was applied to account for the effect of nonuniformity ⊕ mean free path, which produces distinct curves for β's and γ's.

curves are particle-dependent.

Similarly, nonuniformity corrections can depend on source type. For example, a bias could arise from applying the same nonuniformity correction to a single *vs*. multi-γ source: a single γ source will be reconstructed about one mean free path away from its origin while a source of two back-to-back γ's will be reconstructed at their origin. Therefore, the position used in the nonuniformity map will be different, resulting in a different nonuniformity correction. The bias of the example is expected to be about the size of the nonuniformity ⊕ mean free path effect. For example, *n*Gd γ's would not deviate from the β curve due to their average energy of about 2.2 MeV.

To inspect the formulation, we make use of various values of Daya Bay, which are given in Table 4.1. Substituting the values given in Table 4.1 into Eq. (4-19) and then correcting for the nonuniformity ⊕ mean free path effect, yields expected coefficients for the energy resolution of β's and γ's in a Daya Bay AD (the curves are shown in Fig. 4.9). These estimates are compared with fits to data in Table 4.2. The coefficients denoted as Data 1 are from calibration sources at the center of an AD, and IBD and spallation neutrons (*n*H and *n*Gd) distributed throughout the GdLS. The data are from Ref.[57] and shown in Fig. 4.10. The coefficients denoted as Data 2 are from various γ sources at the center of an AD.

The formulation here uses the energy as measured after calibration; i.e., E_{obs}.

Table 4.1 Basic parameters needed to analytically estimate the energy resolution of a detector: energy scale stability/uncertainty, single channel resolution (Section 3.2.3), energy scale in p.e./MeV, single channel nonlinearity, and the number of channels in the detector.

parameter	description	value
$\frac{\sigma_A^2}{A^2}$	energy scale uncertainty	$0.40\%^2$
E_0	energy scale	$\frac{1}{165}$ MeV
$\left(\frac{\sigma_c^2}{c^2}\right)_{\text{spe}}$	PMT channel resolution	$33\%^2 + 6\%^2$
a	RE nonlinearity	0.1
N	number of PMT channels	192

Table 4.2 Comparison of the three energy resolution coefficients from calculations and fits of Daya Bay data. The values of “Data1” and “Data2” are primarily based on single-γ sources and therefore are directly comparable with the values of “Calculated γ”.

	C_1 [%]	C_2 [%]	C_3 [%]
Calculated β	0.4	8.2	2.8
Calculated γ	1.2	8.0	2.9
Data 1	1.6	8.1	2.6
Data 2	1.5	8.7	2.7

However, the results were compared with those using E_{rec}, which is corrected for detector nonuniformity. Correcting energy nonuniformity would change the value of E and affect the nonuniformity $\oplus$ mean free path correction. This correction would also introduce an uncertainty from the position reconstruction and nonuniformity correction, which themselves are position-dependent (position reconstruction is also energy-dependent). It is noted that for either E_{obs} or E_{rec}, the value of energy scale A depends on the calibration source because of nonlinearities in detector response. Therefore, both the energy scale calibration source and its position should be reported along with an energy resolution formula or curve.

Finally, it is noted that the resolution improved by around 20% (relative) from the center of a Daya Bay detector to the edge of the scintillating volume; thus, this comparison is most appropriate for sources at the center of a detector. Nonetheless, the information here can be used to constrain fits of energy resolution. The assumptions of uniform values

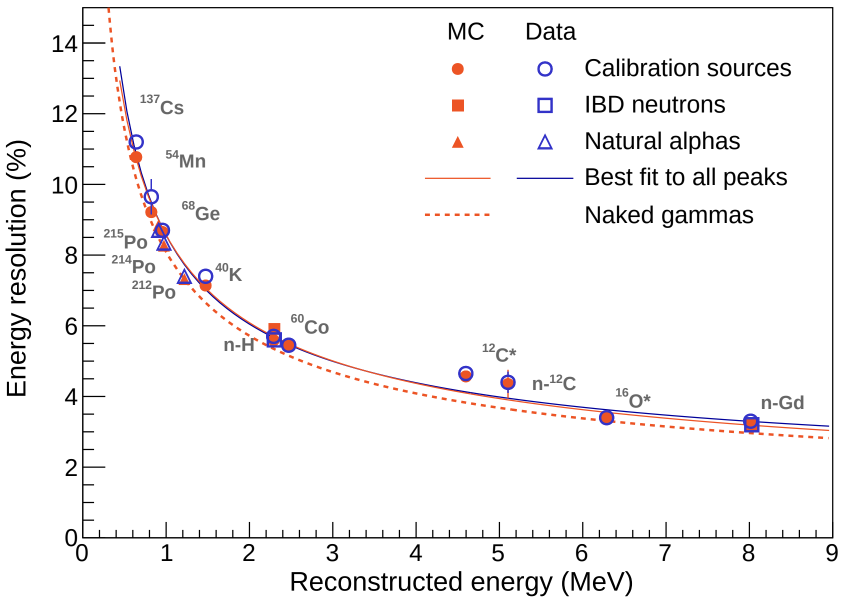

Figure 4.10 Energy resolution *vs*. reconstructed energy fit to various γ calibration sources, IBD neutron capture γ's, and natural α radioactivity in the scintillator[57]. "MC" denotes simulation of a source. The red dashed line excludes the hardware used to contain and deploy the γ sources.

made in simplifying the summations provide minimal estimates for the latter two of the three terms. Additionally, fits of resolution using the Crystal Ball function[71], as done for some of the data in Fig. 4.10, are generally biased upward[75]. Therefore, the formalism presented here should serve as useful lower bound for the energy resolution curve.

4.4.3.1 Conclusions

From analytical derivation, energy resolution can be expressed as

$$\frac{\sigma_E}{E} = \sqrt{a^2 + b^2\frac{E_0}{E} + c^2\frac{E_0^2}{E^2}}, \tag{4-20}$$

where a^2 represents energy scale variation, b^2 includes PMT channel resolution (typically, $b \approx 1.08$), c depends on RE nonlinearity (≈ 4.6 for Daya Bay), and E_0 is the inverse of the energy scale [p.e./MeV]$^{-1}$.

These three coefficients are altered by the convolution of detector nonuniformity and particle mean free path, which depends on particle type and energy. This gives a unique curve for each particle.

If E is corrected for nonuniformity, then uncertainties in the nonuniformity correction and vertex reconstruction should be considered. Furthermore, single-γ and multi-γ sources may require a different nonuniformity $\oplus$ mean free path correction.

Simple, conservative calculations of a, b, and c, as demonstrated here, can provide useful estimates or lower limits in fits of the energy resolution with data.

An additional observation worth noting is that increasing the number of PMTs (N) would reduce the two energy-dependent terms of Eq. (4-19) by $1/N$ (because $A \propto 1/N$ and E is independent of N), essentially improving the resolution by $1/\sqrt{N}$.

4.4.4 Conclusions

The generic energy response model of liquid scintillator detectors presented in this section can be applied to detectors of any shape and most practical sizes. Its application to the Daya Bay ADs results in a negligible difference to the nGd-IBD analysis relative to other methods[73]; however, its additional considerations are shown to be crucial for an nH-IBD spectral analysis, in particular, including E_{fin} in the estimate of scintillator photon yield. A nice feature of the model is that the energy scale and nonuniformity can be simultaneously fit to experimental data with as few as two parameters. This provides a data-based model that naturally accommodates changes in scintillator properties over time. Applied to Daya Bay ADs, reasonable performance is achieved. From analytical derivation, contributions to detector energy resolution are understood. Furthermore, a precise curve can be estimated with a few key input parameters that describe a detector. Reasonable agreement with measurements of Daya Bay ADs are demonstrated.

Chapter 5 IBD Candidate Selection

This chapter introduces the criteria applied to the data to identify IBDs (Section 3.1) caused by the reactor neutrinos produced at the Daya Bay Nuclear Power Station (Section 2.3). The criteria for two distinct analyses are presented: nGd and nH; i.e., when the IBD neutron is captured by gadolinium in the GdLS or by hydrogen in the LS, GdLS, acrylic, or MO. The signal purities (backgrounds) and efficiencies of these criteria and their corresponding detector-uncorrelated uncertainties are described in Chapters 6 and 7, respectively. The bulk of this thesis focuses on the nH-IBD analysis, which faces greater challenges in detector response modeling and accidental backgrounds. The nGd-IBD analysis spanning the same data period is reported in Ref.[12].

IBD candidates were selected from pairs of consecutive events in an AD, which, to suppress muon-induced backgrounds, did not include events within predefined time ranges of detected muons. The selection criteria for the nGd- and nH-IBD analyses are given in Table 5.1. First, AD events caused by spontaneous flashes of light from PMTs (PMT flashes) were removed as described in Section 5.1. Then, in the nH-IBD analysis, AD events were required to have $E_{\mathrm{rec}} > 1.5$ MeV to avoid low-energy backgrounds (see Section 5.2). After applying muon-event vetoes (see Section 5.3), AD events were grouped within a time window to distinguish double coincidences (see Section 5.4). The resulting prompt event was required to have $E_{\mathrm{rec}} < 12$ MeV while the resulting delayed event was required to have E_{rec} within three standard deviations of the fitted nH γ energy in each AD, for the nH analysis, and to have 6 MeV $< E_{\mathrm{rec}} <$ 12 MeV, for the nGd analysis. Finally, the nH analysis required that the distance between the reconstructed positions of the prompt and delayed events be within 50 cm to reduce uncorrelated double coincidences (accidentals), which dominated the collection of double coincidences (see Section 5.6). The resulting number of nH-IBD candidates (N_{DC}) from each AD is listed in Tables 5.2 and 5.3. Details of all the selection criteria are described in the following sections.

5.1 PMT Flashes

As observed in other experiments, light is sometimes spontaneously emitted from the circuit board of a PMT. At Daya Bay, the reconstructed energy of such emissions ranges from sub-MeV to more than tens of MeV, and typically occurs at a rate of 15 Hz

Table 5.1 Summary of IBD selection criteria for the *n*H and *n*Gd analyses. See the text for details.

	*n*H	*n*Gd
AD trigger	$N_{\text{PMT}} \geq 45$ OR $Q_{\text{sum}} \gtrsim 65$ p.e.	
20-cm PMT flash	$Ellipse < 1$	
5-cm PMT flash	$Q < 100$ p.e.	
Low energy	> 1.5 MeV	> 0.7 MeV
Detector latency	$< 2\ \mu s$	
WS muon (μ_{WS}) [IWS/OWS]	$N_{\text{PMT}} > 12/15$	$N_{\text{PMT}} > 12/12$
AD muon (μ_{AD})	> 20 MeV	
Showering AD muon (μ_{sh})	> 2.5 GeV	
WS muon veto	(0, 400) μs	(-2, 600) μs
AD muon veto	(0, 800) μs	(-2, 1000) μs
Showering AD muon veto	(0 μs, 1 s)	(-2 μs, 1 s)
Coincidence time (t_c)	[1, 400] μs	[1, 200] μs
Prompt energy (E_p)	< 12 MeV	
Delayed energy (E_d)	peak ± 3σ	[6, 12] MeV
Coincidence distance (d_c)	< 50 cm	NA

in each AD. One distinguishing feature of PMT flash events is that the PMT that flashes generally has a much larger detected charge than all other PMTs; therefore, a restriction is placed on the largest fraction of an AD event's total charge in a single PMT, q_{max}. Another distinguishing feature is due to the cylindrical symmetry of an AD: defining Q_i as the total charge in AD azimuthal quadrant i and defining Q_1 as being approximately centered on the PMT with q_{max}, a restriction is placed on $Quadrant \equiv Q_3/(Q_2+Q_4)$. By combining these two features into a single test statistic, this instrumental background is cleanly eliminated from the data before any other selections are applied, using the following criterion:

$$Ellipse \equiv \sqrt{Quadrant^2 + (q_{\text{max}}/0.45)^2} < 1. \tag{5-1}$$

This criterion was estimated to be > 99.99% efficient at selecting IBDs in the combined GdLS plus LS volume, using the Daya Bay simulation framework[56]. Given this negligible inefficiency, this criterion and this background are not discussed again. Flashes from the six 5-cm calibration PMTs were simply removed by restricting each of their charge output to be < 100 photoelectrons.

Table 5.2 Data summary for each near-hall AD. All daily rates are corrected with $\varepsilon_\mu \varepsilon_m$. T_DAQ is the DAQ time, ε_μ is the muon-veto efficiency, ε_m is the multiplicity selection efficiency, R_μ is the muon rate, R_s is the rate of uncorrelated single events, N_DC is the number of double-coincidence (DC) events satisfying all IBD selection criteria, N_Acc is the number of accidental DCs, N_Cor is the number of correlated DCs, R_Acc, R_Li9, R_FastN, R_AmC, and R_IBD are the rates of accidental, ^{9}Li/^{8}He, fast neutron, Am-C, and IBD (with all the backgrounds subtracted) DCs, and *n*H/*n*Gd is the ratio of the efficiency- and target proton-corrected R_IBD for the *n*H- and *n*Gd-IBD analyses. The differences in R_IBD among ADs in the same near hall are due primarily to differences in baselines to the reactors, and secondarily to differences in target mass.

	EH1-AD1	EH1-AD2	EH2-AD1	EH2-AD2
T_DAQ [d]	565.436	565.436	568.019	378.407
ε_μ	0.7949	0.7920	0.8334	0.8333
ε_m	0.9844	0.9845	0.9846	0.9846
R_μ [Hz]	200.32	200.32	150.08	149.80
R_s [Hz]	20.111	19.979	19.699	19.702
N_DC	217613	219721	208606	136718
N_Acc	26240±49	25721±49	25422±43	16365±29
N_Cor	191373±473	194000±475	183184±465	120353±449
R_Acc [d^{-1}]	59.31 ± 0.11	58.34 ± 0.11	54.54 ± 0.09	52.71 ± 0.09
R_Li9 [d^{-1}]	2.36 ± 1.02		1.73 ± 0.75	
R_FastN [d^{-1}]	2.11 ± 0.18		1.81 ± 0.17	
R_AmC [d^{-1}]	0.07 ± 0.04	0.07 ± 0.04	0.07 ± 0.03	0.07 ± 0.03
R_IBD [d^{-1}]	428.01 ± 1.48	435.49 ± 1.49	389.41 ± 1.25	384.03 ± 1.42
*n*H/*n*Gd	0.993 ± 0.007	0.993 ± 0.007	0.995 ± 0.007	0.995 ± 0.008

5.2 Low-energy Criterion

The low-energy criterion of the *n*Gd analysis was 0.7 MeV while that of the *n*H analysis was 1.5 MeV. Assuming all energy is deposited in scintillator, the minimum energy of an IBD positron event is 1.022 MeV (all energy coming from annihilation). Given that 0.7 MeV is more than three times the energy resolution (see Section 4.4.3) below this idealized IBD positron minimum energy, it is essentially 100% efficient at selecting positrons whose energy is totally absorbed in the detector; however, given the occasional energy deposition outside scintillator, a selection of > 0.7 MeV excluded 0.1% of IBD reactions.

The 1.5-MeV criterion of the *n*H analysis was selected solely to exclude $\beta\alpha$ decay

Table 5.3 Data summary for each far-hall AD. See the caption for Table 5.2.

	EH3-AD1	EH3-AD2	EH3-AD3	EH3-AD4
T_{DAQ} [d]	562.414	562.414	562.414	372.685
ε_μ	0.9814	0.9814	0.9812	0.9814
ε_m	0.9844	0.9841	0.9839	0.9845
R_μ [Hz]	15.748	15.748	15.748	15.757
R_s [Hz]	19.651	20.020	20.182	19.649
N_{DC}	56880	56106	59230	38037
N_{Acc}	29920±19	30065±20	32179±21	20427±15
N_{Cor}	26960±246	26041±244	27051±251	17610±196
R_{Acc} [d^{-1}]	55.07 ± 0.04	55.35 ± 0.04	59.27 ± 0.04	56.73 ± 0.04
R_{Li9} [d^{-1}]	0.19 ± 0.09			
R_{FastN} [d^{-1}]	0.16 ± 0.03			
R_{AmC} [d^{-1}]	0.03 ± 0.02	0.03 ± 0.02	0.03 ± 0.02	0.02 ± 0.01
R_{IBD} [d^{-1}]	49.24 ± 0.45	47.56 ± 0.45	49.44 ± 0.46	48.54 ± 0.55
nH/nGd	1.015 ± 0.012	0.981 ± 0.012	1.019 ± 0.012	0.987 ± 0.014

cascades from the estimation of the accidental background (see Section 6.1) [the α's were excluded from the IBD sample by the subsequent requirement on the energy of the nH γ (see Section 5.5)]. The decays were produced by the ^{214}Bi-^{214}Po-^{210}Pb and ^{212}Bi-^{212}Po-^{208}Pb chains, which originate from the naturally-occurring ^{238}U and ^{232}Th, respectively, throughout the detector. The latter chain produces an 8.78-MeV α, which, due to the greater quenching of α's in the scintillator (see Section 3.2.2), resulted in an apparent energy of $E_{\mathrm{rec}} = 1.26$ MeV. The former chain produces a 7.68-MeV α with an apparent energy of $E_{\mathrm{rec}} = 1.00$ MeV. Due to the high yield of these decays, excluding them reduced the uncertainty of the estimated accidental rate by an order of magnitude.

5.3 Muon-event Vetoes

To suppress the dominant background due to the long-lived spallation product ^{9}Li (Section 6.2) and the background from muon-induced spallation neutrons (Section 6.3), AD events were excluded from the analysis if they occurred within predefined veto time windows after cosmogenic muon events identified by the water shields or ADs. For the nH analysis, muon events from the ADs, IWS, and OWS that occurred within the 2-μs detector latency were grouped together to account for all events associated with cosmogenic muons. The start of the muon-veto time window was defined by the muon event with the earliest time in the group.

A muon event in a water shield is referred to as a μ_{WS} and was defined by requiring $N_{\text{PMT}} > 12$ (15) for the IWS (OWS). The efficiency of these selections to detect muons was essentially 100%, as determined relative to the ADs[67]. The nH-IBD analysis applied a higher threshold to the OWS (see Table 5.1) to remove correlated triggers that sometimes occurred $O(100)$ μs after an OWS event, due to electronics noise. The nGd-IBD analysis handled these triggers by slightly modifying the multiple-coincidence criteria (see Section 5.4) to have no overlap with a muon-veto time window.

In the nH analysis, an AD event with 20 MeV $< E_{\text{rec}} <$ 2.5 GeV that was grouped with a μ_{WS}, was defined as an AD muon event μ_{AD}. If $E_{\text{rec}} >$ 2.5 GeV, the event was instead defined as a showering AD muon event μ_{sh}. The total rate of these two types of muon events, R_μ, is listed in Tables 5.2 and 5.3 and shown in Fig. 5.1, for each AD.

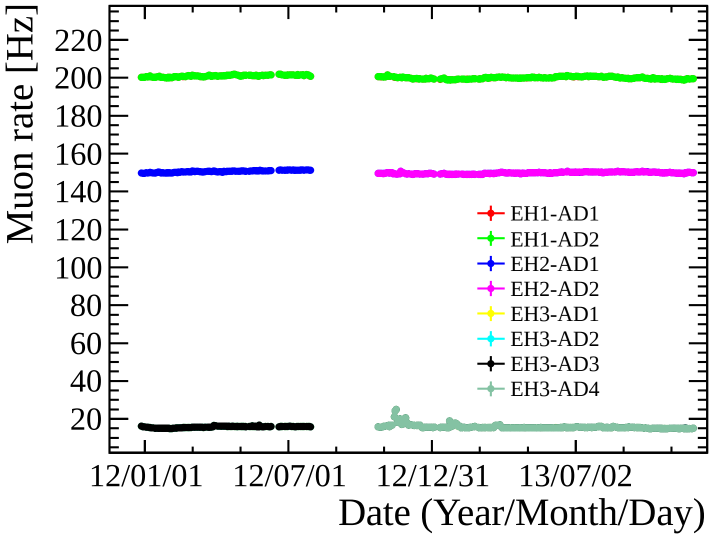

Figure 5.1 Muon event rate *vs.* time for each AD. ADs in the same hall have nearly identical rates.

AD events were excluded from the nH-IBD analysis if they occurred within a veto time window of 400 μs, 800 μs, or 1 s after a μ_{WS}, μ_{AD}, or μ_{sh}, respectively. The fraction of DAQ time remaining for IBD analysis after implementing these offline muon-vetoes ε_μ is listed in Tables 5.2 and 5.3, with typical values of 79%, 83% and 98% in EH1, EH2, and EH3, respectively.

5.4 Coincidence-Time Criteria

To identify a prompt positron event and a delayed neutron capture event, correlated AD events were selected using a coincidence time window. For the nH analysis, this window was $[1, 400]$ μs, which is about two times longer than the mean capture time of an IBD neutron on hydrogen in the LS and about 14 times longer than that in the GdLS. For the nGd analysis, this window was $[1, 200]$ μs, which is about seven times longer than the mean capture time of an IBD neutron in the GdLS. Given the data readout window of 1 μs (see Section 3.5), coincidence windows were initiated 1 μs after an event to distinguish prompt and delayed events. Solitary events are referred to as "singles" and were used to construct accidental background samples in the nH analysis (see Section 6.1). Only pairs of events, referred to as double coincidences (DCs), were selected as IBD candidates. If more than two events occurred within a coincidence time window, the events were excluded from further analysis. Also, if the first, or prompt, event of a DC occurred within a coincidence time window of a preceding event or muon-veto time window, the DC was excluded (this requirement was also applied to singles). The fraction of DAQ time remaining for IBD analysis after implementing these multiple-coincidence criteria ε_m was about 98.4% for each AD, and is listed in Tables 5.2 and 5.3. The expression used to calculate the multiplicity selection efficiency was derived as described in Ref.[76]:

$$\begin{aligned}\varepsilon_m = e^{-R_sT_c} \Big\{ & e^{-(R_s+R_\mu)T_c} \\ & + \frac{R_\mu}{R_s+R_\mu}[1-e^{-(R_s+R_\mu)T_c}] \\ & + \frac{R_s}{R_s+R_\mu}e^{-R_\mu T_c}[1-e^{-(R_s+R_\mu)T_c}] \\ & - \frac{R_s}{2R_s+R_\mu}e^{-R_\mu T_c}[1-e^{-(2R_s+R_\mu)T_c}]\Big\},\end{aligned} \tag{5-2}$$

where $T_c = 399$ μs is the duration of the coincidence time window and R_s is the rate of uncorrelated single events (which are uncorrelated events that satisfy the criteria of Sections 5.1-5.3; not singles, which exclude events involved in coincidences)

5.5 Delayed-Event-Energy Criteria

These criteria are different for the two IBD analyses given that the capture of a neutron on one of the two isotopes ^{157}Gd and ^{155}Gd will release a γ-cascade of 7.94 and

8.54 MeV, respectively, while the capture of a neutron on hydrogen produces a single γ of 2.22 MeV. The top panel of Fig. 5.2 shows the distribution of delayed energy *vs.* prompt energy for all DCs (selected with the longer coincidence-time window of the nH analysis) in all near-hall ADs after applying the coincidence-distance criterion (see Section 5.6). Belts for both the 2.22-MeV nH and 8-MeV nGd delayed events are obvious, with a large background of DCs concentrated below 3 MeV, which surrounds the nH belt. The measured mean of nH-IBD γ's was about 2.33 MeV, which is greater than the true value of 2.22 MeV because of the nonlinear detector response (see Section 4.2) and the calibration of the energy scale using nGd events (see Section 4.2). The clusters at about 1.5 and 2.7 MeV are due to the radioactive γ-decay of ^{40}K and ^{208}Tl decays, respectively. The belts between these clusters are dominantly due to the decay products of ^{238}U. To include the majority of nH-IBD events while excluding the majority of radioactive decays, nH IBDs were selected with a 3σ ($\approx$0.42 MeV) window around the fitted mean of the

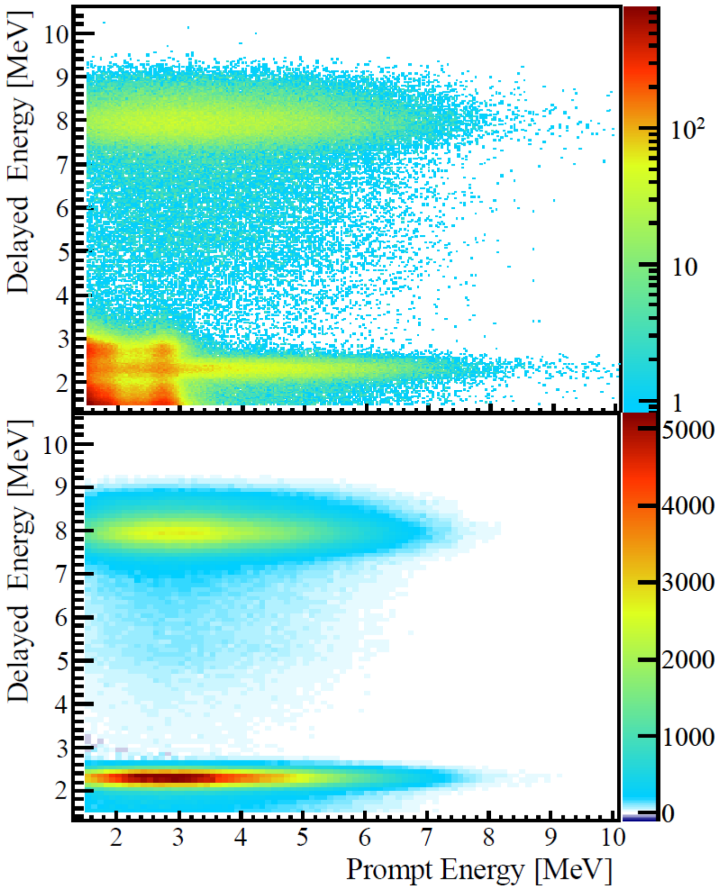

Figure 5.2 Top: delayed *vs.* prompt reconstructed energy of all double coincidences with a maximum 50-cm separation from all near-hall ADs. Bottom: delayed *vs.* prompt reconstructed energy after subtracting the total (621-day) accidental background sample for all near-hall ADs.

nH-IBD peak from each AD. This excludes γ's from ^{40}K. The peak was fit as described in Section 7.4, producing a mean and a standard deviation σ for each AD.

The selection of nGd IBDs was [6, 12] MeV, which is far removed from the radioactive background and was just above the energy of nC, which dominantly occurred in the LS volume.

5.6 Coincidence-Distance Criterion

Given the lower energy of nH γ's, the set of DCs in the nH-IBD analysis was largely comprised of accidental coincidences. Since the positions of such events are uncorrelated throughout the detector, the spatial separation of the reconstructed positions of the prompt and delayed events d_c was restricted. Requiring $d_c < 50$ cm essentially optimized the signal-to-background ratio, rejecting 98% of the accidental coincidences while excluding 25% of the IBDs (see Fig. 6.4).

The remaining accidental background was effectively subtracted as described in Section 6.1. Backgrounds from correlated events are described in the subsequent sections of Chapter 6. The efficiencies and uncertainties of the IBD selection criteria are described in Chapter 7.

Chapter 6 IBD Backgrounds

This chapter focuses on the accidental background and more briefly discusses the correlated-event backgrounds because of their secondary impact. After the accidental background was subtracted from the selected number of double coincidences to obtain the number of correlated double coincidences N_{Cor}, correlated backgrounds were subtracted to obtain the number of measured IBDs (N_{IBD}). In EH3 (EH1), $N_{\mathrm{IBD}}/N_{\mathrm{Cor}} = 99.2\%$ (99.0%) for the nH-IBD analysis. Correlated-event backgrounds consist of prompt and delayed events that are initiated by a single source and satisfy the IBD selection criteria. These backgrounds are dominantly from cosmogenic muon-induced ^{9}Li/^{8}He isotopes and spallation neutrons, and also neutrons from the ^{241}Am-^{13}C calibration sources that interact with the SSV and its appendages. The $^{13}\mathrm{C}(\alpha,n)^{16}\mathrm{O}$ background is due to naturally-occurring radioactive elements in the scintillator.

6.1 Accidental Background

Accidental backgrounds consisted of two uncorrelated AD events that satisfied the IBD selection criteria. Such events were overwhelmingly radioactivity from the materials around and within the detectors. The energy spectrum of this background is apparent below 3 MeV in the top panel of Fig. 5.2. Because the delayed event of an nH IBD is from a 2.22-MeV γ, which overlaps with this background spectrum, the rate of accidentals relative to the IBDs was typically > 50 times greater in the nH-IBD analysis than in the nGd-IBD analysis for the ADs in EH3, after applying all IBD selection criteria (see Table 5.1).

In the nGd-IBD analysis, the background was estimated as described in Ref.[56]. In the nH-IBD analysis, the background was estimated for each AD within each run (which typically spanned two to three days) by constructing accidental background samples (ABSs) from the singles (see Section 5.4) in a run. An ABS was constructed by serially pairing singles from the first half of the run with singles from the second half of the run. The resulting ABS contained $N_{\mathrm{ABS-tot}}$ accidentals. After applying the remaining IBD selection criteria (distance and energy), the ABS contained $N_{\mathrm{ABS-cut}}$ accidentals. The true value of $\varepsilon_{\mathrm{ABS}} \equiv N_{\mathrm{ABS-cut}}/N_{\mathrm{ABS-tot}}$ was determined as the Gaussian mean of the distribution of several hundred different pairing series of the singles. Figure 5.2 shows

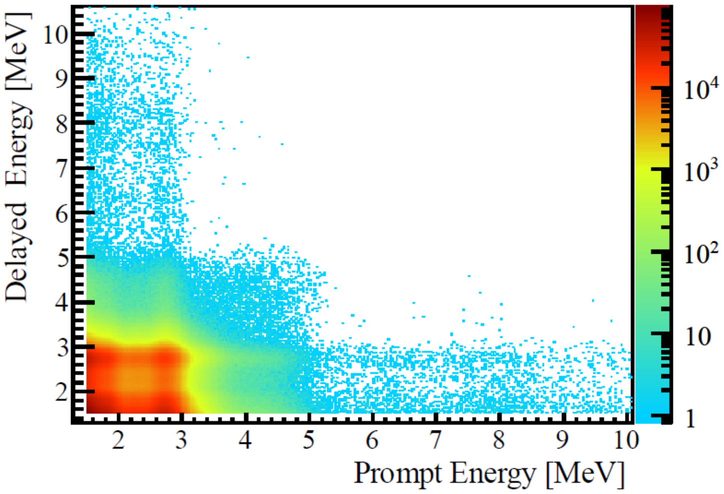

Figure 6.1 Total (621-day) accidental background sample for all near-hall ADs.

the energy distribution of all DCs (621 days) of all near-hall ADs (without applying the delayed-energy criterion), and Fig. 6.1 shows the energy distribution of the total ABS (621 days) of all near-hall ADs (after applying the coincidence-distance criterion). The accidental background was subtracted by scaling each ABS to a calculated number of accidentals (N_{Acc}) and then subtracting it from the number of DCs (N_{DC}), giving the energy distribution of correlated DCs (N_{Cor}), which are predominantly due to IBDs:

$$\begin{aligned} N_{\mathrm{Cor}} &= N_{\mathrm{DC}} - N_{\mathrm{Acc}}, \\ N_{\mathrm{Acc}} &\equiv R_{\mathrm{Acc}} \cdot T_{\mathrm{DAQ}} \cdot \varepsilon_{\mu} \cdot \varepsilon_{\mathrm{ABS}}, \end{aligned} \tag{6-1}$$

where T_{DAQ} is the DAQ time, ε_{μ} is the IBD selection efficiency of the muon veto criteria, and R_{Acc} is the coincidence rate of uncorrelated single events. The latter is expressed as[76]

$$\begin{aligned} R_{\mathrm{Acc}} &= R_s^2 \cdot T_c \cdot \varepsilon_m \\ &\approx R_s \cdot e^{-R_s T_c} \cdot R_s T_c e^{-R_s T_c}, \end{aligned} \tag{6-2}$$

where R_s is the rate of uncorrelated single events and ε_m is the multiplicity selection efficiency, both of which are defined in Eq. (5-2). The approximation of Eq. (5-2) substituted in the second line ($\varepsilon_m \approx e^{-R_s T_c} \cdot e^{-R_s T_c}$) applicable under the condition $(R_s + R_{\mu})T_c \ll 1$ and is valid to within 0.1% for $T_c = 399\ \mu\mathrm{s}$, $R_s = 20$ Hz, and the R_{μ} listed in Tables 5.2 and 5.3. This approximation was not used, but is shown here to demonstrate the basic components of the calculation: $e^{-R_s T_c}$ is the probability of no preceding event within T_c and $R_s T_c e^{-R_s T_c}$ is the probability of a subsequent event within

T_c. N_{DC}, N_{Acc}, and N_{Cor} are listed in Tables 5.2 and 5.3 for each AD.

The bottom panel of Fig. 5.2 shows the energy distribution of N_{Cor} for all near-hall ADs, where the nH γ peak has been cleanly extracted from the accidental-dominated DCs shown in the top panel of Fig. 5.2. The effectiveness of the subtraction is more clearly demonstrated in Fig. 6.2, which shows the energy spectra of the delayed events after subtracting the accidental backgrounds for all near-hall ADs and all far-hall ADs. The spectra are very similar between the two groups of ADs. Figure 4.1 shows the reconstructed positions of the N_{Cor} prompt events after subtracting the accidental backgrounds for all ADs in the far (top panel) and near halls (bottom panel). Fewer events are seen in the GdLS volume ($r^2 < 2.40$ m^2 and $|z| < 1.50$ m) because the majority of neutron captures in that volume are associated with Gd; otherwise, the positions are generally uniform throughout the GdLS and LS volumes.

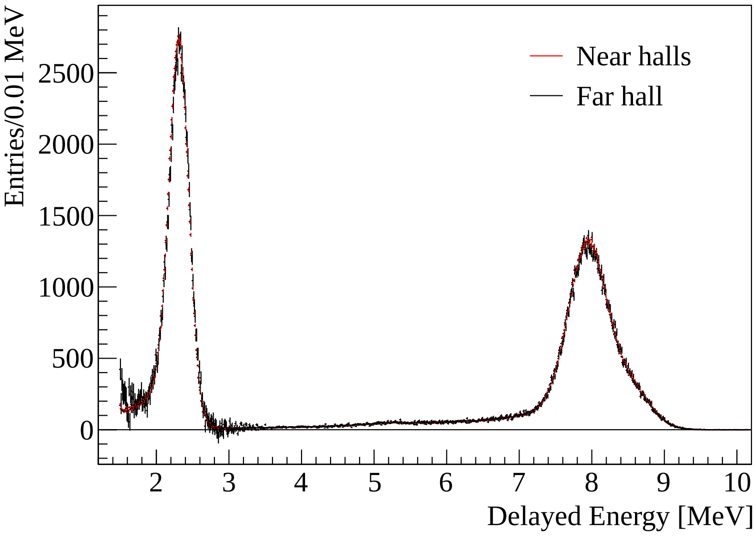

Figure 6.2 Reconstructed delayed energy after accidental background subtraction for all four ADs in EH1 and EH2 (red), and all four ADs in EH3 (black), where the EH3 spectrum has been normalized to the area of the EH1+EH2 spectrum. (621 days of data)

The uncertainty of N_{Cor} is comprised of the statistical uncertainties of N_{DC} and $N_{\mathrm{ABS-cut}}$, and the systematic uncertainty of R_{Acc}, which is governed by the uncertainty of R_s. The uncertainty induced by ε_m was insignificant: using Eq. (5-2) and conditions similar to those in EH1 ($R_s = 40$ Hz, $R_\mu = 200$ Hz, and $T_c = 399$ μs), $d\varepsilon_m = 3 \times 10^{-6} dR_\mu - 6 \times 10^{-3} dR_s$. Variations in R_s or R_μ from run-to-run induced negligible systematic uncertainty via this expression.

R_s was estimated for each run as the average of an upper and lower limit. The upper limit was the total number of AD events after employing the muon-event vetoes. These AD events were primarily singles, but included DCs and multiple coincidences. The lower limit was the number of singles plus the number of DCs that did not fulfill the coincidence-distance criterion. These DCs were primarily accidentals. Average values of R_s over the entire 621-day data sample are listed for each AD in Tables 5.2 and 5.3. The difference between the upper and lower limits was assigned to be the systematic uncertainty of R_s, which was propagated to R_{Acc} and resulted in 0.18%, 0.16% and 0.05% uncertainties of accidental rate in EH1, EH2, and EH3, respectively. The uncertainties for the near halls are larger because of the higher rates of IBD reactions from reactor antineutrinos, which enlarged their upper limits. Figure 6.3 shows R_s *vs.* time for each AD, where the downward trends started after the water shields were filled with water. During the first few weeks, R_s of the near-hall (far-hall) ADs decreased by less than 0.05 (less than 0.08) Hz per day. The near-hall AD rates stabilized earlier because their water shields were filled earlier. The uncertainty introduced to R_{Acc} by these trends of R_s was estimated to be less than 2×10^{-5}, which is more than an order of magnitude smaller than the uncertainty assigned in EH3. In addition, instantaneous increases of R_s were caused by muon-generated spallation products like ^{9}Li (Section 6.2) and spallation

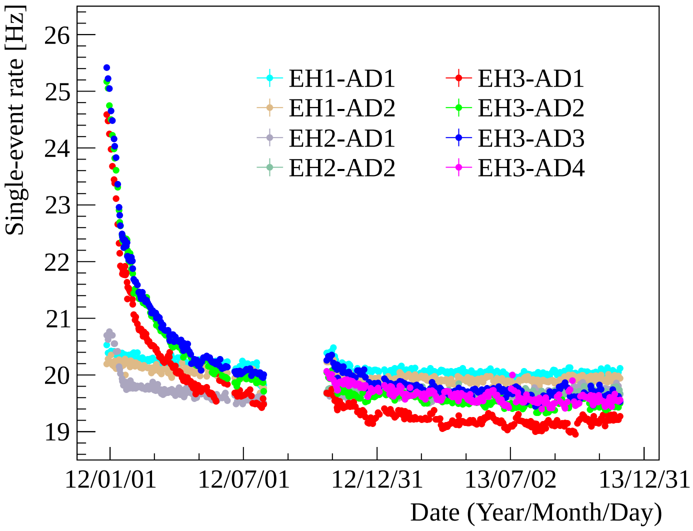

Figure 6.3 Rate of uncorrelated single events *vs.* time for each AD. Rates became stable several months after water shields were filled (in EH3, filling occurred less than one month before data-recording started).

neutrons (Section 6.3). From looking at R_s *vs.* time after muon-event vetoes, the influence of these spallation products was found to be negligible.

The subtraction of the accidental background was validated using two methods. The first method used the fact that the prompt and delayed events with larger separations were dominantly accidental coincidences. Thus, after subtracting the accidental background, the number of correlated DCs with large separations should be zero. The distribution of distance between the prompt and delayed events for DCs, accidentals, and correlated DCs, is shown in Fig. 6.4. The two upper panels of Fig. 6.4 show calculations of the relative difference between the measured number of double coincidences (N_{DC}) and the estimated number of accidentals (N_{Acc}), beyond 200 cm. The differences are consistent with zero. The bottom panel shows a constant fit to the nH IBD candidates (N_{Cor}) beyond

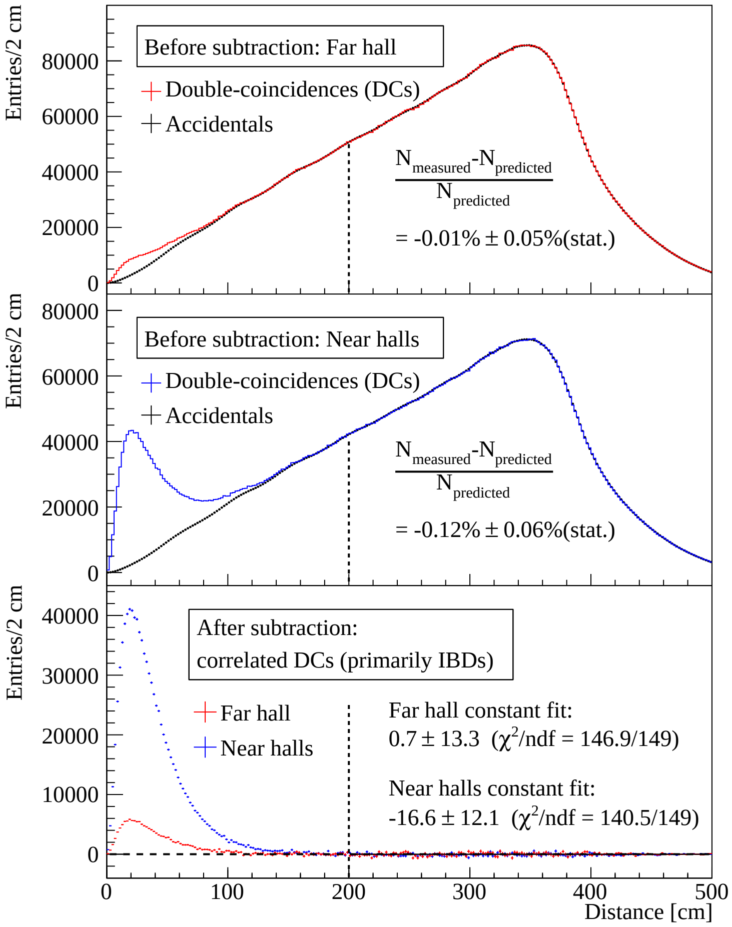

Figure 6.4 Distance between the prompt and delayed events for all measured double coincidences and for the estimated accidental backgrounds (black points) of the far hall (top panel) and near halls (middle panel). Bottom panel: the distance distributions after subtracting the accidental backgrounds for the near halls (blue) and the far hall (red). See text for details.

200 cm that is consistent with an expected fraction of about 0.05%, which was determined using Monte Carlo simulation. This fraction corresponds to a fit constant of about 0 (3) entries/2 cm for the far (near) hall(s).

The subtraction of the accidental background was similarly validated with the distribution of time between prompt and delayed events. The distribution of time between prompt and delayed events for DCs, accidentals, and correlated DCs, is shown in Fig. 6.5. The two upper panels of Fig. 6.5 show calculations of the relative difference between the measured number of double coincidences (N_{DC}) and the estimated number of accidentals (N_{Acc}), beyond 1000 μs. The differences are consistent with zero. The bottom panel shows a constant fit to the nH IBD candidates (N_{Cor}) beyond 1000 μs is consistent with an expected fraction of 0.7%, which was determined using Monte Carlo simulation. This

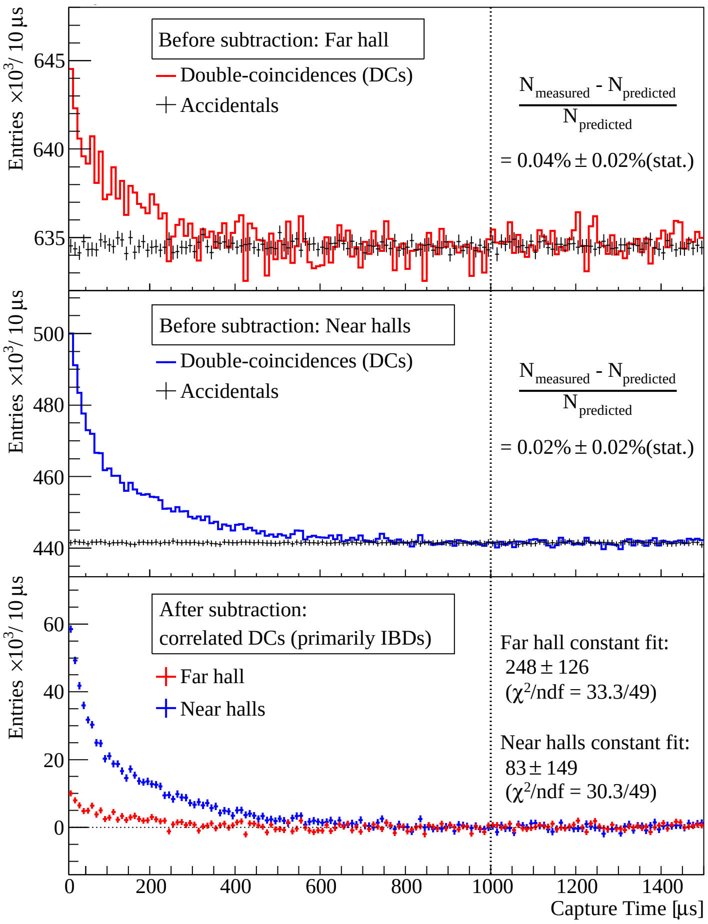

Figure 6.5 Time between the prompt and delayed events for all measured double coincidences and for the estimated accidental backgrounds (black points) of the far hall (top panel) and near halls (middle panel). Bottom panel: the time distributions after subtracting the accidental backgrounds for the near halls (blue) and the far hall (red). See text for details.

fraction corresponds to a fit constant of about 16 (110) entries/10 μs for the far (near) hall(s).

6.2 ^{9}Li/^{8}He Background

Cosmogenic muons and their spallation products interact with the ^{12}C in organic liquid scintillators to produce neutrons and isotopes via hadronic and electromagnetic processes. Among the muon-induced isotopes, ^{9}Li and ^{8}He β^--decay to neutron-unstable excited states, and then immediately eject a neutron. These β^--n decays can impersonate the prompt and delayed events of IBD reactions. The lifetimes of ^{9}Li and ^{8}He (257 and 172 ms, respectively) are longer than the muon-veto windows for a μ_{WS} or μ_{AD} (see Table 5.1), leading to a contamination of the IBD candidate sample. The temporal relation between ^{9}Li/^{8}He decays and preceding detected muons was used to determine the collective yield of the ^{9}Li and ^{8}He background $N_{\mathrm{Li/He}}$ in each hall. The distribution of time between the prompt event of a DC and its preceding muon was described by a formula following Ref.[77]:

$$\begin{aligned} N(t) \;=\;& N_{\mathrm{Li/He}}\left[r\cdot\lambda_{\mathrm{Li}}\cdot e^{-\lambda_{\mathrm{Li}}t}+(1-r)\cdot\lambda_{\mathrm{He}}\cdot e^{-\lambda_{\mathrm{He}}t}\right] \\ &+N_{\mathrm{BB}}\cdot\lambda_{\mathrm{BB}}\cdot e^{-\lambda_{\mathrm{BB}}t} \\ &+N_{\mathrm{DC}\not\mu}\cdot R_{\mu}\cdot e^{-R_{\mu}t}, \end{aligned} \tag{6-3}$$

where $\lambda_{\mathrm{isotope}} \equiv R_\mu + 1/\tau_{\mathrm{isotope}}$ and τ_{isotope} is the lifetime of the specific isotope (^{9}Li or ^{8}He), R_μ is the muon rate (which depends on the muon selection criteria), r is the fraction of ^{9}Li decays among ^{9}Li and ^{8}He decays, $\lambda_{\mathrm{BB}} \equiv R_\mu + 2/\tau_{\mathrm{B}}$, and N_{BB} and $N_{\mathrm{DC}\not\mu}$ are the numbers of ^{12}B-^{12}B coincidences and all other double coincidences (excluding those from cosmogenically-produced isotopes), respectively.

The yield of the beta-decaying isotope ^{12}B was about one order of magnitude greater than the combined yield of ^{9}Li and ^{8}He. With its lifetime of $\tau_{\mathrm{B}} \approx 29$ ms, accidental coincidences of ^{12}B-^{12}B originating from a single muon contributed mainly within the first about 50 ms of the time since the preceding muon distribution. The fitted value $N_{\mathrm{Li/He}}$ changed by up to 10% when including and excluding the ^{12}B term.

The fraction of ^{9}Li, r, could not be determined because of the comparable lifetimes of ^{9}Li and ^{8}He. However, measurements of ^{9}Li and ^{8}He yields from Ref.[78] indicate that r should be between roughly 85% and 100% at Daya Bay. Varying r within this range resulted in a 4% variation in the fitted value of $N_{\mathrm{Li/He}}$ in all halls. The fraction r was set to 90% because this value gave a χ^2 closest to the number of degrees of freedom in the fit of Eq. (6-3) using higher-energy muons in EH3.

To better estimate $N_{\mathrm{Li/He}}$, $N_{\mathrm{DC}\not\mu}$ was reduced by suppressing accidentals among the double coincidences. This was accomplished by augmenting the prompt-energy criterion from $1.5 < E_p < 12.0$ MeV to $3.5 < E_p < 12.0$ MeV. The fitted number of ^{9}Li/^{8}He was corrected with the efficiency of the augmented criterion with respect to the nominal criterion. This ratio was determined to be 74% by averaging measurements with muon energy $E_\mu > 1$ GeV from all three halls (E_μ is the detected energy associated with a muon crossing the detector, which was reconstructed with the nominal detector nonuniformity correction; thus, it is E_{rec}). The weighted average of the three measurements had a 5% statistical uncertainty. The systematic uncertainty was estimated as the difference between the average and a Monte Carlo simulation, thus accounting for backgrounds in the measurements. The simulation used ^{9}Li/^{8}He β-decay spectra calculated as those in Ref.[49]. The prompt-energy spectrum from the simulation is shown in Fig. 6.10, where it is normalized to $N_{\mathrm{Li/He}}$. The difference in efficiency between the average and the simulation was 6%, giving an 8% total uncertainty for the efficiency of the augmented E_p criterion.

The ^{9}Li/^{8}He background was estimated for three ranges of E_μ: 0.02-1.0 GeV, 1.0-2.5 GeV, and > 2.5 GeV. The highest E_μ range was defined identically to a μ_{sh}, which was vetoed for 1 s (see Table 5.1) and therefore contributed only $O(1)$% of the total ^{9}Li/^{8}He background. The lowest E_μ range was defined as such since it could not provide a reliable fit of ^{9}Li/^{8}He due to its lower signal-to-background ratio and higher R_μ: relative to the middle energy range, $N_{\mathrm{Li/He}}/N_{\mathrm{DC}\not\mu}$ was about 5 (10) times lower and R_μ was 14 (11) times greater, in EH1 (EH3).

To obtain a more reliable estimate of the ^{9}Li/^{8}He background in the lowest E_μ range, the signal-to-background ratio was increased and R_μ was reduced, by isolating the muons that produced ^{9}Li/^{8}He. Given that neutrons are generally produced along with the isotopes[78], every μ_{AD} without a subsequent neutron (defined as a 1.8-12 MeV event within 20-200 μs) was excluded. The fitted number of ^{9}Li/^{8}He was corrected with the efficiency of this altered μ_{AD} definition with respect to the nominal definition. Because this ratio could not be estimated for the lowest E_μ range, the ratio for the middle E_μ range was used as a proxy. This ratio was estimated to be about 69% (66%) in the far (near) hall(s). The background was assigned a 100% uncertainty for the lowest E_μ range, which corresponded to a 1σ lower bound of 35% (33%) for the efficiency of the altered μ_{AD} definition in the far (near) hall(s).

The number of ^{9}Li/^{8}He for both the lowest and middle E_μ ranges in EH1 and EH2 were determined from the combined data samples of EH1 and EH2. The muon energy spectra in EH1 and EH2 were similar[67] to the extent that their ^{9}Li/^{8}He yields per muon are expected to agree to $O(1)$%[79,80]. The E_μ spectra of the two near halls differed in scale by about 7%. This was due to the known 7% lower average gain of the high-charge range (see Section 3.4) of the EH2 electronics. After scaling the E_μ spectrum of EH2 by 7%, the difference between the spectra was indeed $O(1)$% across both E_μ ranges. This scaling induced negligible uncertainty to the fitted number of ^{9}Li/^{8}He. The muon rate R_μ used in the combined fit of the two halls was fixed to the DC-weighted average of their measured muon rates. Combining the uncertainties of the numbers of DCs (1%) and the measured muon rates (0.3%), the weighted average had an uncertainty of 0.2%. Varying R_μ by this 0.2% uncertainty in Eq. (6-3) produced a 27% change in the number of ^{9}Li/^{8}He for the middle E_μ range. The lowest E_μ range was negligibly impacted by the 0.2% uncertainty because its muon rate was reduced as described above. Finally, the fitted number of ^{9}Li/^{8}He was distributed among the near halls according to their rates of measured muons (after scaling EH2) multiplied by their DAQ times.

Figure 6.6 shows two examples of fits to the time since the preceding muon [see Eq. (6-3)] without the ^{12}B term for $E_\mu > 1.0$ GeV. The red areas correspond to the ^{9}Li/^{8}He DCs and the green areas correspond to the non-cosmogenic DCs. The plots use wider bins than the actual fits, for presentation purposes.

Uncertainties were from statistics, the contribution of ^{12}B, the fraction of ^{9}Li r, the augmented E_p selection criterion, the altered μ_{AD} definition for the lowest E_μ range, and binning effects. The total uncertainty of the ^{9}Li/^{8}He background is the combination of all these components, and is dominated by statistical uncertainty.

The determined rate of background DCs due to ^{9}Li/^{8}He, and its uncertainty, is listed in Tables 5.2 and 5.3 for each hall. The rate was calculated by dividing the $N_{\mathrm{Li/He}}$ by $T_{\mathrm{DAQ}}\varepsilon_\mu\varepsilon_m$ and correcting for the efficiencies of the altered definitions of the μ_{AD} and E_p criteria.

Since the nH- and nGd-IBD analyses selected different data samples, and the efficiencies were estimated with distinct methods, the nH- and nGd-IBD analyses were

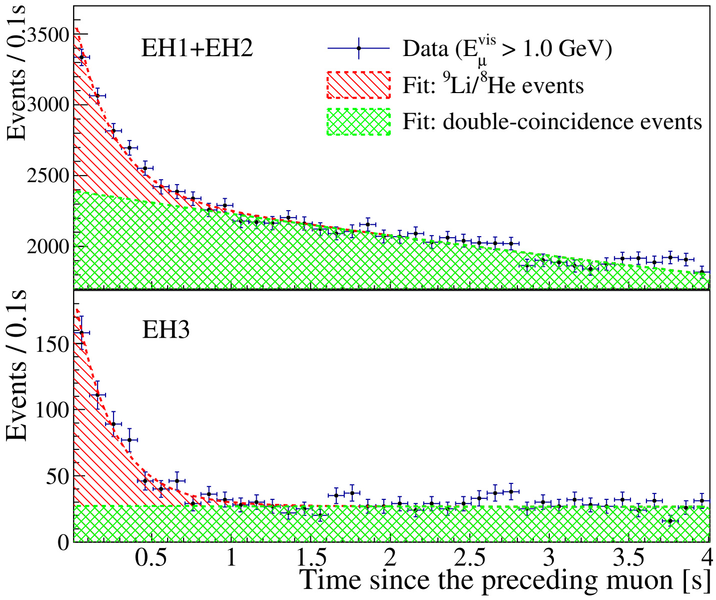

Figure 6.6 Examples of fits to the time since the preceding muon in EH1+EH2 (top) and EH3 (bottom) for E_μ > 1.0 GeV. The red area is the ^{9}Li/^{8}He component and the green area is the non-cosmogenic double-coincidence component.

assumed to share no correlation between their ^{9}Li/^{8}He background determinations.

6.3 Fast Neutron Background

Besides producing radioactive isotopes such as ^{9}Li and ^{8}He, cosmogenic muon interactions produce energetic neutrons via spallation. Upon reaching an AD, a neutron may scatter with hydrogen and then capture on hydrogen, creating a prompt-delayed coincidence. Due to the high efficiency of detecting μ_{WS}'s, neutrons that contribute to this background primarily come from the rock surrounding an OWS. The LS volume is more accessible than the GdLS volume to the externally-produced neutrons, as demonstrated in Fig. 6.7. Thus, this background is significantly higher for the *n*H-IBD analysis than the *n*Gd-IBD analysis.

A Monte Carlo simulation of muon-induced neutrons was performed to understand the measured energy spectrum. Initial kinetic energy and zenith angle distributions of the neutrons were generated in the water shields with an empirical parametrization for neutron production from cosmogenic muons[81] and the estimated average muon energy in an experimental hall[67]. The resulting prompt-energy spectra of the simulated neutrons are shown in Fig. 6.8. The presence of more events at lower energy in the LS volume is due to the lesser enclosure of the recoil protons within the LS volume: the protons

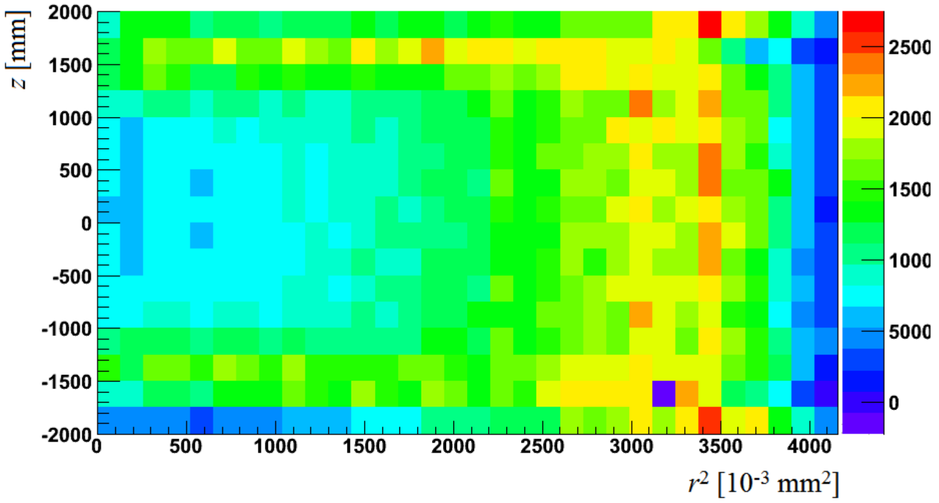

Figure 6.7 Spatial distribution of both *n*H and *n*Gd 'spallation' delayed-type events (delayed-type events satisfied either of the *n*H or *n*Gd delayed-energy criteria and followed WS- or AD-identified muons). There are fewer events at the center of the ADs (z = 0, r = 0).

that recoil from fast neutrons that capture in the LS volume are closer to the edge of the scintillating volume compared to those associated with fast neutrons that capture in the GdLS volume, and thus, are more likely to deposit less energy in scintillator.

To determine the spectrum of the fast neutron background, a sample of spallation neutrons was acquired by modifying two of the nominal IBD selection criteria: the upper prompt-energy criterion of $E_p < 12$ MeV was removed and the OWS muon-event veto was

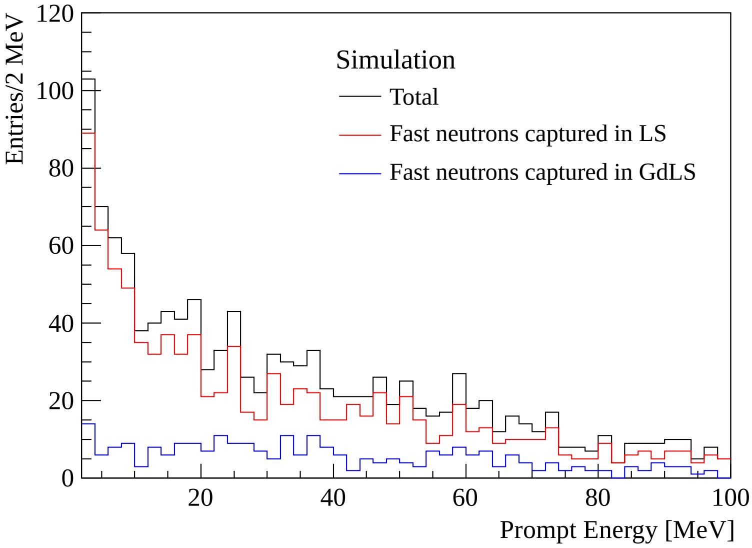

Figure 6.8 Prompt-energy spectra of simulated spallation neutrons produced in the IWS or OWS by cosmogenic muons. See the text for details.

excluded. To avoid confusing a spallation neutron with a muon event in an AD, muons identified with the IWS were still vetoed. In addition, prompt events were required to occur within 300 ns after an OWS-identified muon, and delayed events were required to occur at least 15 μs after the muon to exclude muon decays. The OWS-identified muon events were required to occur later than 1200 μs after a muon event in an AD or the IWS. The EH1 prompt recoil-energy spectrum of OWS-identified spallation neutrons is shown in Fig. 6.9. Figure 6.9 also shows the prompt-energy spectrum of IBD candidates without the upper E_p criterion and the spectrum acquired from the simulation. Both the OWS-identified and simulated spectra were normalized to the number of IBD candidates above 12 MeV, revealing consistent shapes among all three spectra.

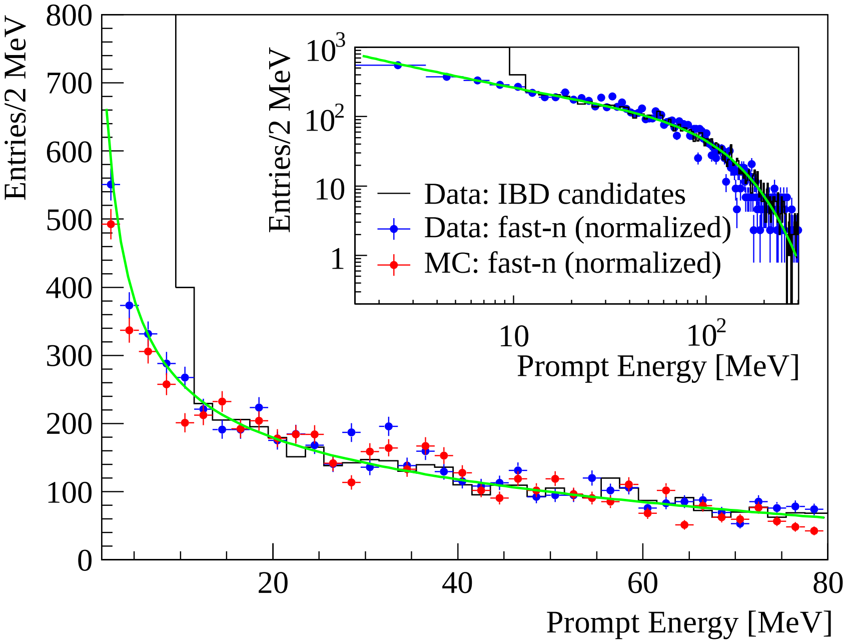

Figure 6.9 Reconstructed prompt recoil-energy spectra of fast spallation neutrons from OWS-identified muons (blue points), simulation (red points), and IBD candidates in EH1 with the upper E_p limit removed (black line). The former two spectra were normalized to the area of the extended IBD spectrum. The green curve is a fit to the extended IBD spectrum using a first-order power law (see text). The inset plot is a log-log scaling.

The prompt recoil-energy spectrum is plotted in a log-log scale in the inset of Fig. 6.9. The portion of the spectrum up to several tens of MeV is seen to be consistent with a power law [$N(E) = N_0 E^{-a}$], while there is a different energy-dependence at higher energies. The entire spectrum was found to be well described by a first-order power law, which is defined here as a first-order extension of the exponent of a power law:

$$N(E) = N_0 \left(\frac{E}{E_0} \right)^{-a-\frac{E}{E_0}} . \tag{6-4}$$

Equation (6-4) produced a χ^2 per degree of freedom close to 1 in the fit of each hall. Bin widths of 2 MeV were chosen for the near halls based on the constancy of the fit parameters and the χ^2 per degree of freedom. Due to the fewer events in EH3, the corresponding bin width was 3 MeV. The value of a was consistent among the three halls with an average of 0.690 ± 0.023. The value of E_0 was (110 ± 10) MeV for the far hall and averaged to (101.7 ± 2.1) MeV for the near halls.

The methods used to estimate the fast neutron background and its uncertainty are the same as in Ref.[12]. The background was estimated as the number of events with the nominal prompt-energy selection ($1.5 < E_{\text{rec}} < 12$ MeV) applied to the OWS-identified spectrum of each hall. The OWS-identified spectrum was first normalized (between 12 and 300 MeV) to the extended IBD spectrum from all the ADs in the hall. The systematic uncertainty was estimated using both the extended IBD and OWS-identified spectra. First, the extended IBD spectrum of each hall was fit between 12 and 300 MeV with the first-order power law [Eq. (6-4)]. Then, the difference was taken between the integral of the function and the number of events in the normalized OWS-identified spectrum, within the nominal prompt-energy selection window. The systematic uncertainty of each hall was assigned to be the largest relative difference among the three halls, which was 6% in EH3. In addition, the fit uncertainty, which included the statistical uncertainty, was about 6%, 7%, and 18% for EH1, EH2, and EH3, respectively. The results are listed in Tables 5.2 and 5.3 for each experimental hall.

Though the *n*H-IBD and *n*Gd-IBD fast neutron analyses used the same basic method, because of the different selection criteria and independent event samples of the analyses, there was no significant correlation between them.

6.4 Am-C Calibration Source Background

One of the calibration sources deployed from the three ACUs atop each AD was an ^{241}Am-^{13}C neutron source with a detected rate of about 0.7 Hz[82] when deployed. Neutrons from these sources inelastically scattered with the nuclei in the surrounding steel (SSV, ACU enclosures, *etc.*) and then captured on Fe, Cr, Ni, or Mn within the steel, producing γ's that could enter the scintillators and satisfy the IBD selection criteria. During the installation of the final two ADs in the summer of 2012, two of the three Am-C sources were removed (from ACU-B and -C) from the ADs in EH3, reducing this background by about 40% in EH3, relative to the previous analysis[15].

The background was estimated using a special Am-C source[83] that had a neutron emission rate approximately 80 times greater than the Am-C calibration sources. The special source was placed on the top of EH3-AD2 near ACU-B for about 10 days.

The number of DCs produced by the special Am-C source N_{Special} was estimated by subtracting N_{DC} of EH3-AD1 from N_{DC} of EH3-AD2 during the same period, yielding $N_{\text{Special}} = 137 \pm 41.6$.

The detected rate of the special Am-C source was scaled to the rates of the Am-C calibration sources of each AD using "delayed-type" events, which are singles that fulfill the delayed-energy criteria. However, substantial radioactive contamination was permitted into this sample of events via the relatively low energy of the nH γ selection. Therefore, the higher-energy nGd delayed-type events were used to avoid this contamination. The number of nGd delayed-type events due to an Am-C source $[N_{\text{AmC-dtype}}]_{n\text{Gd}}$ was estimated by the asymmetry of the vertical position distribution[83]. The number of DCs due to each Am-C calibration source N_{AmC} was estimated as

$$N_{\text{AmC}} = N_{\text{Special}} \left[\frac{N_{\text{AmC-dtype}}}{N_{\text{Special-dtype}}} \right]_{n\text{Gd}}, \tag{6-5}$$

where $N_{\text{AmC-dtype}}$ is counted over the whole 621-day data period. The nGd ratio in Eq. (6-5) was 0.23 for the near halls and 0.12 for the far hall. The uncertainty of N_{AmC} is comprised of the 30% statistical uncertainty of N_{Special} and a 40% systematic uncertainty in common with the nGd-IBD analysis from the differences in delayed-type event rates among the near- and far-hall ADs. This results in a total uncertainty of 50% for the Am-C background of the nH-IBD analysis. The rate of Am-C background DCs, which is N_{AmC} divided by $T_{\text{DAQ}}\varepsilon_\mu\varepsilon_m$, is listed for each AD in Tables 5.2 and 5.3. An exponential was used to model the prompt-energy spectrum of the Am-C background, which was determined from both the data with the special Am-C source and the simulation. The spectrum in EH3 is shown in Fig. 6.10. The Am-C background is smaller for the nH-IBD analysis than for the nGd-IBD analysis primarily because of the low-energy and coincidence-distance criteria.

This background had a 45% total uncertainty for the nGd-IBD analysis. Given the 40% systematic uncertainty in common with nH-IBD analysis, the Am-C background estimation has a correlation coefficient of about 0.7 between the two analyses:

$$\frac{40\% \cdot 40\%}{50\% \cdot 45\%} = 0.7. \tag{6-6}$$

6.5 ^{13}C(α,n)^{16}O Background

There were four dominant sources of α-decays in the liquid scintillator: the ^{227}Ac (in the GdLS), ^{238}U, and ^{232}Th decay chains and ^{210}Po, which is produced in the decay of ^{222}Rn. The ^{13}C(α, n)^{16}O background rate was roughly estimated for the nH-IBD analysis using the rates from the nGd-IBD analysis[12], and the ratio of the nH/nGd IBD selection efficiencies. The estimated rate for the nH (nGd) analysis in EH3 was approximately 0.02 ± 0.01 (0.05 ± 0.03) DCs per AD per day. The uncertainty of the ^{13}C(α,n)^{16}O background contributed insignificantly to the total uncertainty of $\sin^2 2\theta_{13}$ for the nH analysis (see Table 8.2).

6.6 Summary

The rates of the accidental and correlated backgrounds of the nH-IBD analysis are summarized in Tables 5.2 and 5.3. Their prompt-energy distributions are shown for EH3 in Fig. 6.10. The rates of nH IBDs after subtracting all the backgrounds are listed in Tables 5.2 and 5.3 for each AD.

Compared with the previous nH-IBD analysis[15], the absolute uncertainty of the dominant ^{9}Li/^{8}He background was reduced by about 30% due to increased statistics and various improvements in the method. Reductions in the uncertainties of the fast neutron and Am-C backgrounds resulted mainly from the improved method of estimation and fit of the full spectrum, and the removal of two-thirds of the Am-C sources from the far-hall ADs, respectively. Regarding the full-spectrum fit, it is noted that the first-order power law and its use in characterizing the fast neutron spectra at the three overburdens at Daya Bay can be useful for other experiments, particularly low-background experiments, and especially direct dark matter experiments (for example[84]).

The total uncertainty of backgrounds was reduced by 30%.

Compared with the nGd-IBD analysis, the fast neutron background was four to five times larger relative to the IBD rate in EH3, while each of the ^{9}Li/^{8}He and ^{241}Am-^{13}C backgrounds were equal within uncertainties, and the ^{13}C(α,n)^{16}O background was about half as large. The absolute uncertainty of the fast neutron background was four to five times

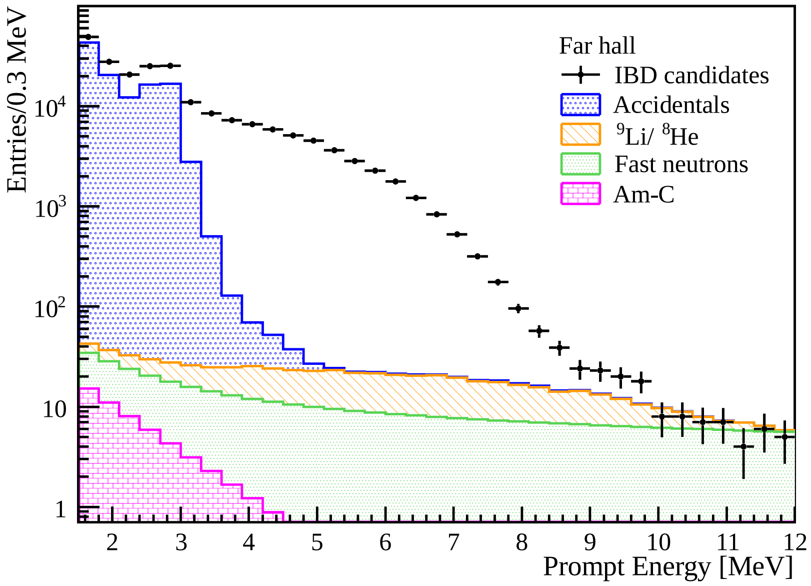

Figure 6.10 Reconstructed prompt-energy distributions of the measured double coincidences after IBD selection (black points) from all ADs in EH3, and their estimated backgrounds.

larger relative to the IBD rate in EH3, while the uncertainties of each of the ^{9}Li/^{8}He and ^{241}Am-^{13}C backgrounds were similar, and the uncertainty of the ^{13}C(α,n)^{16}O background was about half that of the nGd-IBD analysis. The impact of the uncertainties of the background estimations on the uncertainty of $\sin^2 2\theta_{13}$ is quantified in Table 8.2 at the end of Section 8.2.

The Am-C background determinations of the nGd- and nH-IBD analyses had a correlation coefficient of about 0.7, while the ^{9}Li/^{8}He and fast neutron background determinations were uncorrelated, and the ^{13}C(α,n)^{16}O background had negligible impact.

Chapter 7 IBD Selection Efficiencies

The criteria to select IBDs for both the nH and nGd analyses are listed in Table 5.1 and described in Chapter 5. The expected number of IBDs selected from one AD was estimated using Eq. (3-1), in which the efficiency-weighted number of target protons was calculated considering antineutrino interactions in the GdLS, LS, and acrylic volumes v:

$$N_\varepsilon = \varepsilon_\mu \varepsilon_m \left[\sum_{v}^{\text{GdLS,LS,acry.}} N_{p,v} \varepsilon_{E_p,v} \varepsilon_{T,v} \varepsilon_{E_d,v} \right] \varepsilon_D, \tag{7-1}$$

where ε_μ and ε_m are the muon-veto and multiplicity selection efficiencies of the AD, N_p is the number of target protons, ε_{E_p} and ε_{E_d} are the prompt- and delayed-energy selection efficiencies, and ε_T and ε_D are the coincidence-time and -distance selection efficiencies, respectively. It is noted that the prompt-energy selection ($E_{\text{rec}} < 12$ MeV) includes the low-energy criterion ($E_{\text{rec}} > 1.5$ MeV) for the sake of determining efficiency and uncertainty.

The numbers of target protons were estimated for each AD from measurements made before AD deployment. The muon-veto, multiplicity, and distance selection efficiencies were obtained from data. The prompt- and delayed-energy, and time selection efficiencies were ascertained with simulation using a predicted energy spectrum as described by Eq. (3-2). The simulation framework developed by the Daya Bay collaboration is based on GEANT4[85,86] and has been validated with numerous comparisons to data[56].

In a comparison of the IBD rates between the far hall and near halls, efficiencies and uncertainties correlated among all ADs are irrelevant. AD-uncorrelated uncertainties of the efficiencies, which quantify the identicalness of the ADs, were estimated by comparing data among all eight ADs. The uncertainties of ε_μ and ε_m were insignificant (see Section 5). The uncertainties of the other quantities in Eq. (7-1) are discussed in this Section. The contribution of IBDs in the MO volume is described in Section 7.6.

7.1 Uncertainty Metric

The AD-uncorrelated uncertainties were generally determined with data from some number of ADs, typically the four near-hall ADs (because of their larger samples) or

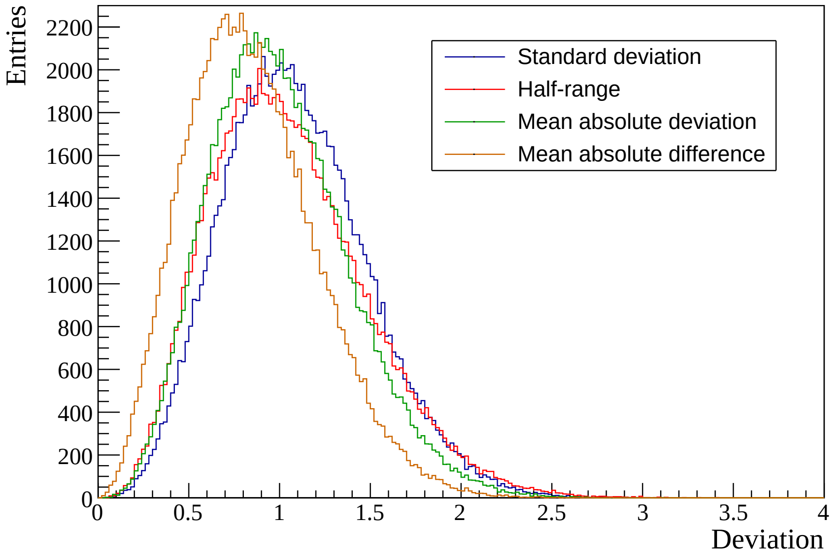

Figure 7.1 Distributions (in units of σ) of four estimators for σ in a standard normal distribution N when only 4 samples are taken from the distribution N. The sampling was repeated 100000 times.

all eight ADs. To accurately extract a realistic standard deviation from an expectedly Gaussian distribution for which we have no more than eight data, four basic metrics were evaluated. A standard normal distribution $N(\mu = 0, \sigma = 1)$ of the variable x was sampled n times, and the resulting x_i ($i = 1, ..., n$) were input to the four metrics. After repeating this sampling 100000 times, the distributions of the metrics were compared. The four metrics were defined as follows:

standard deviation $\sqrt{\frac{1}{n-1}\sum_i^n x_i^2}$

half-range $\frac{1}{2}(\max\{x_i\}\text{-}\min\{x_i\})$

mean absolute deviation $\sqrt{\frac{\pi}{2}}\frac{1}{n}\sum_i^n |x_i|$

mean absolute difference $\frac{1}{n^2}\sum_i^n\sum_j^n |x_i - x_j|$

Three basic cases were considered: when the number of ADs used was $n = 4$, $n = 5$, or $n = 8$. The four distributions are shown for the three cases in Fig. 7.1, Fig. 7.2, and Fig. 7.3, respectively. The abscissa is in units of σ; thus, an ideal estimator would have all of its values at 1. Among the three cases, the most distinctive feature is that the distribution of the half-range metric shifts upward (becomes a more conservative estimator) as n increases. For example, at $n = 120$, the distribution centers around 2.5. Thus, the half-range would be overly conservative in cases with larger n. However, for estimating AD-uncorrelated uncertainties at Daya Bay where $n \leq 8$, the half-range was adopted because of its more conservative estimations.

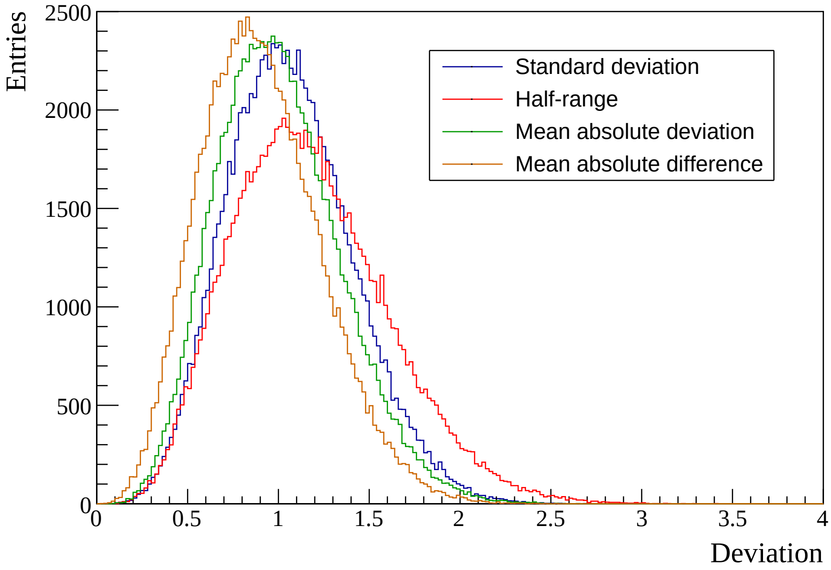

Figure 7.2 Distributions (in units of σ) of four estimators for σ in a standard normal distribution N when only 5 samples are taken from the distribution N. The sampling was repeated 100000 times.

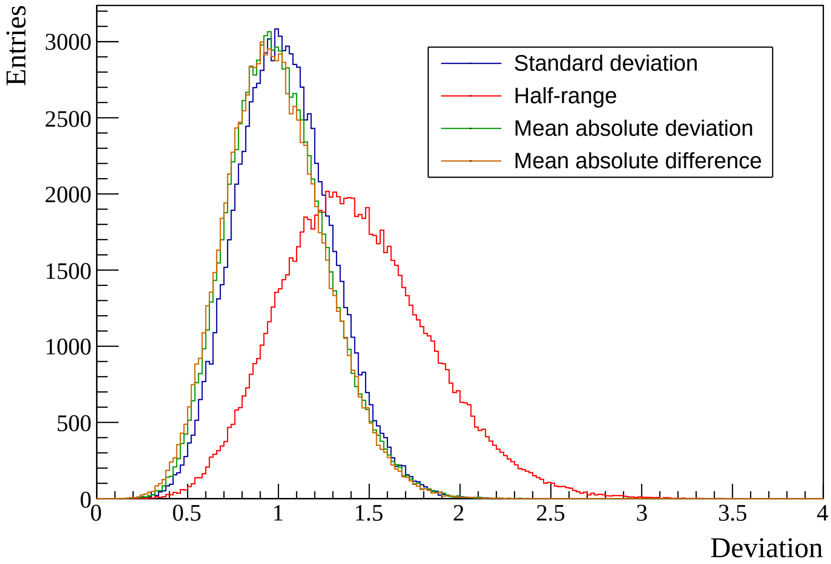

Figure 7.3 Distributions (in units of σ) of four estimators for σ in a standard normal distribution N when only 8 samples are taken from the distribution N. The sampling was repeated 100000 times.

7.2 Low-energy Criterion

The first selection criterion applied to AD events (after excluding PMT flashes) was $E_{\text{rec}} > 1.5$ MeV. In the end, this selection impacted only prompt events because of the more strict requirement applied to delayed events. The prompt-energy selection efficiency and its uncertainty were obtained with simulation in which the energy scale was scaled to that of the data (see Section 4.1). The efficiency was defined as the ratio of IBD reactions N that satisfied the prompt-energy criterion to the total number of IBD reactions occurring in the LS, GdLS, or acrylic volumes. For the nH-IBD analysis, this gives

$$\varepsilon_{E_p} = \frac{N(E_p > 1.5\ \text{MeV})}{N_{\text{IBD}}}. \tag{7-2}$$

The higher-energy requirement of $E_p < 12$ MeV contributed negligibly to the inefficiency and uncertainty, as indicated by Fig. 6.10. The efficiency in the LS volume was lower than that in the GdLS volume because a larger fraction of the positron's annihilation γ's escaped the scintillating volumes. The acrylic volume suffered the largest fraction of such events. The overall efficiency of all volumes was about 90%.

The AD-uncorrelated uncertainty of the prompt-energy selection efficiency was estimated by shifting the energy scale by 0.5% (see Section 4.1) and observing the change in efficiency. The change in efficiency was about 0.1% (relative).

7.2.1 Variation with Baseline

The L/E-dependence of neutrino oscillation [see Eq. (2-3)] implies that the neutrino energy spectrum changes with baseline L. Therefore, the positron energy spectrum changes, and as a result, the efficiency of the prompt-energy criterion (and therefore of all subsequent criteria) changes. The impact of this dependence was evaluated by applying oscillation to a predicted reactor antineutrino spectrum as a function of baseline. At each baseline (Table 3.1), the IBD selection efficiency was determined with simulation samples for each of the LS, GdLS, and acrylic volumes. The simulation incorporated energy deposited outside the scintillator volumes, and the estimated nonlinearity[12], nonuniformity (Section 4.4.2.1), and resolution (Section 4.4.3) of the AD energy-response. Oscillation parameter values were the same as those listed in Section 2.2. The resulting variation in IBD selection efficiency $vs.$ baseline is shown in Fig. 7.4, for the LS volume. The structure of the curve is owed to the range of the data in L/E: for the near halls (shorter L), more oscillation occurred for lower-energy $\overline{\nu}_e$'s, which decreased the fraction of IBD reactions with prompt energy below threshold and thus, increased the efficiency. For example, the average energy of a prompt event with no oscillation was 3.626 MeV while prompt events in EH1 (EH2) from $\overline{\nu}_e$'s produced at the two (four) nearby reactors was 3.630 (3.632) MeV with oscillation. These numbers represent the first 4 (following 8) points in Fig. 7.4. For the far hall (longer L), more oscillation occurred for median $\overline{\nu}_e$ energies and about equally for higher and lower energies, which resulted in a net decrease in efficiency.

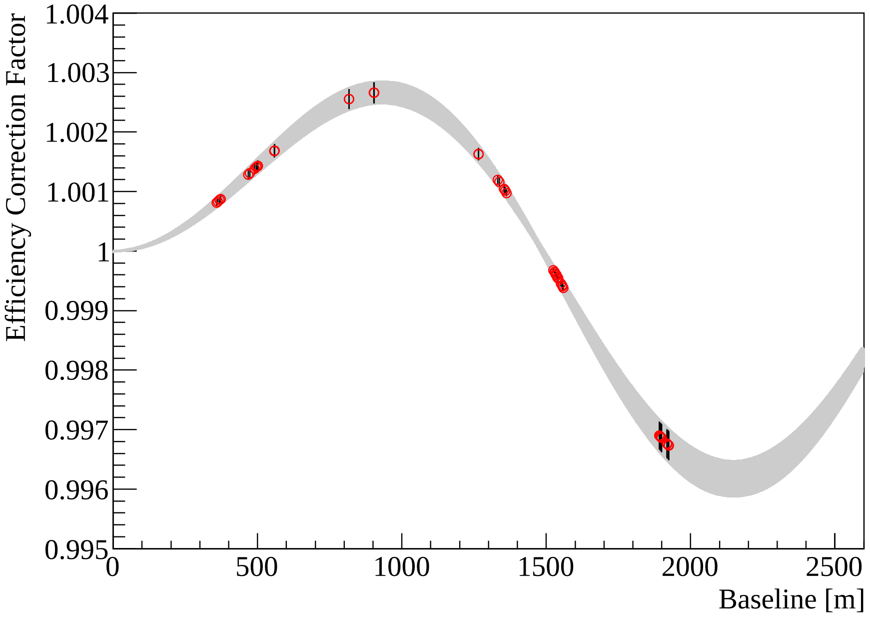

Figure 7.4 Relative variation of the IBD selection efficiency with baseline using the value of $\sin^2 2\theta_{13}$ determined by the nH-IBD analysis. This correction curve is for the LS volume. Red circles signify the 48 reactor-detector pairs. Their error bars (and the error band) are defined by the uncertainty of $\sin^2 2\theta_{13}$.

When fitting for $\sin^2 2\theta_{13}$ (see Section 8.2), the IBD selection efficiencies in the LS, GdLS, and acrylic volumes of each AD were multiplied by a correction factor for each reactor-detector baseline (6 reactors × 8 ADs = 48 baselines) and are tabulated in Appendix B.2. The fit was first done without correction factors. The resulting value of $\sin^2 2\theta_{13}$ was then used to produce a set of correction factors and then fit again. This iterative method was validated using Asimov data samples produced according to Eq. (3-1) with known values of $\sin^2 2\theta_{13}$. Several values for $\sin^2 2\theta_{13}$ were tested and all fits converged consistently with negligible bias; therefore, no additional uncertainty was assigned. Although several iterations were executed, the value of $\sin^2 2\theta_{13}$ converged within the precision reported after the first iteration. The first iterations of the fits (without correction factors) yielded results about 4% larger than both the true values for the Asimov data samples and the converged value for the measured data.

This variation of the IBD selection efficiency was an order of magnitude smaller for the *n*Gd-IBD analysis than for the *n*H-IBD analysis because of the lower prompt-energy criterion: $E_{\text{rec}} > 0.7$ MeV *vs.* $E_{\text{rec}} > 1.5$ MeV.

7.3 Coincidence-Time Criteria

The efficiency of the coincidence-time criteria was distinct for each detector volume v [see Eq. (7-1)] due to the different neutron-capture cross-sections and densities of the materials. The efficiency for the *n*H-IBD analysis was defined as

$$\varepsilon_T = \frac{N(1 < t_c < 400\ \mu s; E_p > \ 1.5\ \text{MeV})}{N(E_p > \ 1.5\ \text{MeV})}, \tag{7-3}$$

and was estimated with simulation. The efficiency for the LS volume was 85% and that for the GdLS volume was 99%, due to the shorter neutron-capture time of *n*Gd. These values were validated using data.

The neutron-capture time was studied in the GdLS and LS volumes by fitting the coincidence-time distribution with the following formulas:

$$\begin{aligned} N_{\text{LS}}(t) &= N_{0,\text{LS}} \cdot \tfrac{1}{\tau_{\text{LS}}} e^{-t/\tau_{\text{LS}}} + C_2, \\ N_{\text{Gd}}(t) &= N_{0,\text{Gd}} \cdot [(1+\alpha)\tfrac{1}{\tau_{\text{Gd}}} e^{-t/\tau_{\text{Gd}}} - \alpha \tfrac{1}{\tau_0} e^{-t/\tau_0}] + C_1, \end{aligned} \tag{7-4}$$

where α balances two terms: the first term corresponds to the capture of a thermal neutron [$O(0.025)$ eV] with time constant τ_{Gd}, and the second term represents the difference in capture cross-section between thermal and IBD neutron energies [$O(0.015)$ MeV], with the effective time constant τ_0. The capture-time spectrum in LS is determined almost entirely by *n*H which can be described by a single exponential. This is because the number of captures per volume per time, which is proportional to the product of neutron velocity and capture cross-section, is basically independent of energy below IBD neutron energies. For *n*Gd, this product is much smaller at IBD energies than at thermal energies (*e.g.*, see Ref.[87]), effectively yielding two different time constants with $\tau_0 < \tau_{\text{Gd}}$. The capture-time constant in LS is represented by τ_{LS}, and C_1 and C_2 are constants that account for accidentals.

The neutron-capture times for the LS and GdLS volumes were studied using *n*H- and *n*Gd-IBDs, respectively. The nominal IBD selection criteria (see Table 5.1) were slightly modified: the *n*H prompt-energy lower limit was increased to 3.5 MeV to minimize the accidental background, and the *n*H delayed-energy criterion was fixed to 1.8-2.8 MeV, while *n*Gd delayed events were selected between 6 and 10 MeV. When fitting the *n*H-IBD spectrum, the reconstructed positions of the prompt events were required to satisfy $r > 1.7$ m, to minimize the fraction of neutrons that originated from GdLS. Similarly, when fitting the *n*Gd-IBD spectrum, the constraints of $|z| < 1$ m and $r < 1$ m were applied to minimize the fraction of neutrons that originated from, or had any interactions, outside GdLS. Combining the data from all ADs, the fit results are shown in Figs. 7.5 and 7.6. The slopes of the spectra from data and simulation show good agreement. The fitted capture-time constants were $\tau_{LS} \approx 216\ \mu s$ and $\tau_{Gd} \approx 28.1\ \mu s$. For reference, the capture-time spectra of the near- and far-hall ADs, with the nominal *n*H-IBD selection criteria, are shown in Fig. 6.5, before and after subtracting the accidental background.

The AD-uncorrelated uncertainty of the *n*H-IBD 400-μs criterion in the combined LS plus GdLS volume was partially estimated using $\beta\alpha$ coincidences from the

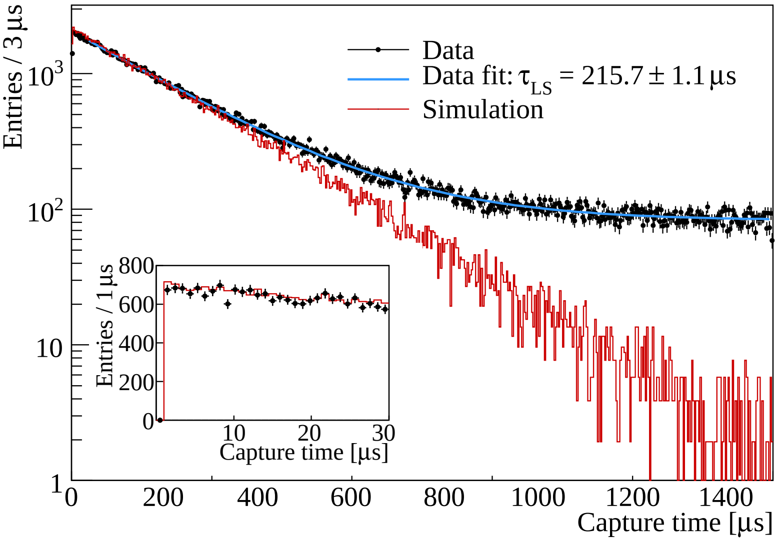

Figure 7.5 Time separation of double coincidences selected with *n*H-IBD criteria from simulation (red histogram) and from the LS volumes of all ADs (black points). The spectra are normalized to the number of coincidences between 30 and 300 μs. The fit to data (blue curve) and the fitted capture-time constant τ_{LS} are shown.

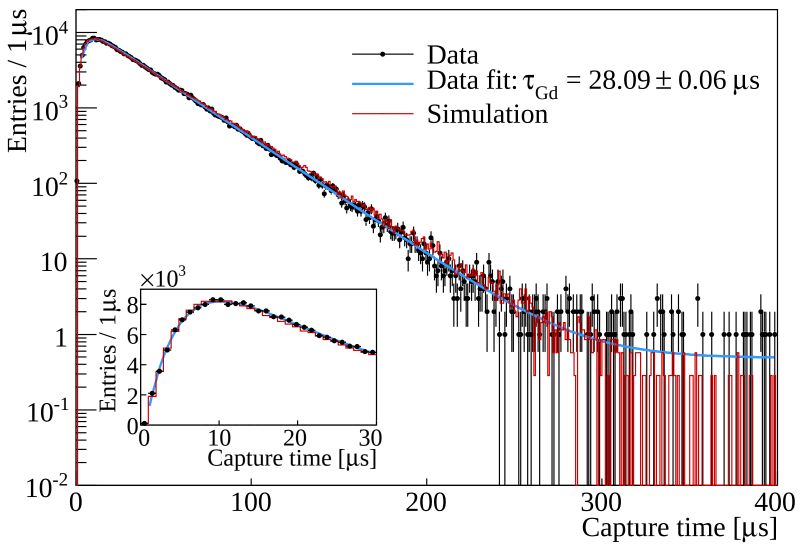

Figure 7.6 Time separation of double coincidences selected with *n*Gd-IBD criteria from simulation (red histogram) and from the GdLS volumes of all ADs (black points). The spectra are normalized to the number of coincidences between 6 and 150 μs. The fit to data (blue curve) and the fitted capture-time constant τ_{Gd} are shown.

^{214}Bi-^{214}Po-^{210}Pb decay chain. These coincidences offered greater statistics than *n*H events and were used to quantify the variation of the time measurements of the electronics. The lifetime of ^{214}Po is 237 μs, which is comparable to the mean *n*H capture time in LS. The efficiency of the selection was estimated relative to the number of DCs with a coincidence time window of [1, 1500] μs. Resulting efficiency curves and the relative differences of the ADs with respect to the average are shown in Fig. 7.7. The differences are within ±0.1% at the selection criterion of 400 μs.

The uncertainty of the 1-μs criterion was similarly determined to be 0.1% by comparing the relative number of events between 1 and 2 μs.

Since the uncertainty estimates used a source different from neutrons, additional uncertainties related to neutron-capture time were considered. These were identified from the following expression of the mean neutron-capture time:

$$\frac{1}{\tau} = \frac{v_n}{\lambda} = v_n \sum_i n_i \sigma_i(v_n), \tag{7-5}$$

where v_n is the neutron velocity, λ is the mean free-path of the neutron, σ_i is the neutron-nucleus cross-section of nucleus i, and n_i is the number-density. Isotopes other than Gd and H contributed fewer than 1% of captures (see Fig. 3.4) and were

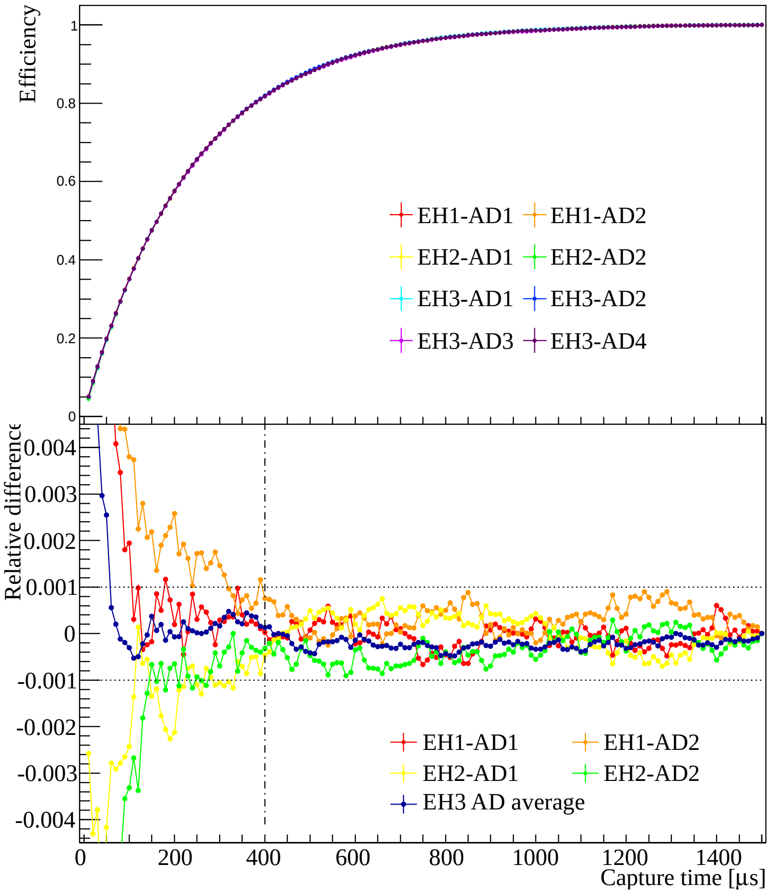

Figure 7.7 Efficiency (top panel) and relative difference to the average (bottom panel) *vs.* coincidence time for ^{214}Bi $\beta\alpha$ coincidences in each AD. In the bottom panel, the data of the far-hall ADs were combined to increase statistics. The differences are within ±0.1% at and beyond the criterion of 400 μs.

not considered. The measured density of the LS volume differed by less than 0.1% among the ADs. The fluctuation in density caused by temperature changes uncorrelated among experimental halls during the data-recording period was less than 0.045%. These effects introduced a less-than-0.11% uncertainty to τ in Eq. (7-5). Propagating this uncertainty through Eq. (7-4) yielded an approximately 0.02% AD-uncorrelated uncertainty originating from considerations of neutron-capture.

The uncertainties from the comparisons of ^{214}Bi $\beta\alpha$ coincidence-time spectra at 400 μs and 1 μs, and calculations of the neutron-capture time-related quantities were combined, giving a total AD-uncorrelated uncertainty of 0.14% for the efficiency of the coincidence-time criteria.

7.4 Delayed-Event-Energy Criteria

The efficiency of the *n*H delayed-energy criteria was estimated with simulation and defined as

$$\varepsilon_{E_d} = \frac{N(E_d \pm 3\sigma; 1 < t_c < 400\ \mu s; E_p > \ 1.5\ \mathrm{MeV})}{N(1 < t_c < 400\ \mu s; E_p > \ 1.5\ \mathrm{MeV})}. \tag{7-6}$$

This definition does not exclude IBDs whose neutron capture by nuclei different from hydrogen; namely, *n*Gd IBDs comprise approximately 0.7% of the IBDs after applying the delayed-energy criteria. The $\mu \pm 3\sigma$ selection was applied to each AD using the mean μ and standard deviation σ obtained from a fit of the Crystal Ball function[71] to the delayed-energy spectrum. The selection efficiency in the LS volume was about 65% mainly because of the outward escape of the *n*H γ's. The efficiency in the GdLS volume was about 15% mainly because of neutron-capture by gadolinium.

The AD-uncorrelated uncertainty of the delayed-energy selection efficiency was estimated by comparing measured efficiencies of the ADs. Efficiency ε_{E_d} defined in Eq. (7-6) could not be directly measured due to the enormous background rate at low energies that contaminated the sample of the denominator. Therefore, the variation of ε_{E_d} was approximated by the variation of a ratio in which the numerator used the nominal selection of $\mu \pm 3\sigma$ (approximately [1.90, 2.74] MeV), however the denominator used an energy range of [1.50, 2.80] MeV. Both of these ranges are visible in Fig. 7.8, for each AD. The upper value of the latter range (2.80 MeV) is slightly larger than the nominal upper value to include most of the *n*H IBDs with $E_d > 2.74$ MeV (only 0.1% of *n*H IBDs). The lower value is limited by the low-energy criterion (Section 5.2), but includes much of the tail of the spectrum (12% more *n*H IBDs). The latter range includes both peak and tail portions of the spectrum and is therefore sensitive to all factors that may impact the shape of the spectrum. For *n*Gd IBDs, the two ranges are the nominal range [6.0, 12.0] MeV and the extended range [3.6, 12.0] MeV. These numerators and denominators were calculated after applying the distance criterion (*n*H only) and subtracting the accidental backgrounds (errors from the subtractions were propagated).

Using each AD i, a linear relation was fit between the number of events in the nominal range (range A) $N_{A,i}$ and the number of events in the extended range (range B) $N_{B,i}$:

$$\overline{N}_A(N_{B,i}) = a + bN_{B,i}. \tag{7-7}$$

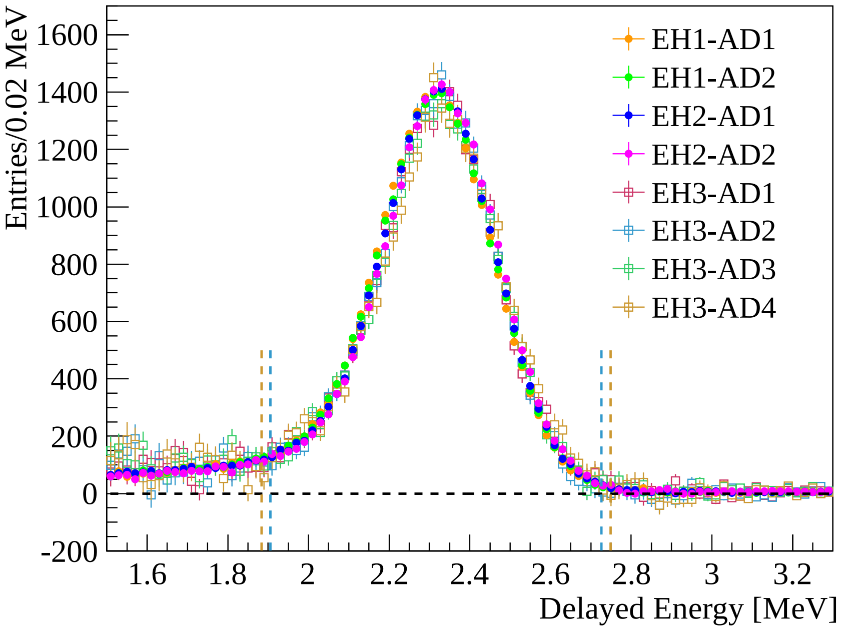

Figure 7.8 Delayed-energy spectra of nH IBDs from all ADs. The entries in each histogram are normalized to the average number of IBDs from the far-hall ADs. The fitted means are aligned to the average fitted mean of the far-hall ADs. The two pairs of vertical lines correspond to the most narrow and most wide 3σ selections among the eight ADs.

The fitted line embodies the average behavior of all ADs, including differences in their spectra and residual backgrounds. We introduce the notation $\varepsilon_i \equiv N_{A,i}/N_{\text{Total,i}}$, which is meant to be identical to Eq. (7-6) except that accidentals have been subtracted and the distance criterion has been applied. The relative variation of ε for each AD was estimated using the fitted line as follows:

$$\frac{\delta\varepsilon_i}{\varepsilon_i} = \frac{\delta N_{A,i}}{N_{A,i}} = \frac{N_{A,i} - \overline{N}_A}{N_{A,i}} = 1 - \frac{a + bN_{B,i}}{N_{A,i}}. \tag{7-8}$$

One potential impact of Eq. (7-8) is that N_{Total} is assumed to be invariant. From studies with simulation, N_A and N_{Total} were found to be highly correlated under various scenarios that could modify the shape of the spectrum, making this assumption conservative. The simulated scenarios included differences in OAV dimensions[59] and the residual nonuniformity of E_{rec} (Section 4.2). However, N_B is used as a proxy for N_{Total}, and it is not assumed to be invariant. Since N_B is highly correlated with N_{Total}, the neglected impact of the aforementioned scenarios due to N_{Total} cancels with the corresponding impact due to N_B. Using N_B as a proxy also assumes that variations in the spectrum below range B are not systematically different from variations within range B. Using simulation, differences in OAV dimensions, residual nonuniformity, or the mean free path of the γ's were found to have a greater influence on the spectrum at the low-energy end, but to contribute negligibly to $\delta\varepsilon_i/\varepsilon_i$. Moreover, a comparison of the high-statistics spectra of the near-hall ADs did not reveal any systematic differences among spectra above 1.5 MeV, suggesting that there may not be any such difference below 1.5 MeV.

The data from the far-hall ADs were excluded from the determination due to their large statistical uncertainties, though the sum of their data was conservatively used in the linear fit. The half-range of $\delta\varepsilon_i/\varepsilon_i$ for the four near-hall ADs was 0.33%. This uncertainty includes AD-to-AD variations in the 3σ selection (for *n*H IBDs), energy scale, and factors that may influence the shape of the spectrum; however, it does not include variations in the fraction of neutrons that capture on the isotope of interest (H or Gd) because such variations have an equivalent impact on N_B and N_A. For the *n*H-IBD analysis, these fractions are 53% for H, 46% for Gd, and 0.5% for C.

The fraction of neutrons captured by isotope x is expressed similarly to the mean capture time in Eq. (7-5):

$$f_x = \frac{n_x \sigma_x(v_n)}{\sum_i n_i \sigma_i(v_n)}. \tag{7-9}$$

Carrying out error propagation on both Eq. (7-5) and Eq. (7-9), and then combining the results, the variation of f_x among the ADs can be expressed in terms of the variation of τ and one of the n_i. Thus, the variation in the measured capture time in the GdLS can constrain the variation of n_{Gd}. The variation in n_{H} is argued to be negligible because of the mixing of all batches of scintillator after production[61] and the AD filling procedures[88]. Consequently, the AD-to-AD variation in f_{H} was estimated to be less than 0.01% and 0.16% in the LS and GdLS volumes, respectively. After accounting for the efficiency of the *n*H-IBD selections in these two volumes, the variation was approximately 0.03% for the full volume.

This paragraph describes a subtle point about the *n*Gd capture fraction f_{Gd}. As described in Section 7.3, the probability of a neutron's capture by Gd depends on energy, leading to a capture time spectrum that can be described with two terms [see the second expression of Eq. (7-4)]. Since the time spectrum can be fit with this two-component formula, a two-component cross-section is expected to be a valid approximation. Similarly, two effective cross-sections implies two capture fractions for *n*Gd. From the fit parameters of Eq. (7-4), about 85% of the *n*Gd-IBD neutrons capture at thermal energies. The capture fraction uncertainty estimate described in the previous paragraph was performed with the thermal capture time. This result is appropriate as long as the variation of the capture times for thermal and IBD neutrons are similar.

Finally, the total AD-uncorrelated uncertainty of the delayed-energy selection efficiency was estimated to be 0.33% by combining the variations estimated from the efficiency comparison and the *n*H capture-fraction. The corresponding uncertainty for the *n*Gd-IBD analysis was 0.15%, owing to 0.11% and 0.10% uncertainties, respectively.

To estimate the correlation of the delayed-energy selection efficiency between the *n*H- and *n*Gd-IBD analyses, the uncertainty was separated into three categories: 3σ variation, energy scale variation, and "other" factors that may not have been completely evaluated due to the finite lower limit of range B, such as differences in OAV dimensions or the residual nonuniformity of E_{rec}. The first two components were estimated with simulation by: (1) applying the widest and narrowest 3σ ranges (see Fig. 7.8) and (2) shifting the energy scale (see Section 7.2), respectively. The first component was dominant for the *n*H-IBD analysis and did not exist for the *n*Gd-IBD analysis; thus, it is uncorrelated. The correlation of the energy scales between the *n*H- and *n*Gd-IBD analyses was determined to be 0.8 by fitting a line to the measured *n*H-IBD *vs.* *n*Gd-IBD delayed-energy peaks. The last uncertainty category of "others" was conservatively assumed to be fully correlated. In the GdLS volume, the hydrogen capture fraction of the *n*H analysis and the gadolinium capture fraction of the *n*Gd analysis were anticorrelated: if the fraction of captures on Gd decreases, then naturally the fraction on H increases. In the LS volume, the same anticorrelated relationship exists through neutrons that are produced in LS or GdLS but capture in the other volume. Combining the four correlation constants and the corresponding uncertainties from both the *n*H and *n*Gd analyses using Eq. (8-11) yielded an overall correlation coefficient of 0.07 for the efficiency of the delayed-energy selection.

7.5 Coincidence-Distance Criterion

The efficiency of the coincidence-distance criterion of the *n*H analysis was measured with the data of all eight ADs and was ideally defined as

$$\varepsilon_D = \frac{N(d_c < 50\text{ cm}; E_d \pm 3\sigma; 1 < t_c < 400\ \mu s; E_p > 1.5\text{ MeV})}{N(E_d \pm 3\sigma; 1 < t_c < 400\ \mu s; E_p > 1.5\text{ MeV})}. \tag{7-10}$$

In actuality, the denominator could not be evaluated directly due to the large accidental background. Instead, the DCs of the denominator were also required to satisfy $d_c <$ 200 cm and had accidental backgrounds subtracted as shown in Fig. 6.4. Resulting efficiency curves and the relative differences of the ADs with respect to the average are shown in Fig. 7.9. The efficiency at $d_c <$ 50 cm was about 75%. The total number of IBDs in the far-hall ADs was only about half that of a single near-hall AD; therefore, the data of the four far-hall ADs were combined to calculate the relative difference. The five differences were within ±0.4% at the 50-cm selection criterion. Accordingly, the AD-uncorrelated uncertainty of the efficiency of the coincidence-distance criterion was chosen to be 0.4%.

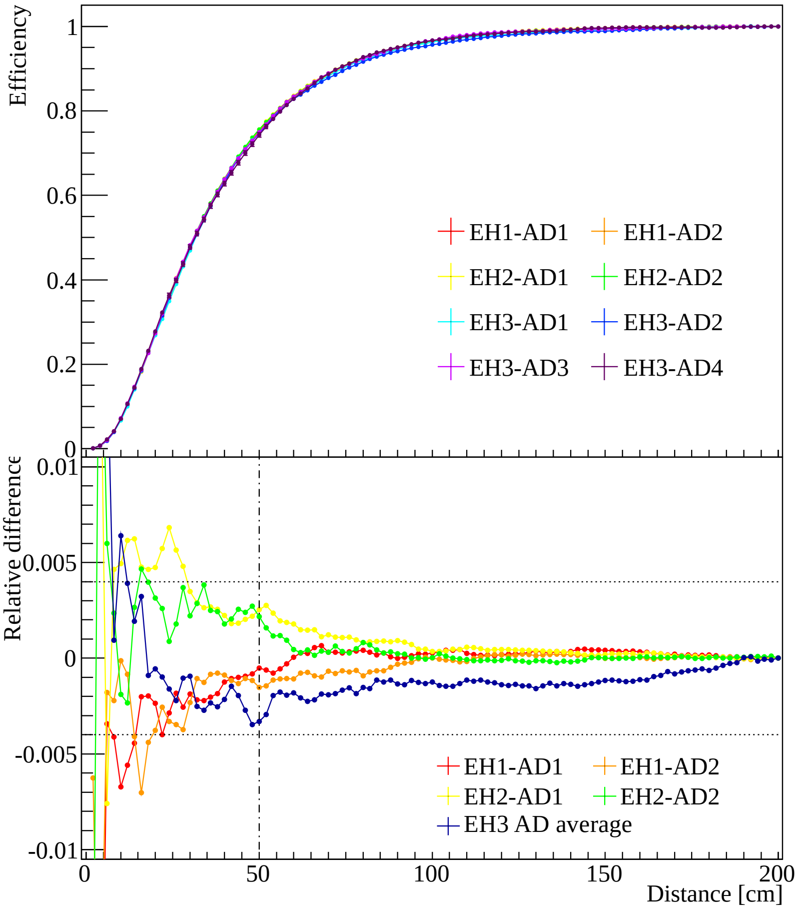

Figure 7.9 Efficiency (top panel) and relative difference to the average (bottom panel) *vs.* coincidence-distance for correlated double coincidences N_{Cor} in each AD. In the bottom panel, the data of the far-hall ADs were combined to increase statistics. The differences are within ±0.4% at and beyond the criterion of 50 cm.

7.6 IBDs in Acrylic and Mineral Oil

The primary target materials were liquid scintillator, however, the IAV, OAV, and acrylic-encased reflectors directly contact or are in close proximity with the scintillators such that an IBD positron coming from these elements could enter the scintillators and deposit enough energy to trigger an AD. Such IBDs contributed an estimated 1.0% for both the nH and nGd analyses after IBD selection.

IBD positrons created in the MO seldom reached scintillator and usually produced an insufficient amount of light to trigger an AD. However, a few percent of the IBD positrons annihilated in flight (see Section 3.1), producing a higher-energy γ that was sometimes aimed toward the scintillator and had enough energy to satisfy the low-energy criterion. The associated IBD neutrons sometimes propagated toward the LS and captured on H. Using simulation, about 0.06% of the IBDs in the MO should have survived the selection criteria. This effect of “spilling in” from the MO had a negligible impact on the determination of $\sin^2 2\theta_{13}$ and so, was not included in the nH-IBD analysis.

It is noted that the impact of neutrons, γ’s, and β’s (and their secondaries) that spill out into the MO, or spill in/out between the LS and GdLS, is naturally included in the definitions of the prompt- and delayed-energy selection efficiencies and the estimations of their uncertainties.

7.7 Target Proton Number

The numbers of target protons N_p in Eq. (7-1) were determined for each AD from the measured target masses M and hydrogen mass-fractions w_{H} of the LS, GdLS, and acrylic volumes v:

$$N_{p,v} = M_v \, w_{\mathrm{H},v} \, N_{\mathrm{A}} \, / \, m_{\mathrm{H}} \, , \tag{7-11}$$

where N_{A} is Avogadro’s number (6.022141E23 mol^{-1}) and m_{H} is the molar mass of hydrogen (1.007975 g mol^{-1}).

The mass-fractions of hydrogen were determined to be about 12.0% for both LS and GdLS by combustion analysis (with uncertainties at the level of 0.1%)[59]. The AD-uncorrelated uncertainties of these w_{H} were taken to be negligible as described for n_{H} in Section 7.4. For acrylic $w_{\mathrm{H}} = 8.05\%$ and was estimated analytically from the chemical formula $C_5H_8O_2$.

The masses of LS and GdLS were measured when filling each AD, using a Coriolis flow meter and a load cell, respectively[88]. The masses of the various acrylic components were measured earlier with an industrial scale[60]. The masses of each volume v are given in Table 7.1 for each AD. The final uncertainties of the target proton numbers contained only uncertainties of the target masses.

The average number of target protons in the LS, GdLS, and acrylic volumes are 1.54×10^{30}, 1.43×10^{30}, and 0.18×10^{30}, respectively. Values for each AD are listed in Table 7.1. AD-uncorrelated uncertainties are listed in Table 7.2.

Table 7.1 Masses [kg] and numbers of target protons of the GdLS, LS, and acrylic volumes of each AD.

Detector	M_{LS}	$N_{p,\text{LS}}$ [$\times 10^{30}$]	M_{GdLS}	$N_{p,\text{GdLS}}$ [$\times 10^{30}$]	M_{acrylic}	$N_{p,\text{acrylic}}$ [$\times 10^{30}$]
EH1-AD1	21574	1.547	19941	1.430	3697	0.178
EH1-AD2	21520	1.543	19967	1.431	3731	0.179
EH2-AD1	21587	1.548	19891	1.426	3664	0.176
EH2-AD2	21450	1.538	19944	1.430	3749	0.180
EH3-AD1	21566	1.546	19917	1.428	3744	0.180
EH3-AD2	21409	1.535	19989	1.433	3864	0.186
EH3-AD3	21653	1.553	19892	1.426	3844	0.185
EH3-AD4	21475	1.540	19931	1.429	3794	0.183

7.8 Summary

The efficiencies of the prompt- and delayed-energy, and coincidence-time selection criteria were determined using simulation, while the numbers of target protons, and the muon-veto, multiplicity, and coincidence-distance selection efficiencies were determined using data. The AD-uncorrelated uncertainties of these quantities were estimated by comparing data from the eight ADs.

The muon-veto and multiplicity selection efficiencies (ε_μ and ε_m) associated with each AD are listed in Tables 5.2 and 5.3. These quantities had negligible AD-uncorrelated uncertainties, as may be inferred from their differences. The product of the prompt- and delayed-energy, and time selection efficiencies was about 50%, 14%, and 5% for the LS, GdLS, and acrylic volumes, respectively. This product was about 77%

for the GdLS volume and the *n*Gd-IBD analysis. The efficiency of the *n*H-IBD coincidence-distance criterion was determined from data as an average of all volumes: 75%. The AD-uncorrelated uncertainties of these efficiencies are listed in Table 7.2. Compared with the previous *n*H-IBD analysis[15], the uncertainty of the delayed-energy selection efficiency was reduced from 0.5% to 0.35% because of a new estimation. This improvement reduced the total uncertainty of N_ε [Eq. (7-1)] by 15%.

Table 7.2 The relative AD-uncorrelated uncertainties of each detector-related quantity for the *n*H- and *n*Gd-IBD analyses. The uncertainties of the N_p are weighted when determining the combined uncertainties of the N_ε in the bottom row. The last column gives the estimated correlation coefficients between the *n*H and *n*Gd analyses.

	*n*Gd [%]	*n*H [%]	Correlation
Target protons ($N_{p,\mathrm{GdLS}}$)	0.03	0.03	1
Target protons ($N_{p,\mathrm{LS}}$)	NA	0.13	0
Prompt energy (ε_{E_p})	0.01	0.10	1
Coincidence time (ε_T)	0.01	0.14	1
Delayed energy (ε_{E_d})	0.16	0.33	0.07
Coincidence distance (ε_D)	NA	0.40	0
Combined (N_ε)	0.16	0.56	0.07

Table 7.2 also lists the correlation coefficient of each detector-related quantity in the *n*H- and *n*Gd-IBD analyses. The number of target protons were uncorrelated in the LS while fully correlated in the GdLS due to their independent and identical methods of mass determination, respectively. The efficiencies of the prompt-energy criteria were correlated through a common dependence on energy scale, and was conservatively considered as fully correlated. The efficiencies of the coincidence-time criteria were also treated as fully correlated. The delayed-energy criteria were largely independent because the primary component of uncertainty for the *n*H-IBD analysis was the variation of the 3σ selection among the ADs, which did not exist in the *n*Gd analysis. The coincidence-distance criterion was uncorrelated because no such selection existed in the *n*Gd-IBD analysis. The overall correlation between the IBD selection efficiencies of the *n*H and *n*Gd analyses was about 0.07, as described in Section 8.3.3.

The ratio of the N_ε-corrected rates of IBDs for the *n*H- and *n*Gd-IBD analyses is listed for each AD in the bottom row of Tables 5.2 and 5.3. Their errors consist of the statistical, AD-uncorrelated systematic, and background uncertainties of both analyses. The consistency of the eight values with each other indicates the consistency of the selected number of IBDs, per-AD target proton and efficiency corrections, and background estimates between the two analyses. The consistency of the eight values with 1 indicates the accuracy of these values in both analyses. It is noted, however, that to properly compare the consistency of the efficiencies, the errors should also include AD-correlated uncertainties. For the *n*Gd analysis, this uncertainty has been reported to be 2.1%[53]. For the *n*H analysis, this uncertainty is similar.

Chapter 8 Results

The measured and predicted rates of IBDs for each experimental hall are shown *vs.* time in Fig. 8.1. The measured rates are the R_{IBD} in Tables 5.2 and 5.3, for which backgrounds were subtracted and the muon veto and multiple coincidence efficiencies ($\varepsilon_\mu \varepsilon_m$) were corrected. The predicted rates are from Eq. (3-1) [which is comprised of Eqs. (3-2) and (7-1)] and are adjusted with the normalization factor ϵ that resulted from the minimization of Eq. (8-6). As seen in the figure, the six reactors operated continually at nominal power output with occasional 1 to 2 months of downtime for refueling. The two reactors nearest EH1 were refueled every 16 months and the four reactors nearest EH2 were refueled every 8 to 12 months.

8.1 Antineutrino Disappearance

Prior to fitting for $\sin^2 2\theta_{13}$ in the next section, this section quantifies the disappearance of $\overline{\nu}_e$ without relying on a model of neutrino oscillation and with minimal impact from models of reactor antineutrino spectra. This was done by directly comparing the measured number of IBDs at the far hall with the number expected based on the measurements at the near halls. The latter was expressed as

$$\overline{N}_{\mathrm{EH3}} \equiv \alpha N_{\mathrm{EH1}} + \beta N_{\mathrm{EH2}}, \tag{8-1}$$

where N_{EH1} and N_{EH2} are the measured numbers of IBDs in EH1 and EH2, which are background-subtracted and corrected for the muon-veto and multiple coincidence selection efficiencies ($\varepsilon_\mu \varepsilon_m$).

Expressions for α and β in Eq. (8-1) were determined by replacing the number of measured IBDs with the number of predicted IBDs assuming no oscillation. This predicted number was calculated for experimental hall i using Eq. (3-1) without oscillation:

$$\overline{N}_i = \sum_{r=1}^{6} \overline{N}_{ir} \equiv \sum_{r=1}^{6} \sum_{d_i} \frac{N_{\varepsilon,d_i}}{4\pi L_{d_i r}^2} \iint_{\{t_{d_i}\}} \sigma_{\mathrm{IBD}} \frac{d^2 N_r}{dE dt} dE dt, \tag{8-2}$$

where d_i is the dth AD in experimental hall i and N_ε does not include ε_m and ε_μ. The

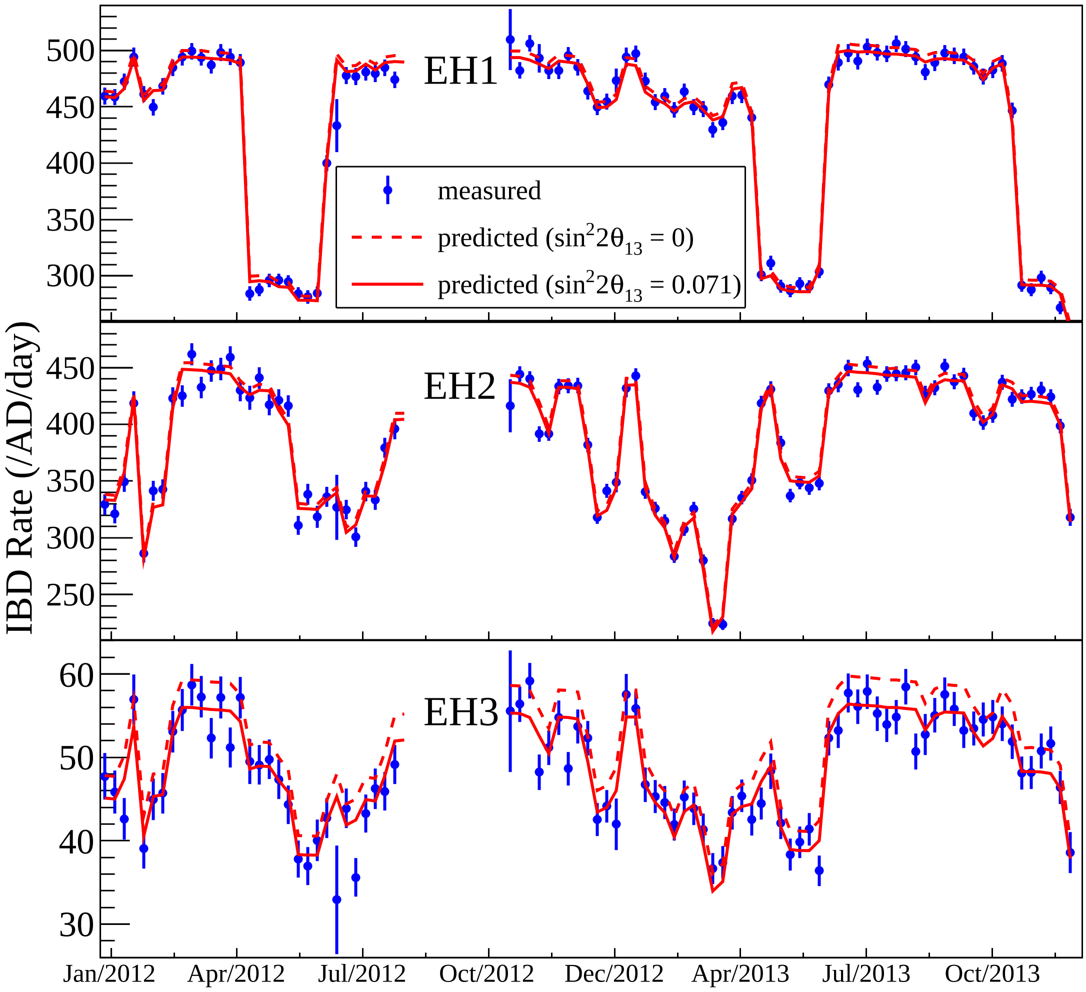

Figure 8.1 Measured (blue points) and predicted (red curves) IBD rate *vs.* time for each experimental hall. Each point spans one week and has a purely statistical error bar. The dashed red curves are the expected IBD rates assuming no oscillation. The solid red curves are the expected IBD rates assuming the best-fit value of $\sin^2 2\theta_{13}$. The final two of the eight ADs were installed during the ≈12-week gap.

modified Eq. (8-1) directly yields

$$\beta = (\overline{N}_3 - \alpha\overline{N}_1)/\overline{N}_2. \tag{8-3}$$

The other weight, α, was obtained by minimizing the reactor-uncorrelated uncertainty:

1. Begin with difference between the two predictions for EH3: $\Delta\overline{N} = \overline{N}_3 - \alpha\overline{N}_1 - \beta\overline{N}_2$.
2. Obtain the variance of $\Delta\overline{N}$ (σ_Δ^2) via error propagation with respect to the reactor-uncorrelated relative uncertainty (which was taken to be identical for all reactors).

3. Find the minimum of σ_{Δ}^2 with respect to α.

These steps yield

$$\alpha = \frac{\sum_r (\overline{N}_{3r} - \frac{\overline{N}_3}{\overline{N}_2}\overline{N}_{2r})(\overline{N}_{1r} - \frac{\overline{N}_1}{\overline{N}_2}\overline{N}_{2r})}{\sum_r (\overline{N}_{1r} - \frac{\overline{N}_1}{\overline{N}_2}\overline{N}_{2r})^2}, \tag{8-4}$$

which minimizes the impact of the reactor-uncorrelated uncertainty in Eq. (8-1).

For the 621-days of this analysis, $\alpha = 0.054$ and $\beta = 0.216$ for the nH data sample. These values are primarily determined by the baselines L_{dr}, with a smaller influence from the reactor neutrino emission rates $d^2N_r(E,t)/dEdt$. As a result, β, which is affiliated with EH2, is four times greater than α primarily due to the shorter baselines between EH3 and the four reactors near EH2. The reactor-uncorrelated uncertainty is suppressed by a factor of approximately 20, which was determined by evaluating the expression for σ_{Δ}^2.

Using Eq. (8-1), the ratio of the observed to the expected number of nH IBDs at the far hall was

$$R \equiv \frac{N_{\mathrm{EH3}}}{\overline{N}_{\mathrm{EH3}}} = 0.950 \pm 0.005. \tag{8-5}$$

Figure 8.2 shows the measured prompt E_{rec} spectrum from nH IBDs in the far hall and that predicted with the near-hall measurements using Eq. (8-1). The ratio R is shown for each energy bin in the bottom panel, which expresses the effect of $\overline{\nu}_e$ disappearance as a function of energy. The curve labeled as "Best fit" is the ratio of the far-hall and normalized near-hall predictions using Eq. (3-1) and the result for $\sin^2 2\theta_{13}$ presented in Section 8.2.

8.2 Fit for $\sin^2 2\theta_{13}$

The fit of $\sin^2 2\theta_{13}$ was performed with a χ^2 formula that used pull terms for the background and the AD- and reactor-uncorrelated uncertainties:

$$\begin{aligned} \chi^2 = &\sum_{d=1}^{8} \frac{[N_{\mathrm{DC},d} - \overline{N}_{\mathrm{IBD},d}(1 + \epsilon + \sum_{r=1}^{6} \omega_r^d \alpha_r + \epsilon_d) - (1 + \eta_d)B_d]^2}{(\sigma_{\mathrm{DC},d})^2} \\ &+ \sum_{r=1}^{6} \frac{\alpha_r^2}{\sigma_R^2} + \sum_{d=1}^{8} \left(\frac{\epsilon_d^2}{\sigma_D^2} + \frac{\eta_d^2}{(\sigma_{B,d})^2} \right). \end{aligned} \tag{8-6}$$

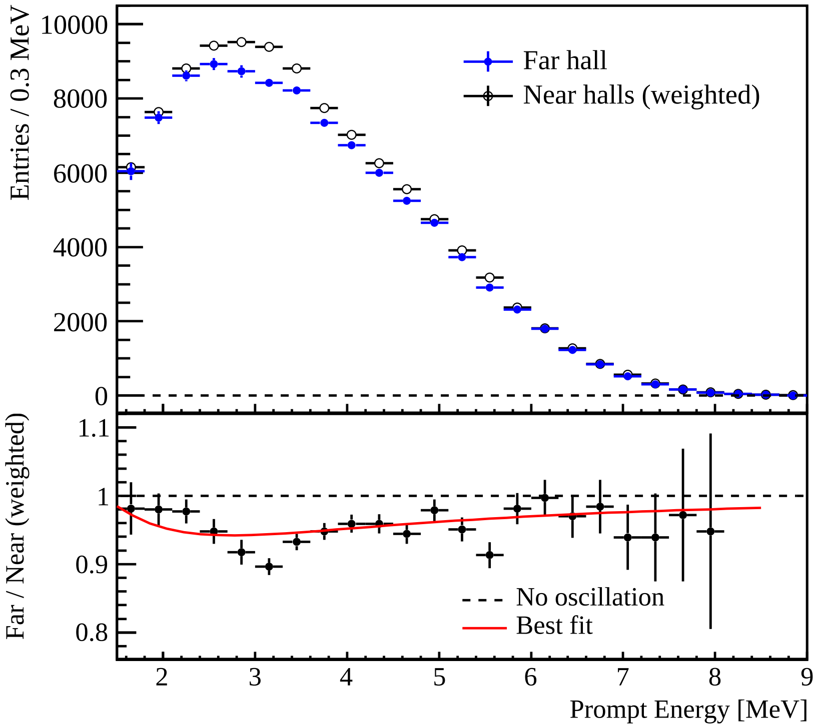

Figure 8.2 Top: Reconstructed prompt-energy spectrum from the far hall (solid blue points) and the expectation based on the measurements from the two near halls (empty black points). Backgrounds were subtracted and error bars are purely statistical. Bottom: Ratio of Far/Near and the curve representing the best-fit value of $\sin^2 2\theta_{13} = 0.071 \pm 0.011$.

$N_{\mathrm{DC},d}$ is the number of double coincidences in the dth AD, which is listed in Tables 5.2 and 5.3, B_d is the sum of all backgrounds, which can be found in Tables 5.2 and 5.3, $\sigma_{\mathrm{DC},d}$ is the statistical uncertainty of N_{DC}, and $\overline{N}_{\mathrm{IBD},d}$ is the predicted number of IBDs from Eq. (3-1), which contains the oscillation parameter $\sin^2 2\theta_{13}$. The ω_r^d (see Table 8.1) are the fractions of IBDs in the dth AD due to the rth reactor, and were calculated using Eq. (3-1) assuming no oscillation (including oscillation decreased the best-fit value of $\sin^2 2\theta_{13}$ by less than 0.03%). σ_R is the reactor-uncorrelated uncertainty discussed in Section 2.3, σ_D is the AD-uncorrelated uncertainty of IBD selection efficiency given in Table 7.2, and $\sigma_{B,d}$ is the total uncertainty from of all background estimates, which are given in Tables 5.2 and 5.3. There are 22 pull parameters corresponding to these uncertainties: α_r, ϵ_d, and η_d. ϵ is an unconstrained normalization factor that accounts for any biases in the backgrounds that were common to all halls or detectors, and any biases in the predicted number of IBDs that were common to all detectors, such as in IBD selection efficiencies, reactor-related models or quantities, and the IBD cross-section model.

Table 8.1 Predicted fractions of IBDs in the dth AD due to each of the six nuclear reactors.

Detector	ω_1^d	ω_2^d	ω_3^d	ω_4^d	ω_5^d	ω_6^d
EH1-AD1	0.384	0.408	0.064	0.083	0.031	0.031
EH1-AD2	0.387	0.408	0.063	0.081	0.030	0.030
EH2-AD1	0.032	0.034	0.262	0.254	0.198	0.220
EH2-AD2	0.033	0.032	0.253	0.252	0.193	0.238
EH3-AD1	0.115	0.131	0.185	0.197	0.194	0.179
EH3-AD2	0.115	0.132	0.185	0.197	0.194	0.178
EH3-AD3	0.115	0.131	0.185	0.196	0.194	0.179
EH3-AD4	0.122	0.123	0.180	0.196	0.186	0.192

Fitting $\sin^2 2\theta_{13}$ iteratively with the efficiency correction factors described in Section 7.2.1, the best-fit value under both the normal and inverted neutrino-mass hierarchies was

$$\sin^2 2\theta_{13} = 0.071 \pm 0.011, \tag{8-7}$$

which had a χ^2_{min} per degree of freedom of 6.3/6. The no-oscillation hypothesis is excluded at 6.5 standard deviations.

The ratio of the measured rate to the predicted rate assuming no oscillation, is shown for each detector in Fig. 8.3. The deficit of 5.0% in EH3 relative to the near halls given [see Eq. (8-5)] is evident. The nGd-IBD analysis had a deficit of about 5.2% and a best-fit value of[12]

$$\sin^2 2\theta_{13} = 0.084 \pm 0.005. \tag{8-8}$$

The red curve is the $\overline{\nu}_e$ survival probability P_{ee} of Eq. (2-3) with a value of $\sin^2 2\theta_{13} =$ 0.082, which is from the combination of the nH- and nGd-IBD results, and is described in Section 8.3.4.

The total uncertainty of $\sin^2 2\theta_{13}$ (σ_{total}) is separated into the contributions from several quantities in Table 8.2, which are presented as fractions of σ^2_{total}. The absolute contribution of a quantity was estimated by subtracting the square of the fit error when fixing the nuisance parameter of said quantity to its best-fit value, from the total σ^2_{total}. Due to correlations between some systematics, the sum of the fractions is not equal to 1.

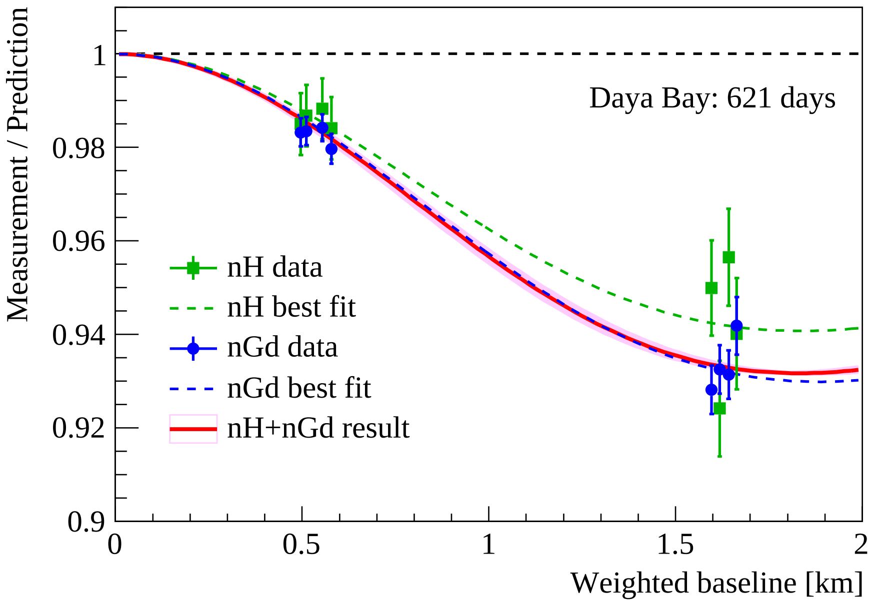

Figure 8.3 Ratio of measured IBD rate to predicted IBD rate assuming no oscillation *vs.* flux-weighted baseline, for each detector. For the *n*H (*n*Gd) analysis, each detector is represented by a green square (blue circle). Error bars include all uncertainties except reactor-related. The dashed green (blue) curve is the neutrino oscillation probability using the *n*H (*n*Gd) result for $\sin^2 2\theta_{13}$ and the global fit value for Δm^2_{32} (the *n*Gd result for Δm^2_{ee}). The solid red curve is the oscillation probability using the *n*H-*n*Gd combined result and Δm^2_{32}, and its magenta error band is the uncertainty of Δm^2_{32}. For visual clarity, the baselines of EH1-AD2 and EH2-AD2 are offset by +20 m, and those of EH3-AD1, 2, 3, and 4 are offset by -30, -10, +10, and +30 m, respectively.

The statistical uncertainty is the largest contributor in both *n*Gd and *n*H analyses. For the *n*Gd analysis, the second- and third-largest uncertainties are those of the delayed-energy criterion and the relative energy scale uncertainty (see Table 7.2 for the components of the detector contribution). For the *n*H analysis, the corresponding uncertainties are those of the coincidence-distance criterion and the delayed-energy criterion (again, see Table 7.2). As discussed regarding the relative expression of Eq. (8-5), the reactor-uncorrelated uncertainty is reduced by a factor of 20.

8.3 *n*Gd-*n*H Combination

This section presents two methods to handle correlations between the systematic uncertainties of two measurements within a χ^2 formalism. The correlation between each systematic uncertainty of the *n*Gd and *n*H analyses is discussed and assigned a value. Using these values, the two analyses are combined with one of the two

Table 8.2 Fractional contributions of individual uncertainties to the total uncertainty of $\sin^2 2\theta_{13}$ for the *n*Gd- and *n*H-IBD analyses. See the text for details. Detector uncertainties are tabulated in Table 7.2. The last column lists the correlation coefficients between the two analyses.

	*n*Gd [%]	*n*H [%]	Correlation
Statistical	67.0	51.8	0
Detector	19.2	39.2	0.07
Reactor	4.8	4.2	1
^{9}Li/^{8}He	9.5	4.4	0
Accidental	0.0	0.4	0
Am-C	0.7	0.1	0.7
Fast neutron	1.2	0.3	0
^{13}C(α,n)^{16}O	0.1	0.0	1
Combined	102.6	100.4	0.02

methods: the analytical solution of a χ^2. AD-uncorrelated uncertainties are found to have minimal correlation among the analyses, showing that the *n*Gd and *n*H analyses provide independent measurements of θ_{13}. Furthermore, the combination provides a noticeable improvement in the precision of θ_{13} obtained by the Daya Bay experiment.

8.3.1 χ^2 Formalism

The pull-term χ^2 used to determine $\sin^2 2\theta_{13}$ is given by Eq. (8-6). Its basic form is expressed as the difference between measurement M and prediction P, which is adjusted by measurement efficiency ε:

$$\chi^2 = \left(\frac{M - P\varepsilon(1+\eta_\varepsilon)}{\sigma}\right)^2 + \left(\frac{\eta_\varepsilon}{\sigma_\varepsilon}\right)^2, \tag{8-9}$$

where η_ε and σ_ε are the nuisance parameters and relative uncertainty of ε, and σ is the statistical uncertainty of M. When combining two measurements, denoted as M_{Gd} and M_H, the χ^2 derived from a 2-by-2 covariance matrix is

$$\chi^2 = \frac{1}{1-\rho^2}\left[\left(\frac{M_{Gd} - P_{Gd}\varepsilon_{Gd}}{\sigma_{Gd}}\right)^2 + \left(\frac{M_H - P_H\varepsilon_H)}{\sigma_H}\right)^2 - 2\rho\frac{(M_{Gd} - P_{Gd}\varepsilon_{Gd})(M_H - P_H\varepsilon_H)}{\sigma_{Gd}\sigma_H}\right], \tag{8-10}$$

where ρ is the correlation coefficient of the two measurements and σ is the total uncertainty of the relevant numerator. If utilizing pull-terms in Eq. (8-10), σ would be purely statistical, and since the nGd and nH analyses use independent samples, $\rho = 0$.

Fitting with a pull term χ^2 is discussed in Appendix A.1. In this study, the nGd and nH measurements are combined analytically with the χ^2 of Eq. (8-10). To do this, ρ is determined from the correlation constants of the individual efficiencies, ρ_ε.

8.3.2 Correlations

This section presents estimates of correlation coefficients for the various efficiencies in the nGd and nH analyses. Appendix A.2 describes how the correlation between efficiencies is generally determined by the correlation between their systematic uncertainties, and furthermore, how ρ is generally less than 1. Here, the basic approach to determining coupling constants is outlined.

Some efficiencies are determined very precisely such that their uncertainties are negligible. They are not assigned a correlation coefficient. Identically, $\rho = 0$.

Efficiencies determined with independent methods or subject to unrelated sources of uncertainty are taken to be uncorrelated: $\rho = 0$.

Some efficiencies are determined by the same method (or selection criteria) or are subject to identical sources of uncertainty. These are taken to be fully correlated: $\rho = 1$. Beyond these simple cases, ρ can be estimated from knowledge of the uncertainties. This is explained in Section 4. In addition, non-zero correlation coefficients may be conservatively assigned $\rho = 1$. This is also explained later.

Table 1 lists the IBD selection criteria of the nGd and nH analyses. Since efficiencies from identical criteria are generally equal, the first five selections, and the ninth and tenth criteria, listed in Table 5.1 are fully correlated (have $\rho = 1$).

Efficiencies determined by the sixth, seventh, and eighth selections have precisely determined efficiencies and therefore, are assigned $\rho = 0$. Although DAQ time is counted identically between the analyses, it belongs to this category.

The selections of primary importance are the last four listed in Table 5.1. In addition to these, correlation coefficients are given for the number of target protons. Coefficients are discussed for the AD-uncorrelated uncertainty of each IBD selection efficiency and background in the relevant sections of Chapters 7 and 6. They are summarized in Tables 7.2 and 8.3.

Table 8.3 Summary of input used in the combination of the *n*Gd and *n*H results for $\sin^2 2\theta_{13}$: background uncertainties relative to the IBD rates in EH3 for the *n*Gd and *n*H analyses and their individual correlation coefficients. The combined correlation coefficient also includes the correlation for efficiencies. See the text for details.

	*n*Gd [%]	*n*H [%]	Correlation
^{9}Li/^{8}He	0.19	0.20	0
Accidental	0.02	0.08	0
Am-C	0.05	0.04	0.7
Fast neutron	0.01	0.06	0
^{13}C(α,n)^{16}O	0.04	0.01	0
Combined	0.20	0.22	0.05

8.3.3 Overall Correlation Coefficient

To utilize the χ^2 of Eq. (8-10), the correlation coefficients ρ_i of the AD-uncorrelated uncertainties of each efficiency ε_i are combined into the single correlation coefficient ρ. This is done by direct calculation. For illustration, we take the measurements M_1 and M_2 to be proportional to the products of their efficiencies: $M_k \propto \prod_{i_k}^{m} \varepsilon_{i_k}$, where both measurements have m efficiencies. The result is

$$\rho = \frac{\prod_i^m (\rho_i \sigma_{i_1} \sigma_{i_2} + 1) - 1}{\sigma_{M_1} \sigma_{M_2}}, \tag{8-11}$$

where

$$\sigma_{M_k} \equiv \left[\sum_{i_k}^{m} \sigma_{i_k}^2 \right]^{1/2}, \tag{8-12}$$

and σ_{i_k} is the relative uncertainty of ε_{i_k}.

Building on this basic expression, we consider an expression for the expected number of IBDs in different volumes v based on Eq. (3-1):

$$N_k = \varepsilon_{0_k} \sum_{v_k} \varepsilon_{v_k}, \tag{8-13}$$

where ε_v is the efficiency-weighted number of target protons for volume v as in Eq. (7-1), but including only the fraction of neutron captures as an efficiency. The coincidence-time and prompt- and delayed-energy selection efficiencies are excluded from ε_v because the uncertainties of these quantities were determined with data from the combined scintillator volume, as described in Chapter 7. Thus, ε_0 is the product of the predicted number of IBDs per target proton expressed as Φ in Eq. (3-2), and all other (full-volume) selection efficiencies, excluding the neutron capture fractions. The small contribution of events in acrylic is ignored so that for each quantity in ε_v, there are two correlation coefficients between the GdLS volume of the nGd measurement M_1 and the GdLS and LS volumes of the nH measurement M_2. Performing the same calculation as for Eq. (8-11) gives

$$\rho = \frac{p_0\left(\frac{\varepsilon_{Gd_2}}{\varepsilon_{Gd_2}+\varepsilon_{LS_2}} p_{Gd_1,Gd_2} + \frac{\varepsilon_{LS_2}}{\varepsilon_{Gd_2}+\varepsilon_{LS_2}} p_{Gd_1,LS_2}\right) - 1}{\sigma_{M_1}\sigma_{M_2}}, \tag{8-14}$$

where

$$p_0 \equiv \prod_i^m (\rho_{0i}\sigma_{0i_1}\sigma_{0i_2} + 1), \tag{8-15}$$

$$p_{Gd_1,v_2} \equiv \prod_i^l (\rho_{i,Gd_1,v_2}\sigma_{i,Gd_1}\sigma_{i,v_2} + 1), \tag{8-16}$$

$$\sigma_{M_2} \equiv \left[\sigma_{0_2}^2 + \frac{\sigma_{Gd_2}^2/\varepsilon_{LS_2}^2 + \sigma_{LS_2}^2/\varepsilon_{Gd_2}^2 + C}{(1/\varepsilon_{LS_2} + 1/\varepsilon_{Gd_2})^2}\right]^{1/2}, \tag{8-17}$$

$$C = 2\sum_i^l \rho_i\sigma_{i,Gd}\sigma_{i,LS}. \tag{8-18}$$

Here, $l = 2$ (proton numbers and neutron capture fractions) and m represents all other selection efficiencies. C accounts for the correlations between an efficiency in different volumes for the nH analysis. This uncertainty in proton number is uncorrelated while the capture fraction uncertainty is fully correlated. Of course, C does not exist in the nGd case and so, σ_{M_1} is a much simpler expression.

The uncertainty of $\sin^2 2\theta_{13}$ is essentially the uncertainty of $N_{\mathrm{far}}/N_{\mathrm{near}}$. Taking EH1 and EH3 to represent near and far, respectively, error propagation shows that the contribution from the uncertainties of near relative to that from far is smaller by $N_{\mathrm{EH3}}/N_{\mathrm{EH1}} \approx 11\%$ (for both *n*Gd and *n*H analyses). When including statistical uncertainties, this increases to about 30%, however, since the background uncertainties among sites are similar, we take the uncertainty of only EH3 backgrounds to represent the total uncertainty of backgrounds.

Finally, to utilize the EH3 background values in Table 8.3, we must augment Eq. (8-13) so that the number of IBDs (N) includes n background terms (N_b); i.e., $N = \varepsilon_0 \sum_v \varepsilon_v + \sum_b^n N_b$. Repeating the calculation again yields

$$\rho = \frac{p_0 \left(\frac{\varepsilon_{Gd_2}}{\varepsilon_{Gd_2}+\varepsilon_{LS_2}} p_{Gd_1,Gd_2} + \frac{\varepsilon_{LS_2}}{\varepsilon_{Gd_2}+\varepsilon_{LS_2}} p_{Gd_1,LS_2} \right) - 1 + B}{\sigma_{M_1}\sigma_{M_2}}, \tag{8-19}$$

where

$$B \equiv \frac{\sum_b^n \rho_b \sigma_{b_1} \sigma_{b_2}}{\varepsilon_{0_1}\varepsilon_{0_2}\varepsilon_{Gd_1}(\varepsilon_{Gd_2}+\varepsilon_{LS_2})}, \tag{8-20}$$

$$\sigma_{M_2} \equiv \left[\sigma_{0_2}^2 + \frac{\sigma_{Gd_2}^2/\varepsilon_{LS_2}^2 + \sigma_{LS_2}^2/\varepsilon_{Gd_2}^2 + C + \sigma_{B_2}^2/(\varepsilon_{0_2}\varepsilon_{Gd_2}\varepsilon_{LS_2})^2}{(1/\varepsilon_{LS_2} + 1/\varepsilon_{Gd_2})^2} \right]^{1/2}, \tag{8-21}$$

and $\sigma_{B_2}^2 \equiv \sum_{b_2}^m \sigma_{b_2}^2$, where the σ_{b_2} are the absolute background uncertainties relative to the IBD rate, and are given with the σ_{b_1} in Tables 5.2 and 5.3.

To include statistical uncertainty in the uncertainty of measurement σ_{M_k}, we consider its significance relative to the total systematic uncertainty: σ_{M_k} is multiplied by

$$\left(1 + \sigma_{\mathrm{stat},k}^2/\sigma_{\mathrm{sys},k}^2\right)^{1/2}. \tag{8-22}$$

For the *n*Gd analysis, this is $(1+0.67/(1.00-0.67))^{1/2} = 1.74$[12]. For the *n*H analysis, it is $(1+0.518/(1.000-0.518))^{1/2} = 1.44$. Because these numbers include background uncertainties, they should be applied to Eq. (8-19) only.

The correlation coefficient ρ is calculated using the correlation coefficients ρ_ε summarized in Tables 7.2 and 8.3. The results of four calculation methods are shown in Table 8.4. The first and second constants are calculated from Eqs. (8-14) and (8-19), respectively, to illustrate the effect of the backgrounds. The third constant in Table 8.4

Table 8.4 Correlation coefficients calculated with: the correlation coefficients from Table 7.2 in Eq. (8-14) (first row), the constants from Tables 7.2 and 8.3 in Eq. (8-19) (second row), the constants from Tables 7.2 and 8.3 and the statistical uncertainty from Eq. (8-22) (third row), and the conservative estimate using Eq. (8-23).

Calculation method	ρ
ρ_i from Table 7.2 (no bkg., no stat.)	0.07
ρ_i from Tables 7.2 and 8.3 (no stat.)	0.04
ρ_i from Table 7.2 and 8.3	0.02
Conservative estimate	0.11

includes statistical uncertainty via Eq. (8-22) and provides the most realistic estimate of ρ (the second constant can be considered the statistical limit of ρ). Actually, this estimate is conservative in that it does not account for the uncertainties of the nGd spectral analysis which do not appear in the nH rate analysis. The fourth constant in Table 8.4 is an approximation made by separating a measurement's total error into correlated (σ_{Mcor}) and uncorrelated components (σ_{Muncor}):

$$\rho \approx \frac{\sigma_{M_1cor}\sigma_{M_2cor}}{\sigma_{M_1}\sigma_{M_2}} = \frac{1}{\sqrt{1+\left(\frac{\sigma_{M_1uncor}}{\sigma_{M_1cor}}\right)^2}\sqrt{1+\left(\frac{\sigma_{M_2uncor}}{\sigma_{M_2cor}}\right)^2}}. \tag{8-23}$$

This method is conservative because all correlated uncertainties are treated as fully correlated. Thus, σ_{Mcor} includes the detector, reactor, and Am-C uncertainties:

$$\rho \approx \frac{(0.192+0.048+0.007)(0.392+0.042+0.001)}{1.00\cdot 1.00} = 0.11. \tag{8-24}$$

8.3.4 nGd-nH Combined Result

The nGd and nH measurements were combined with the analytical minimization of Eq. (8-10). The solution is a weighted average

$$\sin^2 2\theta_{13} = w(\sin^2 2\theta_{13})_{nH} + (1-w)(\sin^2 2\theta_{13})_{nGd}, \tag{8-25}$$

where the weight w is given by

$$w = \frac{\sigma_{Gd}^2 - \rho\sigma_{Gd}\sigma_H}{\sigma_{Gd}^2 + \sigma_H^2 - 2\rho\sigma_{Gd}\sigma_H}. \tag{8-26}$$

The uncertainty of the average is given by

$$\sigma^2 = \frac{\sigma_{Gd}^2\sigma_H^2(1 - \rho^2)}{\sigma_{Gd}^2 + \sigma_H^2 - 2\rho\sigma_{Gd}\sigma_H}. \tag{8-27}$$

The values for ρ from Table 8.4 are substituted into Eqs. (8-26) and (8-27) to determine the central value and uncertainty, respectively. The two results for $\sin^2 2\theta_{13}$ given in Eqs. (8-8) and (8-7) in Section 8.2, are combined. With the realistic estimate of $\rho = 0.018$, we obtain $w = 0.155$, and

$$\sin^2 2\theta_{13} = 0.082 \pm 0.004, \tag{8-28}$$

which is a 7.7% improvement in precision.

With the conservative estimate of $\rho = 0.149$, we obtain $w = 0.144$, $\sin^2 2\theta_{13} = 0.082$, and $\sigma = 0.004$, which is a 5.0% improvement.

The realistic and conservative estimates of $\sin^2 2\theta_{13}$ are indistinguishable at the level of precision presented. The two uncertainty estimates are illustrated in Figure 8.4, which shows the improvement in uncertainty versus ρ.

8.3.5 Summary

Two methods for incorporating correlations in a χ^2 have been presented. Values for correlation coefficients of systematic uncertainties in the *n*Gd and *n*H analyses have been supplied in Chapters 7 and 6. AD-uncorrelated uncertainties were found to have a small correlation, showing that the *n*Gd and *n*H analyses provide independent measurements of θ_{13}. The combination of the *n*H rate analysis with the *n*Gd spectral analysis improved the precision of the uncertainty by about 8%.

8.4 Summary

Estimating all relevant backgrounds and the efficiency-weighted number of target protons, and their uncertainties, a quantitative model-independent evaluation of

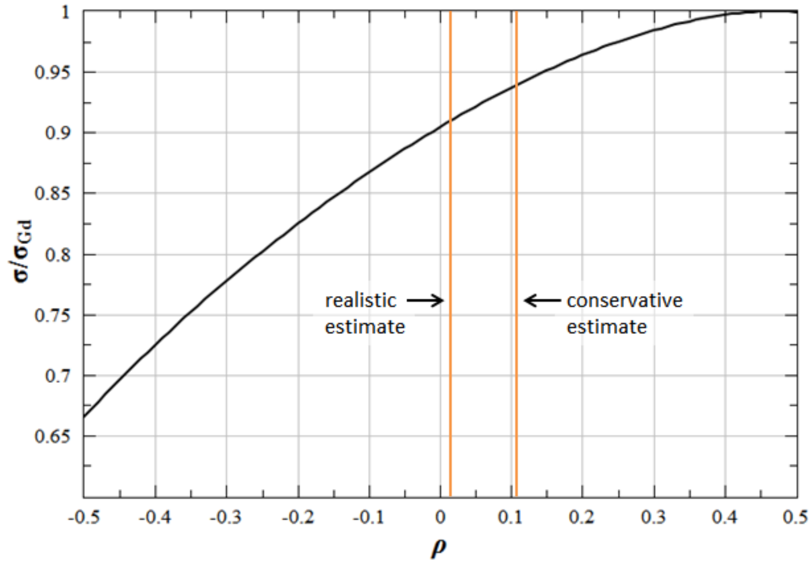

Figure 8.4 Uncertainty of the combined measurement relative to the smallest uncertainty of the two original measurements (nGd) as a function of correlation coefficient. Because the two analyses have different uncertainties, the most conservative value of ρ is less than 1, as described in Appendix A.3. In this case, it is 0.48, where there is no improvement of the original nGd uncertainty.

$\overline{\nu}_e$-disappearance is presented. In the three-flavor-neutrino oscillation framework, the nGd- and nH-IBD analyses provide the first- and second-most precise results for mixing angle θ_{13}:

$$\begin{aligned} n\mathrm{Gd} : \sin^2 2\theta_{13} &= 0.084 \pm 0.005, \\ n\mathrm{H} : \sin^2 2\theta_{13} &= 0.071 \pm 0.011. \end{aligned} \tag{8-29}$$

Studying the correlations between the backgrounds and efficiencies of the two analyses, their results were combined to provide the most precise determination of θ_{13}:

$$\sin^2 2\theta_{13} = 0.082 \pm 0.004, \tag{8-30}$$

which is an 8% improvement in precision over the nGd-IBD analysis alone.

In the future, combinations may be performed with other experiments; namely, RENO and Double Chooz, which are estimated to contribute at the level of the current nH-IBD analysis.

Chapter 9 Summary

The precision to which neutrino mixing angle θ_{13} is determined is vital to constraining the leptonic *CP* phase δ_{CP} in conjunction with accelerator experiments[1–4]. Discovery of *CP*-symmetry violation among neutrinos may explain the basic question of why there is more matter than antimatter in the universe.

This thesis presents a new independent measurement of $\sin^2 2\theta_{13}$ at the Daya Bay Reactor Neutrino Experiment using a 621-day sample of 780000 *n*H IBDs (distinct from the 1240000 *n*Gd IBDs). The rates of these IBDs were measured at different baselines, and after subtracting backgrounds and correcting for selection efficiencies and detector energy response, analysis within the three-neutrino-oscillation framework yields $\sin^2 2\theta_{13} = 0.071 \pm 0.011$. Correlations between this *n*H analysis and the *n*Gd analysis from Daya Bay were evaluated and led to a most precise, combined measurement of $\sin^2 2\theta_{13} = 0.082 \pm 0.004$.

Figure 1.1 in Chapter 1 shows constrained regions of δ_{CP} $vs.$ $\sin^2 \theta_{13}$ from T2K and reactor experiments. Figure 9.1 below shows the same constrained regions, but with the addition of blue lines representing the measured value and uncertainty of the most precise combined result of $\sin^2 2\theta_{13}$. A significant shift to a smaller value of $\sin^2 \theta_{13}$ is apparent, as well as a large reduction in uncertainty, paving the way for greater constraints on δ_{CP} and the possible discovery of leptonic *CP* violation.

The precision of the Daya Bay experiment should ultimately be limited by systematic uncertainties, particularly, those related to the performance of the $\overline{\nu}_e$ detectors. Knowing this, new techniques and models were developed to quantify systematic uncertainties and to obtain a basic understanding of the energy response of scintillation detectors. This understanding has laid the foundation for a spectral analysis of the prompt-energy spectrum from *n*H IBDs, which will further improve the precision of $\sin^2 2\theta_{13}$. This analysis would also provide a new determination of the neutrino mass-squared difference Δm^2_{32}. Additionally, the data-driven techniques developed to study the accidental, ^{9}Li, and fast neutron backgrounds could be useful for other experiments, especially those that use or plan to use *n*H-IBDs, such as JUNO[30].

In summary, the achievements in this thesis help provide the most reliable and accurate measurements of $\sin^2 2\theta_{13}$, will be useful for improving these measurements in

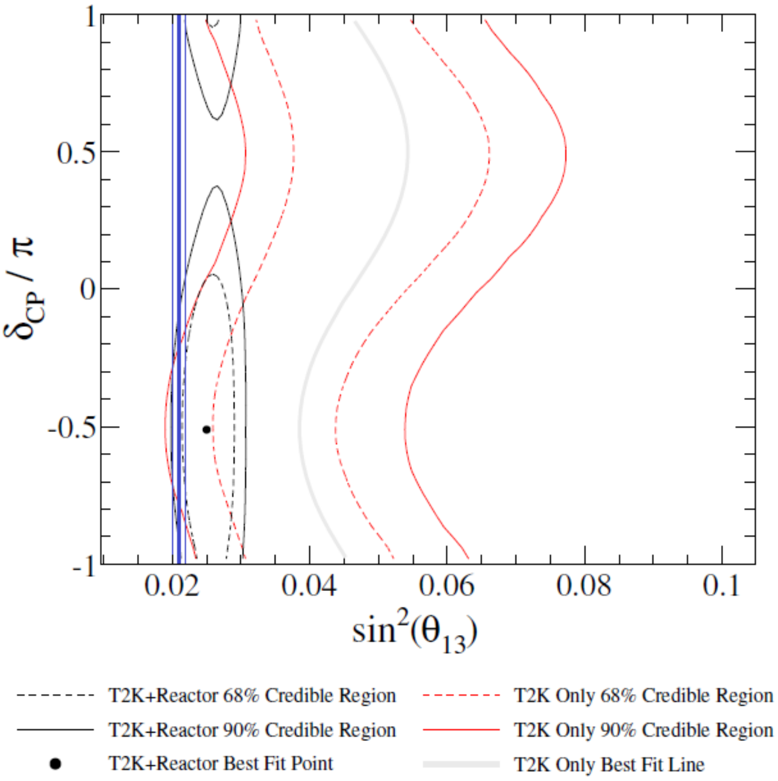

Figure 9.1 Constraints on δ_{CP} $vs.$ $\sin^2\theta_{13}$ from the T2K experiment alone (red and grey curves) and when combined with θ_{13} from reactor experiments (black). The vertical blue lines represent the value and uncertainty of $\sin^2\theta_{13}$ resulting from the combination of the 621-day nH and nGd analyses from Daya Bay. The original figure is shown in Fig. 1.1 and is from Ref.[1].

the future (including Δm^2_{32}), and can be useful for future and ongoing experiments that use scintillation detectors.

References

[1] Abe, K. and others. *Measurements of neutrino oscillation in appearance and disappearance channels by the T2K experiment with 6.6×10^{20} protons on target.* Phys. Rev., 2015, D91(7):072010.

[2] Ayres, D. S. and others. *The NOvA Technical Design Report.* 2007..

[3] Adamson, P. and others. *Combined analysis of ν_μ disappearance and $\nu_\mu \rightarrow \nu_e$ appearance in MINOS using accelerator and atmospheric neutrinos.* Phys. Rev. Lett., 2014, 112:191801.

[4] Adams, C. and others. *The Long-Baseline Neutrino Experiment: Exploring Fundamental Symmetries of the Universe.* 2013.

[5] Abe, Y. and others. *Indication for the disappearance of reactor electron antineutrinos in the Double Chooz experiment.* Phys. Rev. Lett., 2012, 108:131801.

[6] Abe, K. and others. *Indication of Electron Neutrino Appearance from an Accelerator-produced Off-axis Muon Neutrino Beam.* Phys. Rev. Lett., 2011, 107:041801.

[7] Adamson, P. and others. *Improved search for muon-neutrino to electron-neutrino oscillations in MINOS.* Phys. Rev. Lett., 2011, 107:181802.

[8] Apollonio, M. and others. *Search for neutrino oscillations on a long baseline at the CHOOZ nuclear power station.* Eur. Phys. J., 2003, C27:331–374.

[9] Piepke, A. *Final results from the Palo Verde neutrino oscillation experiment.* Prog. Part. Nucl. Phys., 2002, 48:113–121. [,113(2002)].

[10] Yamamoto, S. and others. *An Improved search for $\nu_\mu \rightarrow \nu_e$ oscillation in a long-baseline accelerator experiment.* Phys. Rev. Lett., 2006, 96:181801.

[11] An, F. P. and others. *Observation of electron-antineutrino disappearance at Daya Bay.* Phys. Rev. Lett., 2012, 108:171803.

[12] An, F. P. and others. *New Measurement of Antineutrino Oscillation with the Full Detector Configuration at Daya Bay.* Phys. Rev. Lett., 2015, 115(11):111802.

[13] Choi, J. H. and others. *Observation of Energy and Baseline Dependent Reactor Antineutrino Disappearance in the RENO Experiment.* Phys. Rev. Lett., 2016, 116(21):211801.

[14] Abrahão, T. and others. *Measurement of θ_{13} in Double Chooz using neutron captures on hydrogen with novel background rejection techniques.* JHEP, 2016, 01:163. [JHEP01,163(2016)].

[15] An, F. P. and others. *Independent measurement of the neutrino mixing angle θ_{13} via neutron capture on hydrogen at Daya Bay.* Phys. Rev., 2014, D90(7):071101.

[16] Abe, Y. and others. *Improved measurements of the neutrino mixing angle θ_{13} with the Double Chooz detector.* JHEP, 2014, 10:086. [Erratum: JHEP02,074(2015)].

[17] Abe, K. and others. *Observation of Electron Neutrino Appearance in a Muon Neutrino Beam.* Phys. Rev. Lett., 2014, 112:061802.

[18] Adamson, P. and others. *Electron neutrino and antineutrino appearance in the full MINOS data sample*. Phys. Rev. Lett., 2013, 110(17):171801.

[19] Ardellier, F. and others. *Double Chooz: A Search for the neutrino mixing angle θ_{13}*. 2006..

[20] Ahn, J. K. and others. *RENO: An Experiment for Neutrino Oscillation Parameter θ_{13} Using Reactor Neutrinos at Yonggwang*. 2010..

[21] Guo, Xinheng and others. *A Precision measurement of the neutrino mixing angle θ_{13} using reactor antineutrinos at Daya-Bay*. 2007..

[22] Abe, Y. and others. *First Measurement of θ_{13} from Delayed Neutron Capture on Hydrogen in the Double Chooz Experiment*. Phys. Lett., 2013, B723:66–70.

[23] Kim, S. B. Neutrino Oscillation Workshop, Otranto, Italy, 7-14 September 2014 (unpublished).

[24] Eguchi, K. and others. *First results from KamLAND: Evidence for reactor anti-neutrino disappearance*. Phys. Rev. Lett., 2003, 90:021802.

[25] Araki, T. and others. *Experimental investigation of geologically produced antineutrinos with KamLAND*. Nature, 2005, 436:499–503.

[26] Bellini, G. and others. *Observation of Geo-Neutrinos*. Phys. Lett., 2010, B687:299–304.

[27] Agostini, M. and others. *Borexino's search for low-energy neutrino and antineutrino signals correlated with gamma-ray bursts*. Astropart. Phys., 2017, 86:11–17.

[28] Zhang, H. and others. *Supernova Relic Neutrino Search with Neutron Tagging at Super-Kamiokande-IV*. Astropart. Phys., 2015, 60:41–46.

[29] Wurm, Michael and others. *The next-generation liquid-scintillator neutrino observatory LENA*. Astropart. Phys., 2012, 35:685–732.

[30] An, Fengpeng and others. *Neutrino Physics with JUNO*. J. Phys., 2016, G43(3):030401.

[31] Pauli, Wolfgang. Letter sent to the Tubingen conference, December, 1930..

[32] Fermi, E. *Trends to a Theory of beta Radiation. (In Italian)*. Nuovo Cim., 1934, 11:1–19. [,535(1934)].

[33] Arnison, G. and others. *Experimental Observation of Isolated Large Transverse Energy Electrons with Associated Missing Energy at s**(1/2) = 540-GeV*. Phys. Lett., 1983, B122:103–116. [,611(1983)].

[34] Banner, M. and others. *Observation of Single Isolated Electrons of High Transverse Momentum in Events with Missing Transverse Energy at the CERN anti-p p Collider*. Phys. Lett., 1983, B122:476–485.

[35] Arnison, G. and others. *Experimental Observation of Lepton Pairs of Invariant Mass Around 95-GeV/c**2 at the CERN SPS Collider*. Phys. Lett., 1983, B126:398–410.

[36] Bagnaia, P. and others. *Evidence for Z0 —> e+ e- at the CERN anti-p p Collider*. Phys. Lett., 1983, B129:130–140.

[37] Cowan, C. L. and Reines, F. and Harrison, F. B. and Kruse, H. W. and McGuire, A. D. *Detection of the free neutrino: A Confirmation*. Science, 1956, 124:103–104.

[38] Danby, G. and Gaillard, J. M. and Goulianos, Konstantin A. and Lederman, L. M. and Mistry, Nari B. and Schwartz, M. and Steinberger, J. *Observation of High-Energy Neutrino Reactions and the Existence of Two Kinds of Neutrinos*. Phys. Rev. Lett., 1962, 9:36–44.

[39] Kodama, K. and others. *Observation of tau neutrino interactions.* Phys. Lett., 2001, B504:218–224.

[40] Schael, S. and others. *Precision electroweak measurements on the Z resonance.* Phys. Rept., 2006, 427:257–454.

[41] Ade, P. A. R. and others. *Planck 2015 results. XIII. Cosmological parameters.* Astron. Astrophys., 2016, 594:A13.

[42] Palanque-Delabrouille, Nathalie and others. *Neutrino masses and cosmology with Lyman-alpha forest power spectrum.* JCAP, 2015, 1511(11):011.

[43] Davis, Jr., Raymond and Harmer, Don S. and Hoffman, Kenneth C. *Search for neutrinos from the sun.* Phys. Rev. Lett., 1968, 20:1205–1209.

[44] Fukuda, Y. and others. *Evidence for oscillation of atmospheric neutrinos.* Phys. Rev. Lett., 1998, 81:1562–1567.

[45] Ahmad, Q. R. and others. *Measurement of the rate of* $\nu_e + d \to p + p + e^-$ *interactions produced by* ^8B *solar neutrinos at the Sudbury Neutrino Observatory.* Phys. Rev. Lett., 2001, 87:071301.

[46] Pontecorvo, B. *Mesonium and anti-mesonium.* Sov. Phys. JETP, 1957, 6:429. [Zh. Eksp. Teor. Fiz.33,549(1957)].

[47] Maki, Ziro and Nakagawa, Masami and Sakata, Shoichi. *Remarks on the unified model of elementary particles.* Prog. Theor. Phys., 1962, 28:870–880.

[48] Olive, K. A. and others. *Review of Particle Physics.* Chin. Phys., 2014, C38:090001.

[49] An, F. P. and others. *Spectral measurement of electron antineutrino oscillation amplitude and frequency at Daya Bay.* Phys. Rev. Lett., 2014, 112:061801.

[50] Ma, X. B. and Zhong, W. L. and Wang, L. Z. and Chen, Y. X. and Cao, J. *Improved calculation of the energy release in neutron-induced fission.* Phys. Rev., 2013, C88(1):014605.

[51] Mueller, Th. A. and others. *Improved Predictions of Reactor Antineutrino Spectra.* Phys. Rev., 2011, C83:054615.

[52] Huber, Patrick. *On the determination of anti-neutrino spectra from nuclear reactors.* Phys. Rev., 2011, C84:024617. [Erratum: Phys. Rev.C85,029901(2012)].

[53] An, Feng Peng and others. *Measurement of the Reactor Antineutrino Flux and Spectrum at Daya Bay.* Phys. Rev. Lett., 2016, 116(6):061801.

[54] An, Feng-Peng and Tian, Xin-Chun and Zhan, Liang and Cao, Jun. *Systematic impact of spent nuclear fuel on Theta(13) sensitivity at reactor neutrino experiment.* Chin. Phys., 2009, C33:711–716.

[55] Zhou, Bin and Ruan, Xi-Chao and Nie, Yang-Bo and Zhou, Zu-Ying and An, Feng-Peng and Cao, Jun. *A study of antineutrino spectra from spent nuclear fuel at Daya Bay.* Chin. Phys., 2012, C36:1–5.

[56] An, F. P. and others. *Improved Measurement of Electron Antineutrino Disappearance at Daya Bay.* Chin. Phys., 2013, C37:011001.

[57] An, Feng Peng and others. *Improved Measurement of the Reactor Antineutrino Flux and Spectrum at Daya Bay.* 2016..

[58] Vogel, P. and Beacom, John F. *Angular distribution of neutron inverse beta decay, $\overline{\nu}_e + p \rightarrow e^+ + n$.* Phys. Rev., 1999, D60:053003.

[59] An, F. P. and others. *The Detector System of The Daya Bay Reactor Neutrino Experiment.* Nucl. Instrum. Meth., 2016, A811:133–161.

[60] Band, H. R. and others. *Acrylic Target Vessels for a High-Precision Measurement of θ_{13} with the Daya Bay Antineutrino Detectors.* JINST, 2012, 7:P06004.

[61] Beriguete, Wanda and others. *Production of a gadolinium-loaded liquid scintillator for the Daya Bay reactor neutrino experiment.* Nucl. Instrum. Meth., 2014, A763:82–88.

[62] Liu, J. and others. *Automated calibration system for a high-precision measurement of neutrino mixing angle θ_{13} with the Daya Bay antineutrino detectors.* Nucl. Instrum. Meth., 2014, A750:19–37.

[63] Xiao Hua-Lin and Li Xiao-Bo and Zheng Dong and Cao Jun and Wen Liang-Jian and Wang Nai-Yan. *Study of absorption and re-emission processes in a ternary liquid scintillation system.* Chinese Physics C, 2010, 34(11):1724.

[64] Li Xiao-Bo and Xiao Hua-Lin and Cao Jun and Li Jin and Ruan Xi-Chao and Heng Yue-Kun. *Timing properties and pulse shape discrimination of LAB-based liquid scintillator.* Chinese Physics C, 2011, 35(11):1026.

[65] http://www.hamamatsu.com/resources/pdf/etd/LARGE_AREA_PMT_TPMH1286E.pdf.

[66] Band, H. R. and others. *Target Mass Monitoring and Instrumentation in the Daya Bay Antineutrino Detectors.* JINST, 2013, 8:T04001.

[67] An, F. P. and others. *The muon system of the Daya Bay Reactor antineutrino experiment.* Nucl. Instrum. Meth., 2015, A773:8–20.

[68] An, F. P. and others. *A side-by-side comparison of Daya Bay antineutrino detectors.* Nucl. Instrum. Meth., 2012, A685:78–97.

[69] Gong, Hui and Lin, Yan-Chang and Gong, Guang-Hua and Xue, Tao and Wang, Xi and Shao, Bei-Bei and Chen, Shaomin and Li, Xiao-Nan and Wang, Zheng and Li, Qiu-Ju. *Design of the local trigger board for the Daya Bay reactor neutrino experiment.* Nucl. Instrum. Meth., 2011, A637:138–142.

[70] Li, Fei and Ji, Xiao-Lu and Li, Xiao-Nan and Zhu, Kejun. *DAQ architecture design of Daya Bay reactor neutrino experiment.* IEEE Trans. Nucl. Sci., 2011, 58:1723–1727.

[71] Oreglia, M. *A Study of the Reactions $\psi' \rightarrow \gamma\gamma\psi$*[D]. SLAC, 1980.

[72] J B Birks. *Scintillations from Organic Crystals: Specific Fluorescence and Relative Response to Different Radiations.* Proceedings of the Physical Society. Section A, 1951, 64(10):874.

[73] An, Feng Peng and others. *Measurement of electron antineutrino oscillation based on 1230 days of operation of the Daya Bay experiment.* 2016..

[74] http://physics.nist.gov/PhysRefData/XrayMassCoef/ComTab/polyethylene.html.

[75] Cheng, Jia-Hua and Wang, Zhe and Lebanowski, Logan and Lin, Guey-Lin and Chen, Shaomin. *Determination of the total absorption peak in an electromagnetic calorimeter.* Nucl. Instrum. Meth., 2016, A827:165–170.

[76] Yu, Jing-Yi and Wang, Zhe and Chen, Shao-Min. *A precise calculation of delayed coincidence selection efficiency and accidental coincidence rate*. Chin. Phys., 2015, C39(5):056201.

[77] Wen, Liang-jian and Cao, Jun and Luk, Kam-Biu and Ma, Yu-qian and Wang, Yi-fang and Yang, Chang-gen. *Measuring cosmogenic Li-9 background in a reactor neutrino experiment*. Nucl. Instrum. Meth., 2006, A564:471–474.

[78] Abe, S. and others. *Production of Radioactive Isotopes through Cosmic Muon Spallation in KamLAND*. Phys. Rev., 2010, C81:025807.

[79] Khalchukov, F. F. and Korolkova, E. V. and Kudryavtsev, V. A. and Malguin, A. S. and Ryasnii, V. G. and Ryazhskaya, O. G. and Zatsepin, G. T. and Saavedra, O. *Hadrons and other secondaries generated by cosmic ray muons underground*. Nuovo Cim., 1995, C18:517–529.

[80] Hagner, T. and von Hentig, R. and Heisinger, B. and Oberauer, L. and Schonert, Stefan. and von Feilitzsch, F. and Nolte, E. *Muon induced production of radioactive isotopes in scintillation detectors*. Astropart. Phys., 2000, 14:33–47.

[81] Wang, Y. F. and Balic, V. and Gratta, G. and Fasso, A. and Roesler, S. and Ferrari, A. *Predicting neutron production from cosmic ray muons*. Phys. Rev., 2001, D64:013012.

[82] Liu, J. and Carr, R. and Dwyer, D. A. and Gu, W. Q. and Li, G. S. and McKeown, R. D. and Qian, X. and Tsang, R. H. M. and Wu, F. F. and Zhang, C. *Neutron Calibration Sources in the Daya Bay Experiment*. Nucl. Instrum. Meth., 2015, A797:260–264.

[83] Gu, W. Q. and Cao, G. F. and Chen, X. H. and Ji, X. P. and Li, G. S. and Ling, J. J. and Liu, J. and Qian, X. and Wang, W. *Background Evaluation for the Neutron Sources in the Daya Bay Experiment*. Nucl. Instrum. Meth., 2016, A833:27–32.

[84] Hennings-Yeomans, Raul and Akerib, D. S. *A Neutron Multiplicity Meter for Deep Underground Muon-Induced High Energy Neutron Measurements*. Nucl. Instrum. Meth., 2007, A574:89–97.

[85] Agostinelli, S. and others. *GEANT4: A Simulation toolkit*. Nucl. Instrum. Meth., 2003, A506:250–303.

[86] Allison, John and others. *Geant4 developments and applications*. IEEE Trans. Nucl. Sci., 2006, 53:270.

[87] Chadwick, M. B. and others. *ENDF/B-VII.1 Nuclear Data for Science and Technology: Cross Sections, Covariances, Fission Product Yields and Decay Data*. Nucl. Data Sheets, 2011, 112(12):2887–2996.

[88] Band, H. R. and others. *The Daya Bay Antineutrino Detector Filling System and Liquid Mass Measurement*. JINST, 2013, 8:P09015.

Acknowledgments

The data used in this study is a result of the efforts of many physicists, engineers, and students. I thank all those who contributed to the Daya Bay Reactor Neutrino Experiment. I thank my scientific advisor during my undergraduate and Master's periods, professor Kwong Lau, for years of guidance and support, along with the physics department at the University of Houston. I thank the members of the neutrino physics group at Tsinghua University led by professors Shaomin Chen and Zhe Wang, for a stimulating professional and personal experience. In particular, I acknowledge my colleagues at Tsinghua, Xiangpan Ji, Beizhen Hu (of National Taiwan University), Hanyu Wei, and Yiming Zhang, who contributed numerous components of this study. I appreciate the support provided by the China Scholarship Council. And finally, I sincerely appreciate the patience, support, and courage of my wife.

Declaration

本人郑重声明：所呈交的学位论文，是本人在导师指导下，独立进行研究工作所取得的成果。尽我所知，除文中已经注明引用的内容外，本学位论文的研究成果不包含任何他人享有著作权的内容。对本论文所涉及的研究工作做出贡献的其他个人和集体，均已在文中以明确方式标明。

签　名：＿＿＿＿＿＿ 日　期：＿＿＿＿＿＿

Appendix A Handling Correlations

A.1 Correlations in a pull-term χ^2

A nuisance parameter can be expressed as the difference between the estimated and actual efficiency:

$$\eta \equiv \frac{\delta\varepsilon}{\varepsilon} = \frac{\varepsilon - \mu_\varepsilon}{\varepsilon}. \tag{A-1}$$

Thus, a pull-term has the same form as a χ^2 formula:

$$\left(\frac{\eta}{\sigma_\varepsilon}\right)^2 = \eta^2\left(\frac{1}{\sigma_\varepsilon}\right)^2 = \left(\frac{\delta\varepsilon}{\varepsilon}\right)^2\left(\frac{\varepsilon}{\sigma_{\mathrm{abs}}}\right)^2 = \left(\frac{\varepsilon - \mu_\varepsilon}{\sigma_{\mathrm{abs}}}\right)^2, \tag{A-2}$$

where σ_{abs} is the absolute uncertainty of ε. So, we express the correlation between efficiencies using pull-terms with the same general form of Eq. (8-10):

$$\frac{1}{1-\rho_\varepsilon^2}\left[\left(\frac{\eta_{\varepsilon Gd}}{\sigma_{\varepsilon Gd}}\right)^2 + \left(\frac{\eta_{\varepsilon H})}{\sigma_{\varepsilon H}}\right)^2 - 2\rho_\varepsilon\frac{\eta_{\varepsilon Gd}\eta_{\varepsilon H}}{\sigma_{\varepsilon Gd}\sigma_{\varepsilon H}}\right]. \tag{A-3}$$

By its derivation, this formulation is identical to using a covariance matrix for the two nuisance parameters and could be expanded to include couplings between more than two efficiencies. Though it is not necessarily identical to using a covariance matrix in the normal χ^2, depending on how the nuisance parameters are handled.

The final form of the pull term χ^2 with correlations is

$$\begin{aligned}\chi^2 = &\left[\left(\frac{M_{Gd} - P_{Gd}\varepsilon_{Gd}(1+\eta_{\varepsilon Gd})}{\sigma_{Gd}}\right)^2 + \left(\frac{M_H - P_H\varepsilon_H(1+\eta_{\varepsilon H})}{\sigma_H}\right)^2\right] + \\ &\frac{1}{1-\rho_\varepsilon^2}\left[\left(\frac{\eta_{\varepsilon Gd}}{\sigma_{\varepsilon Gd}}\right)^2 + \left(\frac{\eta_{\varepsilon H}}{\sigma_{\varepsilon H}}\right)^2 - 2\rho_\varepsilon\frac{\eta_{\varepsilon Gd}\eta_{\varepsilon H}}{\sigma_{\varepsilon Gd}\sigma_{\varepsilon H}}\right].\end{aligned} \tag{A-4}$$

For the case $\rho < 0$, the nuisance parameters ($\eta_{\varepsilon Gd}$ and $\eta_{\varepsilon H}$) have opposite signs. This approach can be used identically for correlations between efficiencies of a single measurement.

Fitting with Eq. (A-4) requires about 10 pull terms to describe correlations, while combining two measurements can be done analytically with the normal χ^2 of Eq. (8-10). To do this, ρ is determined from all the ρ_ε.

A.2 Correlated variables

To introduce some characteristics of correlation and illustrate the pull term formulation, we look at the case of full correlation ($\rho_\varepsilon = 1$). An expression of full correlation between two determined efficiencies is

$$\begin{aligned} \varepsilon_{Gd} &= \mu_{\varepsilon,Gd} + \theta, \\ \varepsilon_H &= \mu_{\varepsilon,H} + c\theta, \end{aligned} \tag{A-5}$$

where θ is a random variable with standard deviation σ. The true efficiencies, $\mu_{\varepsilon,i}$, may be independent, but the determined values, ε_i, are fully correlated via systematic uncertainty, θ. In this case, the relative uncertainties of the ε_i differ by a factor of c, which also appears in the nuisance parameter as defined in Eq. (A-1), thus cancelling in Eq. (A-3) to produce a single pull-term and single nuisance parameter, as expected when $\rho_\varepsilon = 1$. It is straightforward to see that when $\rho_\varepsilon = 0$, Eq. (A-3) results in two independent pull-terms and nuisance parameters.

The correlation between efficiencies is generally determined by the correlation between their systematic uncertainties, and is often complicated by the presence of more than one component of uncertainty:

$$\begin{aligned} \varepsilon_{Gd} &= \mu_{\varepsilon,Gd} + \theta_1 + \theta_2 + \ldots, \\ \varepsilon_H &= \mu_{\varepsilon,H} + c_1\theta_1 + c_2\theta_2 + \ldots. \end{aligned} \tag{A-6}$$

This generally limits ρ to be < 1. If each component is fully correlated as in Eq. (A-6), ρ can reach 1 only if all θ_i share a single proportionality constant; i.e., if all c_i are equal. Therefore, assigning a ρ_ε of 1 is either conservative (as in the case of this study) or aggressive, as described in Appendix A.3.

One could imagine a dependence of μ_ε on a parameter, such as temperature. In this case, one could simply take μ_ε to be the true efficiency at a particular temperature. A correction could be applied for the change in temperature, for which θ_i would represent the uncertainty.

It should be noted that the presence of statistical uncertainty affects the level of correlation. For the *n*Gd and *n*H analyses, it is conservatively assumed that deviations in ε_i from $\mu_{\varepsilon i}$ are dominated by systematic deviations for all i.

A.3 The most conservative value of ρ: $\rho_{\max}$

"Most conservative" refers to the least improvement in the uncertainty of the combined measurement, as expressed by Eq. (8-27). The most conservative value of ρ ($\rho_{\max}$) is found to be ≤ 1 by taking the derivative of Eq. (8-27) with respect to ρ. The solution is simply

$$\rho_{\max} = \frac{\sigma_2}{\sigma_1}, \tag{A-7}$$

where the σ_i are absolute uncertainties and $\sigma_1 > \sigma_2$.

Equation (A-7) does not apply to the component correlation coefficients ρ_ε as in Eq. (8-11), for example. In this case, the most conservative value of ρ_ε is 1 (-1), if $\rho \ll \rho_{\max}$ ($\gg \rho_{\max}$). A single most conservative values is easily confirmed by observing ρ during a scan on ρ_ε, as done for the low-energy criterion in Section 7.2.

Appendix B Data needed to reproduce the fit of $\sin^2 2\theta_{13}$ using nH IBDs

B.1 Predicted reactor antineutrino spectra $dN_r(E)/dE$

Tables B.1-B.5 provide the predicted reactor antineutrino energy spectrum from each nuclear reactor integrated over the data acquisition periods of each AD [$dN_r(E)/dE$ from Eq. (2-6)]. Because EH2-AD2 and EH3-AD4 were installed after the other six ADs, they have distinct predicted spectra given in Tables B.3 and B.5, respectively.

Table B.1 Predicted reactor antineutrino energy spectrum from each nuclear reactor integrated over the data acquisition time of EH1 (2011/12/24-2013/11/27). Applicable to both ADs in EH1. The energy bins are presented as lower and upper bin edges.

Energy [MeV]	Reactor 1	Reactor 2	Reactor 3	Reactor 4	Reactor 5	Reactor 6
(1.375, 1.625)	6.1430e+27	6.7985e+27	6.2797e+27	6.7112e+27	6.7924e+27	6.0289e+27
(1.625, 1.875)	5.4706e+27	6.0584e+27	5.5882e+27	5.9682e+27	6.0418e+27	5.3642e+27
(1.875, 2.125)	4.6443e+27	5.1401e+27	4.7425e+27	5.0664e+27	5.1278e+27	4.5526e+27
(2.125, 2.375)	3.9433e+27	4.3614e+27	4.0253e+27	4.3013e+27	4.3526e+27	3.8643e+27
(2.375, 2.625)	3.1962e+27	3.5400e+27	3.2655e+27	3.4875e+27	3.5283e+27	3.1319e+27
(2.625, 2.875)	2.6949e+27	2.9797e+27	2.7516e+27	2.9412e+27	2.9743e+27	2.6398e+27
(2.875, 3.125)	2.2495e+27	2.4898e+27	2.2988e+27	2.4566e+27	2.4851e+27	2.2055e+27
(3.125, 3.375)	1.8608e+27	2.0685e+27	1.9068e+27	2.0343e+27	2.0583e+27	1.8261e+27
(3.375, 3.625)	1.5304e+27	1.7008e+27	1.5682e+27	1.6734e+27	1.6932e+27	1.5022e+27
(3.625, 3.875)	1.2270e+27	1.3641e+27	1.2575e+27	1.3416e+27	1.3579e+27	1.2048e+27
(3.875, 4.125)	9.7573e+26	1.0878e+27	1.0017e+27	1.0676e+27	1.0803e+27	9.5821e+26
(4.125, 4.375)	7.7159e+26	8.5915e+26	7.9149e+26	8.4398e+26	8.5411e+26	7.5770e+26
(4.375, 4.625)	5.9061e+26	6.5992e+26	6.0704e+26	6.4643e+26	6.5446e+26	5.8050e+26
(4.625, 4.875)	4.5187e+26	5.0589e+26	4.6495e+26	4.9474e+26	5.0105e+26	4.4441e+26
(4.875, 5.125)	3.5320e+26	3.9674e+26	3.6413e+26	3.8695e+26	3.9201e+26	3.4762e+26
(5.125, 5.375)	2.7699e+26	3.1122e+26	2.8559e+26	3.0346e+26	3.0751e+26	2.7272e+26
(5.375, 5.625)	2.0710e+26	2.3283e+26	2.1360e+26	2.2691e+26	2.2995e+26	2.0393e+26
(5.625, 5.875)	1.6337e+26	1.8361e+26	1.6845e+26	1.7896e+26	1.8151e+26	1.6103e+26
(5.875, 6.125)	1.2040e+26	1.3610e+26	1.2457e+26	1.3204e+26	1.3397e+26	1.1880e+26
(6.125, 6.375)	8.6945e+25	9.8772e+25	9.0197e+25	9.5417e+25	9.6961e+25	8.5996e+25
(6.375, 6.625)	6.6261e+25	7.5168e+25	6.8684e+25	7.2701e+25	7.3853e+25	6.5501e+25
(6.625, 6.875)	4.9347e+25	5.5975e+25	5.1143e+25	5.4136e+25	5.5022e+25	4.8810e+25
(6.875, 7.125)	3.4615e+25	3.9345e+25	3.5919e+25	3.7991e+25	3.8612e+25	3.4247e+25
(7.125, 7.375)	2.2111e+25	2.5113e+25	2.2929e+25	2.4258e+25	2.4677e+25	2.1897e+25
(7.375, 7.625)	1.4136e+25	1.6094e+25	1.4680e+25	1.5517e+25	1.5785e+25	1.4003e+25
(7.625, 7.875)	8.6923e+24	9.9942e+24	9.0788e+24	9.5595e+24	9.7310e+24	8.6272e+24
(7.875, 8.125)	5.0610e+24	5.7698e+24	5.2593e+24	5.5568e+24	5.6509e+24	5.0122e+24
(8.125, 8.375)	2.9719e+24	3.3571e+24	3.0714e+24	3.2572e+24	3.3092e+24	2.9367e+24
(8.375, 8.625)	1.7610e+24	1.9699e+24	1.8094e+24	1.9264e+24	1.9554e+24	1.7363e+24
(8.625, 8.875)	1.0534e+24	1.1664e+24	1.0758e+24	1.1501e+24	1.1664e+24	1.0364e+24
(8.875, 9.125)	6.3641e+23	6.9722e+23	6.4587e+23	6.9337e+23	7.0266e+23	6.2480e+23
(9.125, 9.375)	3.8833e+23	4.2087e+23	3.9159e+23	4.2220e+23	4.2757e+23	3.8049e+23
(9.375, 9.625)	2.3934e+23	2.5659e+23	2.3981e+23	2.5966e+23	2.6281e+23	2.3406e+23

Table B.2 Predicted reactor antineutrino energy spectrum from each nuclear reactor integrated over the data acquisition time of EH2 (2011/12/24-2013/11/27). Applicable to EH2-AD1. The energy bins are presented as lower and upper bin edges.

Energy [MeV]	Reactor 1	Reactor 2	Reactor 3	Reactor 4	Reactor 5	Reactor 6
(1.375, 1.625)	6.1978e+27	6.8296e+27	6.3071e+27	6.7450e+27	6.8158e+27	6.0761e+27
(1.625, 1.875)	5.5195e+27	6.0860e+27	5.6125e+27	5.9983e+27	6.0627e+27	5.4061e+27
(1.875, 2.125)	4.6858e+27	5.1636e+27	4.7632e+27	5.0919e+27	5.1455e+27	4.5882e+27
(2.125, 2.375)	3.9785e+27	4.3813e+27	4.0429e+27	4.3230e+27	4.3675e+27	3.8945e+27
(2.375, 2.625)	3.2247e+27	3.5561e+27	3.2797e+27	3.5051e+27	3.5405e+27	3.1563e+27
(2.625, 2.875)	2.7189e+27	2.9933e+27	2.7636e+27	2.9560e+27	2.9845e+27	2.6605e+27
(2.875, 3.125)	2.2696e+27	2.5011e+27	2.3089e+27	2.4690e+27	2.4936e+27	2.2227e+27
(3.125, 3.375)	1.8775e+27	2.0779e+27	1.9150e+27	2.0445e+27	2.0654e+27	1.8404e+27
(3.375, 3.625)	1.5441e+27	1.7085e+27	1.5749e+27	1.6817e+27	1.6991e+27	1.5140e+27
(3.625, 3.875)	1.2380e+27	1.3703e+27	1.2629e+27	1.3484e+27	1.3626e+27	1.2142e+27
(3.875, 4.125)	9.8453e+26	1.0927e+27	1.0059e+27	1.0729e+27	1.0841e+27	9.6570e+26
(4.125, 4.375)	7.7854e+26	8.6300e+26	7.9488e+26	8.4820e+26	8.5707e+26	7.6362e+26
(4.375, 4.625)	5.9595e+26	6.6285e+26	6.0962e+26	6.4963e+26	6.5674e+26	5.8503e+26
(4.625, 4.875)	4.5597e+26	5.0812e+26	4.6691e+26	4.9718e+26	5.0280e+26	4.4788e+26
(4.875, 5.125)	3.5642e+26	3.9847e+26	3.6566e+26	3.8886e+26	3.9338e+26	3.5033e+26
(5.125, 5.375)	2.7952e+26	3.1258e+26	2.8679e+26	3.0495e+26	3.0859e+26	2.7485e+26
(5.375, 5.625)	2.0899e+26	2.3384e+26	2.1449e+26	2.2803e+26	2.3076e+26	2.0552e+26
(5.625, 5.875)	1.6487e+26	1.8441e+26	1.6915e+26	1.7984e+26	1.8215e+26	1.6228e+26
(5.875, 6.125)	1.2151e+26	1.3668e+26	1.2508e+26	1.3268e+26	1.3444e+26	1.1973e+26
(6.125, 6.375)	8.7754e+25	9.9187e+25	9.0562e+25	9.5877e+25	9.7303e+25	8.6666e+25
(6.375, 6.625)	6.6876e+25	7.5485e+25	6.8964e+25	7.3052e+25	7.4113e+25	6.6012e+25
(6.625, 6.875)	4.9805e+25	5.6211e+25	5.1351e+25	5.4397e+25	5.5216e+25	4.9191e+25
(6.875, 7.125)	3.4937e+25	3.9510e+25	3.6065e+25	3.8173e+25	3.8749e+25	3.4514e+25
(7.125, 7.375)	2.2317e+25	2.5219e+25	2.3022e+25	2.4375e+25	2.4764e+25	2.2068e+25
(7.375, 7.625)	1.4268e+25	1.6161e+25	1.4739e+25	1.5591e+25	1.5841e+25	1.4113e+25
(7.625, 7.875)	8.7746e+24	1.0035e+25	9.1143e+24	9.6046e+24	9.7658e+24	8.6944e+24
(7.875, 8.125)	5.1083e+24	5.7937e+24	5.2803e+24	5.5834e+24	5.6709e+24	5.0513e+24
(8.125, 8.375)	2.9993e+24	3.3715e+24	3.0841e+24	3.2731e+24	3.3208e+24	2.9596e+24
(8.375, 8.625)	1.7770e+24	1.9786e+24	1.8171e+24	1.9359e+24	1.9622e+24	1.7499e+24
(8.625, 8.875)	1.0629e+24	1.1717e+24	1.0805e+24	1.1559e+24	1.1704e+24	1.0445e+24
(8.875, 9.125)	6.4201e+23	7.0051e+23	6.4876e+23	6.9692e+23	7.0505e+23	6.2969e+23
(9.125, 9.375)	3.9169e+23	4.2292e+23	3.9340e+23	4.2440e+23	4.2901e+23	3.8347e+23
(9.375, 9.625)	2.4137e+23	2.5788e+23	2.4095e+23	2.6103e+23	2.6369e+23	2.3590e+23

Table B.3 Predicted reactor antineutrino energy spectrum from each nuclear reactor integrated over the data acquisition time of EH2 during the 8-AD period (2012/10/19-2013/11/27). Applicable to EH2-AD2. The energy bins are presented as lower and upper bin edges.

Energy [MeV]	Reactor 1	Reactor 2	Reactor 3	Reactor 4	Reactor 5	Reactor 6
(1.375, 1.625)	4.4013e+27	4.3154e+27	4.1376e+27	4.5388e+27	4.3992e+27	4.3732e+27
(1.625, 1.875)	3.9203e+27	3.8443e+27	3.6830e+27	4.0356e+27	3.9134e+27	3.8899e+27
(1.875, 2.125)	3.3281e+27	3.2624e+27	3.1256e+27	3.4264e+27	3.3211e+27	3.3015e+27
(2.125, 2.375)	2.8257e+27	2.7689e+27	2.6529e+27	2.9095e+27	2.8188e+27	2.8024e+27
(2.375, 2.625)	2.2899e+27	2.2463e+27	2.1519e+27	2.3581e+27	2.2856e+27	2.2716e+27
(2.625, 2.875)	1.9309e+27	1.8921e+27	1.8133e+27	1.9897e+27	1.9262e+27	1.9150e+27
(2.875, 3.125)	1.6116e+27	1.5804e+27	1.5147e+27	1.6614e+27	1.6096e+27	1.5999e+27
(3.125, 3.375)	1.3326e+27	1.3109e+27	1.2560e+27	1.3741e+27	1.3341e+27	1.3250e+27
(3.375, 3.625)	1.0960e+27	1.0779e+27	1.0330e+27	1.1304e+27	1.0974e+27	1.0900e+27
(3.625, 3.875)	8.7872e+26	8.6443e+26	8.2830e+26	9.0616e+26	8.8011e+26	8.7408e+26
(3.875, 4.125)	6.9859e+26	6.8863e+26	6.5969e+26	7.2048e+26	7.0054e+26	6.9533e+26
(4.125, 4.375)	5.5250e+26	5.4413e+26	5.2129e+26	5.6979e+26	5.5374e+26	5.4978e+26
(4.375, 4.625)	4.2280e+26	4.1740e+26	3.9974e+26	4.3597e+26	4.2454e+26	4.2121e+26
(4.625, 4.875)	3.2344e+26	3.1974e+26	3.0614e+26	3.3347e+26	3.2512e+26	3.2246e+26
(4.875, 5.125)	2.5275e+26	2.5044e+26	2.3972e+26	2.6057e+26	2.5450e+26	2.5225e+26
(5.125, 5.375)	1.9821e+26	1.9643e+26	1.8802e+26	2.0432e+26	1.9965e+26	1.9788e+26
(5.375, 5.625)	1.4819e+26	1.4692e+26	1.4062e+26	1.5276e+26	1.4931e+26	1.4797e+26
(5.625, 5.875)	1.1693e+26	1.1587e+26	1.1090e+26	1.2049e+26	1.1784e+26	1.1680e+26
(5.875, 6.125)	8.6128e+25	8.5704e+25	8.1983e+25	8.8743e+25	8.7056e+25	8.6189e+25
(6.125, 6.375)	6.2182e+25	6.2079e+25	5.9349e+25	6.4033e+25	6.3052e+25	6.2371e+25
(6.375, 6.625)	4.7393e+25	4.7269e+25	4.5197e+25	4.8809e+25	4.8015e+25	4.7509e+25
(6.625, 6.875)	3.5298e+25	3.5200e+25	3.3655e+25	3.6345e+25	3.5770e+25	3.5396e+25
(6.875, 7.125)	2.4755e+25	2.4724e+25	2.3634e+25	2.5490e+25	2.5111e+25	2.4837e+25
(7.125, 7.375)	1.5817e+25	1.5784e+25	1.5087e+25	1.6280e+25	1.6045e+25	1.5875e+25
(7.375, 7.625)	1.0110e+25	1.0107e+25	9.6580e+24	1.0406e+25	1.0267e+25	1.0153e+25
(7.625, 7.875)	6.2112e+24	6.2534e+24	5.9700e+24	6.3920e+24	6.3397e+24	6.2570e+24
(7.875, 8.125)	3.6187e+24	3.6216e+24	3.4596e+24	3.7251e+24	3.6766e+24	3.6346e+24
(8.125, 8.375)	2.1264e+24	2.1145e+24	2.0212e+24	2.1895e+24	2.1499e+24	2.1291e+24
(8.375, 8.625)	1.2610e+24	1.2453e+24	1.1912e+24	1.2987e+24	1.2684e+24	1.2585e+24
(8.625, 8.875)	7.5492e+23	7.4021e+23	7.0861e+23	7.7767e+23	7.5535e+23	7.5102e+23
(8.875, 9.125)	4.5644e+23	4.4424e+23	4.2561e+23	4.7027e+23	4.5426e+23	4.5260e+23
(9.125, 9.375)	2.7876e+23	2.6926e+23	2.5818e+23	2.8724e+23	2.7594e+23	2.7552e+23
(9.375, 9.625)	1.7195e+23	1.6485e+23	1.5819e+23	1.7720e+23	1.6932e+23	1.6942e+23

Table B.4 Predicted reactor antineutrino energy spectrum from each nuclear reactor integrated over the data acquisition time of EH3 (2011/12/24-2013/11/27). Applicable to EH3-AD1, EH3-AD2, and EH3-AD3. The energy bins are presented as lower and upper bin edges.

Energy [MeV]	Reactor 1	Reactor 2	Reactor 3	Reactor 4	Reactor 5	Reactor 6
(1.375, 1.625)	6.1167e+27	6.7569e+27	6.2487e+27	6.6749e+27	6.7455e+27	6.0002e+27
(1.625, 1.875)	5.4473e+27	6.0213e+27	5.5605e+27	5.9359e+27	6.0001e+27	5.3385e+27
(1.875, 2.125)	4.6244e+27	5.1086e+27	4.7191e+27	5.0390e+27	5.0924e+27	4.5309e+27
(2.125, 2.375)	3.9263e+27	4.3348e+27	4.0054e+27	4.2780e+27	4.3225e+27	3.8458e+27
(2.375, 2.625)	3.1825e+27	3.5183e+27	3.2493e+27	3.4687e+27	3.5040e+27	3.1169e+27
(2.625, 2.875)	2.6833e+27	2.9615e+27	2.7380e+27	2.9253e+27	2.9538e+27	2.6272e+27
(2.875, 3.125)	2.2398e+27	2.4745e+27	2.2875e+27	2.4433e+27	2.4679e+27	2.1950e+27
(3.125, 3.375)	1.8530e+27	2.0557e+27	1.8972e+27	2.0233e+27	2.0441e+27	1.8174e+27
(3.375, 3.625)	1.5240e+27	1.6902e+27	1.5603e+27	1.6643e+27	1.6815e+27	1.4951e+27
(3.625, 3.875)	1.2218e+27	1.3557e+27	1.2512e+27	1.3343e+27	1.3485e+27	1.1990e+27
(3.875, 4.125)	9.7170e+26	1.0810e+27	9.9660e+26	1.0617e+27	1.0728e+27	9.5362e+26
(4.125, 4.375)	7.6838e+26	8.5378e+26	7.8750e+26	8.3939e+26	8.4820e+26	7.5407e+26
(4.375, 4.625)	5.8820e+26	6.5574e+26	6.0395e+26	6.4289e+26	6.4992e+26	5.7771e+26
(4.625, 4.875)	4.5005e+26	5.0266e+26	4.6257e+26	4.9202e+26	4.9757e+26	4.4227e+26
(4.875, 5.125)	3.5180e+26	3.9419e+26	3.6225e+26	3.8482e+26	3.8928e+26	3.4594e+26
(5.125, 5.375)	2.7590e+26	3.0922e+26	2.8411e+26	3.0178e+26	3.0537e+26	2.7140e+26
(5.375, 5.625)	2.0628e+26	2.3133e+26	2.1249e+26	2.2566e+26	2.2835e+26	2.0294e+26
(5.625, 5.875)	1.6273e+26	1.8242e+26	1.6757e+26	1.7797e+26	1.8025e+26	1.6025e+26
(5.875, 6.125)	1.1994e+26	1.3520e+26	1.2391e+26	1.3131e+26	1.3303e+26	1.1823e+26
(6.125, 6.375)	8.6627e+25	9.8112e+25	8.9712e+25	9.4884e+25	9.6282e+25	8.5578e+25
(6.375, 6.625)	6.6016e+25	7.4667e+25	6.8317e+25	7.2295e+25	7.3336e+25	6.5183e+25
(6.625, 6.875)	4.9165e+25	5.5602e+25	5.0870e+25	5.3834e+25	5.4637e+25	4.8574e+25
(6.875, 7.125)	3.4489e+25	3.9082e+25	3.5726e+25	3.7778e+25	3.8342e+25	3.4080e+25
(7.125, 7.375)	2.2031e+25	2.4946e+25	2.2806e+25	2.4123e+25	2.4504e+25	2.1791e+25
(7.375, 7.625)	1.4085e+25	1.5985e+25	1.4600e+25	1.5430e+25	1.5674e+25	1.3935e+25
(7.625, 7.875)	8.6630e+24	9.9248e+24	9.0282e+24	9.5053e+24	9.6625e+24	8.5850e+24
(7.875, 8.125)	5.0429e+24	5.7308e+24	5.2307e+24	5.5256e+24	5.6113e+24	4.9878e+24
(8.125, 8.375)	2.9606e+24	3.3351e+24	3.0552e+24	3.2391e+24	3.2861e+24	2.9225e+24
(8.375, 8.625)	1.7539e+24	1.9574e+24	1.8002e+24	1.9159e+24	1.9418e+24	1.7280e+24
(8.625, 8.875)	1.0489e+24	1.1593e+24	1.0705e+24	1.1439e+24	1.1584e+24	1.0315e+24
(8.875, 9.125)	6.3354e+23	6.9312e+23	6.4279e+23	6.8967e+23	6.9784e+23	6.2185e+23
(9.125, 9.375)	3.8648e+23	4.1849e+23	3.8980e+23	4.1997e+23	4.2465e+23	3.7870e+23
(9.375, 9.625)	2.3814e+23	2.5521e+23	2.3875e+23	2.5831e+23	2.6103e+23	2.3297e+23

Table B.5 Predicted reactor antineutrino energy spectrum from each nuclear reactor integrated over the data acquisition time of EH3 during the 8-AD period (2012/10/19-2013/11/27). Applicable to EH3-AD4. The energy bins are presented as lower and upper bin edges.

Energy [MeV]	Reactor 1	Reactor 2	Reactor 3	Reactor 4	Reactor 5	Reactor 6
(1.375, 1.625)	4.3327e+27	4.2414e+27	4.0739e+27	4.4662e+27	4.3269e+27	4.3115e+27
(1.625, 1.875)	3.8592e+27	3.7783e+27	3.6263e+27	3.9711e+27	3.8490e+27	3.8350e+27
(1.875, 2.125)	3.2762e+27	3.2065e+27	3.0775e+27	3.3716e+27	3.2665e+27	3.2549e+27
(2.125, 2.375)	2.7817e+27	2.7214e+27	2.6121e+27	2.8630e+27	2.7724e+27	2.7628e+27
(2.375, 2.625)	2.2542e+27	2.2078e+27	2.1188e+27	2.3204e+27	2.2480e+27	2.2395e+27
(2.625, 2.875)	1.9007e+27	1.8596e+27	1.7854e+27	1.9579e+27	1.8946e+27	1.8879e+27
(2.875, 3.125)	1.5864e+27	1.5533e+27	1.4914e+27	1.6348e+27	1.5831e+27	1.5774e+27
(3.125, 3.375)	1.3119e+27	1.2883e+27	1.2367e+27	1.3521e+27	1.3122e+27	1.3063e+27
(3.375, 3.625)	1.0790e+27	1.0594e+27	1.0171e+27	1.1123e+27	1.0794e+27	1.0746e+27
(3.625, 3.875)	8.6506e+26	8.4954e+26	8.1553e+26	8.9167e+26	8.6562e+26	8.6173e+26
(3.875, 4.125)	6.8775e+26	6.7674e+26	6.4950e+26	7.0896e+26	6.8900e+26	6.8551e+26
(4.125, 4.375)	5.4392e+26	5.3474e+26	5.1325e+26	5.6068e+26	5.4463e+26	5.4201e+26
(4.375, 4.625)	4.1625e+26	4.1018e+26	3.9356e+26	4.2900e+26	4.1754e+26	4.1525e+26
(4.625, 4.875)	3.1843e+26	3.1419e+26	3.0141e+26	3.2814e+26	3.1976e+26	3.1789e+26
(4.875, 5.125)	2.4885e+26	2.4609e+26	2.3601e+26	2.5640e+26	2.5030e+26	2.4868e+26
(5.125, 5.375)	1.9516e+26	1.9302e+26	1.8510e+26	2.0106e+26	1.9635e+26	1.9508e+26
(5.375, 5.625)	1.4591e+26	1.4437e+26	1.3844e+26	1.5032e+26	1.4684e+26	1.4587e+26
(5.625, 5.875)	1.1512e+26	1.1386e+26	1.0918e+26	1.1856e+26	1.1589e+26	1.1515e+26
(5.875, 6.125)	8.4804e+25	8.4206e+25	8.0708e+25	8.7325e+25	8.5616e+25	8.4967e+25
(6.125, 6.375)	6.1230e+25	6.0989e+25	5.8424e+25	6.3009e+25	6.2007e+25	6.1486e+25
(6.375, 6.625)	4.6666e+25	4.6440e+25	4.4492e+25	4.8029e+25	4.7220e+25	4.6835e+25
(6.625, 6.875)	3.4757e+25	3.4583e+25	3.3130e+25	3.5764e+25	3.5177e+25	3.4893e+25
(6.875, 7.125)	2.4377e+25	2.4289e+25	2.3265e+25	2.5083e+25	2.4694e+25	2.4485e+25
(7.125, 7.375)	1.5574e+25	1.5507e+25	1.4852e+25	1.6019e+25	1.5779e+25	1.5649e+25
(7.375, 7.625)	9.9551e+24	9.9288e+24	9.5072e+24	1.0239e+25	1.0097e+25	1.0009e+25
(7.625, 7.875)	6.1169e+24	6.1424e+24	5.8763e+24	6.2898e+24	6.2343e+24	6.1679e+24
(7.875, 8.125)	3.5634e+24	3.5578e+24	3.4056e+24	3.6656e+24	3.6156e+24	3.5830e+24
(8.125, 8.375)	2.0937e+24	2.0775e+24	1.9898e+24	2.1545e+24	2.1143e+24	2.0990e+24
(8.375, 8.625)	1.2414e+24	1.2237e+24	1.1728e+24	1.2779e+24	1.2474e+24	1.2407e+24
(8.625, 8.875)	7.4316e+23	7.2751e+23	6.9771e+23	7.6524e+23	7.4294e+23	7.4042e+23
(8.875, 9.125)	4.4928e+23	4.3669e+23	4.1910e+23	4.6276e+23	4.4682e+23	4.4623e+23
(9.125, 9.375)	2.7435e+23	2.6473e+23	2.5425e+23	2.8264e+23	2.7143e+23	2.7165e+23
(9.375, 9.625)	1.6922e+23	1.6210e+23	1.5579e+23	1.7436e+23	1.6656e+23	1.6705e+23

B.2 Efficiency correction factors

This appendix provides the efficiency correction factors described in Section 7.2.1. Factors were calculated for each fit iteration. The factors supplied in Tables B.6-B.11 were calculated after the third fit (used for the fourth fit).

The three sets of factors listed in Tables B.6, B.7, and B.8 were generated assuming the normal neutrino mass hierarchy ($\Delta m^2_{32} > 0$). The three sets of factors listed in Tables B.9, B.10, and B.11 were generated assuming the inverted neutrino mass hierarchy ($\Delta m^2_{32} < 0$).

Table B.6 Efficiency correction factors for the LS volume of each detector-reactor pair assuming the normal mass hierarchy.

Detector	Reactor 1	Reactor 2	Reactor 3	Reactor 4	Reactor 5	Reactor 6
EH1-AD1	1.00052	1.00077	1.00210	1.00181	1.00028	1.00138
EH1-AD2	1.00053	1.00092	1.00208	1.00216	1.00108	1.00149
EH2-AD1	1.00093	1.00061	1.00109	1.00122	1.00162	1.00127
EH2-AD2	1.00086	1.00074	1.00103	1.00101	1.00138	1.00098
EH3-AD1	0.99731	0.99727	0.99964	0.99939	0.99934	0.99989
EH3-AD2	0.99711	0.99794	0.99968	0.99978	0.99935	1.00010
EH3-AD3	0.99753	0.99783	1.00016	0.99982	0.99978	1.00014
EH3-AD4	0.99684	0.99768	0.99970	0.99907	0.99933	0.99968

Table B.7 Efficiency correction factors for the GdLS volume of each detector-reactor pair assuming the normal mass hierarchy.

Detector	Reactor 1	Reactor 2	Reactor 3	Reactor 4	Reactor 5	Reactor 6
EH1-AD1	1.00084	1.00032	1.00144	1.00190	1.00038	1.00180
EH1-AD2	1.00070	1.00028	1.00066	1.00039	1.00033	1.00145
EH2-AD1	0.99941	0.99994	1.00013	1.00095	1.00177	1.00103
EH2-AD2	1.00067	0.99998	1.00121	1.00087	1.00117	1.00115
EH3-AD1	0.99837	0.99693	0.99982	0.99912	0.99775	0.99797
EH3-AD2	0.99698	0.99756	1.00047	1.00055	1.00047	0.99984
EH3-AD3	0.99815	0.99842	0.99921	0.99937	0.99972	0.99972
EH3-AD4	0.99675	0.99805	0.99973	1.00120	0.99812	0.99887

Table B.8 Efficiency correction factors for the acrylic volume of each detector-reactor pair assuming the normal mass hierarchy.

Detector	Reactor 1	Reactor 2	Reactor 3	Reactor 4	Reactor 5	Reactor 6
EH1-AD1	1.00199	1.00192	1.00443	1.00672	1.00573	1.00264
EH1-AD2	1.00152	1.00122	1.00296	1.00472	1.00830	1.00643
EH2-AD1	1.00130	1.00111	1.00211	1.00037	0.99951	1.00017
EH2-AD2	1.00389	1.00222	1.00381	1.00103	1.00116	1.00019
EH3-AD1	0.99646	1.00105	1.00351	0.99779	1.00175	1.00236
EH3-AD2	0.99930	0.99597	1.00211	1.00201	1.00319	1.00052
EH3-AD3	0.99641	0.99435	1.00397	1.00269	1.00571	1.00312
EH3-AD4	0.99588	0.99492	0.99899	1.00318	1.00055	1.00456

Table B.9 Efficiency correction factors for the LS volume of each detector-reactor pair assuming the inverted mass hierarchy.

Detector	Reactor 1	Reactor 2	Reactor 3	Reactor 4	Reactor 5	Reactor 6
EH1-AD1	1.00077	1.00085	1.00276	1.00245	1.00118	1.00174
EH1-AD2	1.00074	1.00075	1.00247	1.00255	1.00122	1.00181
EH2-AD1	1.00116	1.00131	1.00120	1.00122	1.00146	1.00139
EH2-AD2	1.00129	1.00124	1.00115	1.00128	1.00173	1.00142
EH3-AD1	0.99711	0.99738	0.99989	1.00006	0.99971	1.00013
EH3-AD2	0.99712	0.99721	0.99999	0.99983	0.99963	1.00011
EH3-AD3	0.99708	0.99722	0.99984	0.99982	0.99977	0.99989
EH3-AD4	0.99710	0.99717	1.00000	0.99989	0.99969	0.99998

Table B.10 Efficiency correction factors for the GdLS volume of each detector-reactor pair assuming the inverted mass hierarchy.

Detector	Reactor 1	Reactor 2	Reactor 3	Reactor 4	Reactor 5	Reactor 6
EH1-AD1	1.00063	1.00051	1.00191	1.00172	1.00090	1.00093
EH1-AD2	1.00054	1.00050	1.00182	1.00169	1.00063	1.00094
EH2-AD1	1.00069	1.00074	1.00068	1.00080	1.00098	1.00098
EH2-AD2	1.00074	1.00064	1.00091	1.00101	1.00109	1.00090
EH3-AD1	0.99761	0.99785	0.99991	0.99969	0.99946	0.99973
EH3-AD2	0.99800	0.99797	0.99973	0.99949	0.99927	0.99985
EH3-AD3	0.99803	0.99811	0.99993	0.99936	0.99945	0.99989
EH3-AD4	0.99780	0.99790	0.99986	0.99959	0.99931	0.99959

Table B.11 Efficiency correction factors for the acrylic volume of each detector-reactor pair assuming the inverted mass hierarchy.

Detector	Reactor 1	Reactor 2	Reactor 3	Reactor 4	Reactor 5	Reactor 6
EH1-AD1	1.00037	1.00084	1.00507	1.00310	1.00672	1.00442
EH1-AD2	1.00126	1.00090	1.00699	1.00881	1.00606	1.00629
EH2-AD1	1.00805	1.00673	1.00201	1.00164	1.00278	1.00081
EH2-AD2	1.00736	1.00750	1.00272	1.00259	1.00443	1.00227
EH3-AD1	1.00110	0.99921	1.00409	1.00435	1.00418	1.00150
EH3-AD2	0.99828	1.00015	1.00165	1.00583	1.00762	1.00569
EH3-AD3	0.99665	1.00050	1.00570	1.00420	1.00303	1.00524
EH3-AD4	1.00223	0.99546	1.00347	1.00348	1.00335	1.00494

B.3 Efficiency-weighted target protons

Table B.12 lists the efficiency-weighted number of target protons for the LS, GdLS, and acrylic volumes of each AD. The calculation of these numbers followed Eq. (7-1) such that the sum of the values of each volume equals N_{ε}: $N_{\varepsilon,\mathrm{LS}} + N_{\varepsilon,\mathrm{GdLS}} + N_{\varepsilon,\mathrm{acrylic}} = N_{\varepsilon}$.

Table B.12 Efficiency-weighted number of target protons of each volume of each AD.

Detector	$N_{\varepsilon,\mathrm{LS}}$	$N_{\varepsilon,\mathrm{GdLS}}$	$N_{\varepsilon,\mathrm{acrylic}}$
EH1-AD1	0.4574e+30	0.1151e+30	0.0057e+30
EH1-AD2	0.4546e+30	0.1148e+30	0.0058e+30
EH2-AD1	0.4799e+30	0.1203e+30	0.0060e+30
EH2-AD2	0.4768e+30	0.1207e+30	0.0061e+30
EH3-AD1	0.5643e+30	0.1419e+30	0.0072e+30
EH3-AD2	0.5601e+30	0.1423e+30	0.0074e+30
EH3-AD3	0.5665e+30	0.1416e+30	0.0074e+30
EH3-AD4	0.5622e+30	0.1420e+30	0.0073e+30